



HAL
open science

Water Vapor Transport Across an Arid Sand Surface-Non-Linear Thermal Coupling, Wind-Driven Pore Advection, Subsurface Waves, and Exchange With the Atmospheric Boundary Layer

M. Y. Louge, Alexandre Valance, J. Xu, Ahmed Ould El Moctar, Patrick Chasle

► **To cite this version:**

M. Y. Louge, Alexandre Valance, J. Xu, Ahmed Ould El Moctar, Patrick Chasle. Water Vapor Transport Across an Arid Sand Surface-Non-Linear Thermal Coupling, Wind-Driven Pore Advection, Subsurface Waves, and Exchange With the Atmospheric Boundary Layer. *Journal of Geophysical Research: Earth Surface*, 2022, 127 (4), pp.e2021JF006490. 10.1029/2021JF006490 . hal-03657541

HAL Id: hal-03657541

<https://hal.science/hal-03657541>

Submitted on 14 Oct 2022

HAL is a multi-disciplinary open access archive for the deposit and dissemination of scientific research documents, whether they are published or not. The documents may come from teaching and research institutions in France or abroad, or from public or private research centers.

L'archive ouverte pluridisciplinaire **HAL**, est destinée au dépôt et à la diffusion de documents scientifiques de niveau recherche, publiés ou non, émanant des établissements d'enseignement et de recherche français ou étrangers, des laboratoires publics ou privés.

1 **Water vapor transport across an arid sand surface -**
2 **non-linear thermal coupling, wind-driven pore**
3 **advection, subsurface waves, and exchange with the**
4 **atmospheric boundary layer**

5 **M. Y. Louge¹, A. Valance², J. Xu¹, A. Ould el-Moctar³, P. Chasle²**

6 ¹Sibley School of Mechanical and Aerospace Engineering, Cornell University, Ithaca, NY 14853, USA.

7 ²Institut de Physique de Rennes, Université de Rennes 1, France.

8 ³Ecole Polytechnique de l'Université de Nantes, France.

9 **Key Points:**

- 10 • We detect tiny spatio-temporal moisture variations below a hyper-arid mobile dune
11 with a new capacitance instrument.
- 12 • We predict moisture profiles, internal waves and wind-driven pore advection. Grain
13 evaporation is a kinetic-limited, activated process.
- 14 • The moisture surface flux is weaker than expected, and not always proportional
15 to the mass fraction difference between surface and ambient.

Abstract

Although vapor exchanged across hyper-arid surfaces without free liquid affects the water budget of sand seas, its mechanism is poorly documented for want of accurate instruments with fine spatial resolution. To rectify this, we report bulk density profiles and spatio-temporal variations of vapor mass fraction just below the surface of a mobile dune, acquired with a multi-sensor capacitance probe sensitive to tiny water films adsorbed on sand grains. We also record wind speed and direction, ambient temperature and relative humidity, net radiation flux, and subsurface temperature profiles over two days. The data validate a non-linear model of vapor mass fraction. Unlike heat, which conducts through grains, vapor percolates across the interstitial pore space by advection and diffusion. On time scales longer than evaporation, adsorbed films equilibrate with their surroundings and hinder molecular diffusion. Their non-linear coupling with subsurface temperature generates inflections in vapor profiles without counterpart in simpler diffusive systems. Pore advection arises as wind induces subtle pressure variations over the topography. During periods of aeolian transport, flowing sand dehydrates the surface intermittently, triggering evanescent vapor waves of amplitude decaying exponentially downward on a characteristic length implying an adsorption rate governed by a kinetic-limited activated process. Finally, the probe yields diffusive and advective exchanges with the atmospheric boundary layer. During the day, their combined flux is smaller than expected, yet nearly proportional to the difference between vapor mass fraction at the surface and aloft. Under stabler stratification at night, or during aeolian sand transport, this relation no longer holds.

Plain Language Summary

Deserts inhale and exhale water vapor through their surface. Although this process affects the water balance over vast sand seas, it is poorly understood for want of sensitive instruments. We discover how it operates using a new probe that detects tiny amounts of moisture on sand grains. Our analysis reveals that vapor infiltration is considerably slower in dry sand, and that wind flowing over a dune creates weak internal air currents contributing to the transport of moisture. Their strength depends on dune location, wind speed and direction. When wind is strong enough to let dry sand meander over a dune, the resulting rapid variation in surface moisture sends evanescent waves of humidity downward. An analysis of these waves implies that water evaporation from individual sand grains behaves like a slow chemical reaction. The exchange of moisture with the atmosphere is not always driven by the difference between humidity at the dune surface and in the ambient, as current models assume, and it is weaker than they predict. In future, the new probe can be used as “ground truth” to calibrate satellite observations over deserts, explore extra-terrestrial environments holding scant water, and detect moisture contamination in pharmaceutical products.

1 Introduction

Sands of hyper-arid deserts subject to infrequent precipitation experience a diurnal exchange of water vapor between the ambient and a relatively shallow layer just below the surface (Kobayashi et al., 1986). Although free-liquid water is largely absent, this exchange can be intense in fog deserts where morning relative humidity is high (Lancaster et al., 1984; Cereceda et al., 2008). In turn, moisture profiles determine the viability of microorganisms sheltering from high temperatures (Cáceres et al., 2007). If sands imbibe morning dew fast enough (Gambaryan-Roisman, 2014; Johnson & Dettre, 1964), grains can bind with ephemeral capillary bridges forming at their contacts (Mitarai & Nori, 2006), thereby briefly affecting surface cohesion and the rate of aeolian transport (Ravi et al., 2006; Rotnicka, 2013). Understanding how and when hyper-arid sand surfaces exchange water vapor with the atmosphere is therefore crucial to subjects as diverse as zo-

66 ology (Robinson & Barrows, 2013), microbiology (Heulin et al., 2012; Louge et al., 2013),
67 botany (Wilcox et al., 2004), and desertification management (Fang et al., 2007; T. Wang
68 et al., 2011).

69 Unfortunately, precise measurements of solid-bound water below the surface of hyper-
70 arid sands are rare. They are usually achieved by weighing and drying samples collected
71 over a relatively large volume (Dincer et al., 1974; Kobayashi et al., 1991; J. Wang & Mit-
72 suta, 1992; Ritsema & Dekker, 1994; Feigenwinter et al., 2020). Using time-domain re-
73 flectometry (TDR), Shao et al. (2021) recently reported measurements of water volume
74 fraction in the hyper-arid Taklamakan desert. They also summarized the approach that
75 is typically adopted to analyze the water retention of arid soils. In general, detailed time-
76 histories of moisture depth profiles are not as well established as the corresponding tem-
77 perature records (de Félice, 1968), particular near the surface where gradients of water
78 mass fraction are largest.

79 To address this, Louge, Valance, Babah, et al. (2010) exploited a capacitance tech-
80 nique that Louge et al. (1998) had designed for alpine snowpacks to record solid volume
81 fraction and solid-bound water mass fraction through the first 30 cm of dune sands, where
82 moisture is most likely to be affected by diurnal changes in ambient conditions. How-
83 ever, because those authors did not repeat these measurements throughout the day, it
84 remained unclear how moisture profiles evolved during a complete diurnal period. More
85 significantly, their governing equations for mass transfer ignored water adsorption on the
86 surface of sand grains, therefore overestimating the diffusion rate of moisture into dry
87 sands, and they did not consider the possibility that advection could take place deeper
88 than what they had calculated within sand ripples.

89 In this context, we designed a new probe to record low water mass fractions vs depth
90 and time on a fine spatial resolution. Our simultaneous development of capacitance in-
91 struments for moisture and bulk density measurements in pharmaceutical powders con-
92 ferred an unprecedented precision to this technique (Louge et al., 2021). The probe is
93 intended for “hygroscopic” conditions, where water either exists as a vapor or is adsorbed
94 on sand grains (Shahraeeni & Or, 2010). We inserted it in a mobile barchan dune of the
95 Qatar desert. Its measurements at 2.7 min intervals revealed hitherto undocumented phe-
96 nomena that similar instruments lacking fine spatial resolution could not discern.

97 First, the data set implies the existence of a slow wind-driven “seepage” advection
98 flow in the pore space below the surface that augments water diffusion. Inspired by the
99 theory of P. S. Jackson and Hunt (1975), we suggest that the advection derives from pres-
100 sure variations on the dune topography. Beside recording stratigraphic layering of the
101 subsurface, the probe also reveals evanescent waves of moisture coinciding with the on-
102 set of aeolian transport. The exponential decay of their amplitude with depth implies
103 that evaporation acts as a slow activated reaction. Next, we explain why spatial vari-
104 ations of vapor mass fraction feature multiple moisture profiles inflexions without a coun-
105 terpart in simpler advection-diffusion systems such as heat transfer through sands (Louge
106 et al., 2013). Finally, the data set provides a unique “ground truth” for the moisture flux
107 through a hyper-arid surface into the atmospheric boundary layer. As such, it has the
108 potential to complement models of deeper moisture exchange in deserts, such as those
109 of Kamai and Assouline (2018); Assouline and Kamai (2019); Shao et al. (2021) and, when
110 the near-surface holds no liquid water, to revisit the classical formulations of Philip and
111 De Vries (1957); Jury and Letey Jr (1979); Parlange (1980); Brutsaert (1982, 1986); Cahill
112 and Parlange (1998) for water transport in wetter soils.

113 We begin with a description of the new probe and its response to the moisture con-
114 tent of sands. We then present the data set from all deployed instruments. We derive
115 governing equations to interpret the resulting observations, and we use this framework
116 to identify the principal mechanisms of hygroscopic subsurface moisture transport and
117 dismiss those that are negligible. In future, the sensitivity of our technique, and the mod-

118 els that the new probe inspired, will make it possible to discern very low levels of mois-
 119 ture and understand its transport in the desert subsurface, or potentially in extra-terrestrial
 120 environments (Honniball et al., 2020; Davidsson & Hosseini, 2021).

121 2 Instruments

122 We designed two bespoke instruments for insertion through sand surfaces: a rec-
 123 tilinear lance with 15 temperature sensors (LM235 National Semiconductor temperature-
 124 sensitive Zener diodes), already exploited by Louge et al. (2013), and a capacitance probe
 125 with another 15 sensors recording moisture vs depth, shown in Fig. 1 and described in Ap-
 126 pendix A. We inserted these instruments perpendicularly to the sand free surface un-
 127 til their top skimmed it without impeding sand transport, through a relatively soft zone
 128 upwind of a barchan sand dune west of Mesaieed, Qatar at $25^{\circ}00'34.7''\text{N}$, $51^{\circ}20'24.9''\text{E}$.
 129 We mounted a Kipp & Zonen NR-Lite-2 radiometer nearby, and we buried the electron-
 130 ics, batteries and data acquisition system under a thin reflective emergency blanket ap-
 131 proximately 1.5 m away. The system took approximately 20 s to scan all temperature,
 132 moisture and radiation sensors every 2.7 min for nearly two days. In addition, we deployed
 133 a weather station above hard ground upstream of the dune at the location shown in Fig. 1D
 134 to record ambient humidity and temperature at 0.9 m and 2 m altitude, as well as wind
 135 speed at 0.9 m and 2.4 m, and wind direction at 2.4 m, every minute. Michel et al. (2018)
 136 later exploited this aeolian data to calibrate optical satellite imagery for dune motion.

137 Louge et al. (2013) provided additional information on this site, including avail-
 138 able long-term rain and wind records, location and speed of barchans in the region, mea-
 139 surements of relative humidity and temperature from a probe buried deeply in our dune
 140 over several months, modeling of deep water penetration and thermal energy, near-surface
 141 thermal exchanges, particle characterization (size distribution, grain composition), and
 142 biology. Arran (2018) also recorded detailed stratigraphy near the dune surface. Mean-
 143 while, Abdul-Majid, Graw, et al. (2016) carried out the first characterization of the mi-
 144 crobiota within mobile dunes in this field, including our own, which they dubbed “Na-
 145 dine”, while Abdul-Majid, Chatziefthimiou, et al. (2016) considered their herpetology.

146 On long time scales, the capacitance probe is mainly sensitive to the mass fraction
 147 Ω of water adsorbed on sand grains, as discussed in Appendix A. When the vapor mass
 148 fraction Y (a.k.a. specific humidity) changes rapidly, the probe also discerns its varia-
 149 tions vs depth, as Y quickly reaches an equilibrium with the thin solder mask protect-
 150 ing its electrodes. Each of the probe’s 15 independent sensors records the real and imag-
 151 inary parts of the complex effective sand dielectric constant ($K'_e - \iota K''_e$), where $\iota^2 =$
 152 -1 , from which the “loss tangent” $\tan \varphi \equiv K''_e/K'_e$ can be inferred (J. D. Jackson, 1999;
 153 Louge et al., 1997). A sensor of characteristic length ℓ_c exposed to air has a capacitance
 154 $\epsilon_0 \ell_c$, where $\epsilon_0 \simeq 8.854 \text{ fF/mm}$ is the permittivity *in vacuo*. Its introduction in a moist
 155 dielectric medium changes its impedance to an equivalent circuit consisting of a resis-
 156 tance $(2\pi f \epsilon_0 K''_e \ell_c)^{-1}$ in parallel with a capacitance $\epsilon_0 K'_e \ell_c$, where f is frequency of the
 157 applied voltage (Louge et al., 2021). Dry sand is a pure dielectric with $K''_e \simeq 0$.

158 As Shahraeeni and Or (2010) showed, van der Waals attraction to the solid and
 159 binding liquid forces hold a thin layer of water molecules on the grain surface to a thick-
 160 ness

$$161 \ell_w = \frac{\ell_0}{[T^* \ln(1/\text{RH})]^{1/3}}, \quad (1)$$

162 with characteristic length

$$163 \ell_0 \equiv \left[\frac{\text{MW}_{\text{H}_2\text{O}}(-H)}{6\pi\rho_w \hat{R}T_{\text{st}}} \right]^{1/3}, \quad (2)$$

164 where RH is relative humidity in the interstitial air surrounding a sand grain, $\text{MW}_{\text{H}_2\text{O}}$
 165 is the molar mass of water, $H < 0$ is an effective Hamaker coefficient, $\hat{R} \simeq 8.314 \text{ J/mole.K}$
 166 is the fundamental gas constant, $\rho_w \simeq 997 \text{ kg/m}^3$ is the density of liquid water, $T_{\text{st}} =$

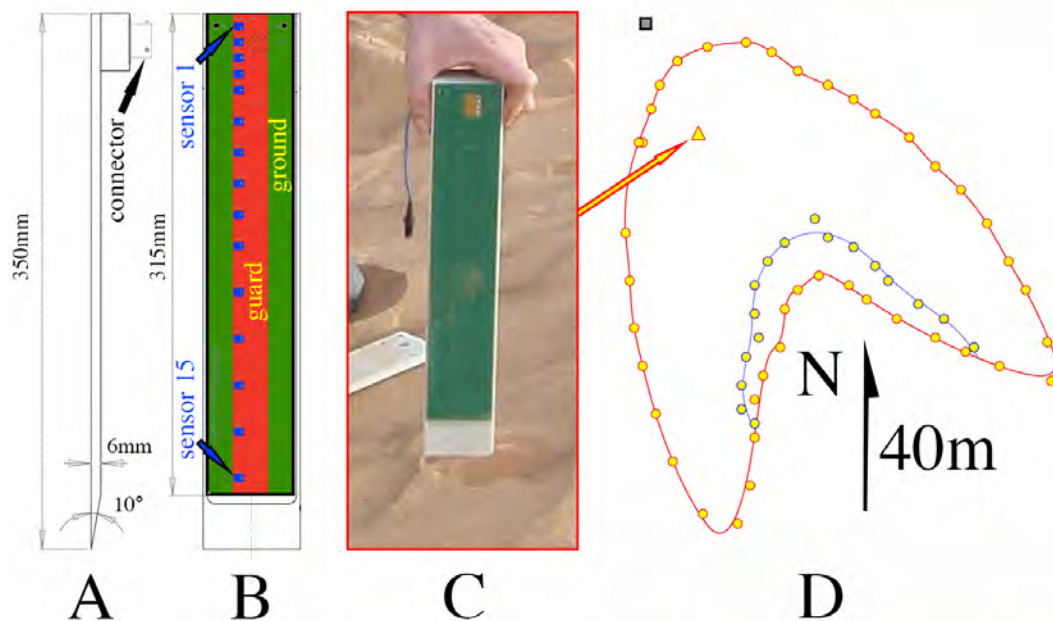


Figure 1. Fifteen-sensor capacitance probe. (A) Side view of the lance showing the rear guarded connector. (B) Front view with superimposed printed circuit board of 15 independent sensors numbered from the surface downward. Blue rectangles are maintained at sensor voltages. Surrounding red and green surfaces hold guard and ground voltages, respectively. (C) The probe before insertion into sands. In the background, a lance of similar geometry is used to assess sand looseness nearby before insertion. (D) GPS-recorded dune outline and brink (red and blue circles, respectively). The yellow triangle and grey square show insertion spot and weather station, respectively. For scale, the North arrow is 40 m-long.

298.15 K is the absolute temperature T at standard conditions, and $T^* \equiv T/T_{\text{st}}$ is its dimensionless counterpart (Iwamatsu & Horii, 1996). This “film adsorption” regime persists until water forms meniscii in small cavities through capillary condensation (Shahraeeni & Or, 2010). As Appendix B shows, the resulting mass fraction of water Ω_e in bulk sand of particle-size distribution f_M at equilibrium with the surrounding RH is given by the “isotherm” relation

$$\Omega_e = \frac{\Omega_1}{[T^* \ln(1/\text{RH})]^{1/3}}. \quad (3)$$

For sands of the dune under study, Louge et al. (2013) measured $\Omega_1 \simeq 0.0013$ in a moisture chamber.

Because Ω_e , or its instantaneous counterpart Ω , are ratios of masses attached to individual grains, they do not depend on the solid volume fraction ν of the sand bed. Similarly, the loss tangent $\tan \varphi$ is weakly dependent on ν (Louge, Valance, el Moctar, & Dupont, 2010), but it rises with Ω . To establish their relation, we covered the probe of Louge, Valance, el Moctar, and Dupont (2010) with a 1 cm-thick layer of Qatar dune sand in a humidity chamber held at $T_c \simeq 35.4^\circ\text{C}$ with relative humidity in the range $0.32 < \text{RH}_c < 0.9$ (Fig. 2). We obtained stable signals until $\text{RH}_c = \text{RH}_{\text{max}} \sim 0.821$, at which point K_e'' became too large. We attribute this maximum RH to the onset of capillary condensation. In the chamber, the loss tangent conformed to

$$\tan \varphi \simeq \tan \varphi_0 \times \text{RH}_c / (1 - \text{RH}_c), \quad (4)$$

where RH_c is the relative humidity around grains during calibration.

As sand temperature T varies substantially below the dune surface (Louge et al., 2013), Eq. (4) must be extrapolated to values of T other than the calibration temperature T_c . To that end, we use Eq. (3) to convert RH_c to $\text{RH}_e = \exp[(T_c/T) \ln \text{RH}_c]$. Substituting Eq. (4), we find the equilibrium RH around grains at T ,

$$\text{RH}_e = \exp \left[- \left(\frac{T_c}{T} \right) \ln \left(1 + \frac{\tan \varphi_0}{\tan \varphi} \right) \right]. \quad (5)$$

Approximating the saturation pressure of water using “Antoine’s law”

$$p_{\text{sat}} \simeq p_{A_0} \exp[-T_{A_a}/(T - T_{A_0})], \quad (6)$$

with $p_{A_0} \simeq 1.24 \cdot 10^{10}$ Pa, $T_{A_a} \simeq 3841.2^\circ\text{K}$ and $T_{A_0} \simeq 45.2^\circ\text{K}$, we convert RH to water vapor mass fraction using

$$Y = \frac{\text{RH}}{M^*(p/p_{\text{sat}}) - \text{RH}(M^* - 1)} \simeq \frac{p_{\text{sat}}}{M^*p} \text{RH}, \quad (7)$$

where $M^* \equiv \text{MW}_{\text{air}}/\text{MW}_{\text{H}_2\text{O}} \simeq 1.61$ is the ratio of the molar masses of air and water.

Louge et al. (2013) recorded sand composition for the dune under study using a QEMscan (Gottlieb et al., 2000), reported it in Appendix E of their supporting information, and verified that Eq. (3) has merit. Other mineral compositions can exhibit qualitatively different isotherms (Shang et al., 1995). However, because the latter have a weaker dependence on temperature than saturation pressure does in Eq. (6), our modeling framework has broad applicability.

3 Temperature profiles

In Appendix C, we calculate the derivatives of Ω_e from the isotherm of Eq. (3). This reveals that the amount of water held on sand grains is a strong function of temperature through the exponential in Antoine’s law (Eq. 6). However, because negligible latent heat is associated with the thin layer in Eq. (1), the heat equation is not affected

210 its adsorption or desorption. In other words, Eq. (6) “one-way-couples” spatio-temporal
 211 variations of Y to T , thereby making it crucial to record subsurface temperature, and
 212 to evaluate its partial derivatives with time and space accurately. Such evaluation first
 213 requires a fit of temperature data that is strictly consistent with the solution of the linear
 214 heat equation in time t and depth x

$$215 \quad \frac{\partial T}{\partial t} = \alpha \frac{\partial^2 T}{\partial x^2}, \quad (8)$$

216 which Louge et al. (2013) satisfactorily integrated subject to the surface boundary con-
 217 dition

$$218 \quad -k_s \frac{\partial T}{\partial x} \Big|_{x=0} = \dot{q}_{\text{rad}}'' + \dot{q}_{\text{wind}}'', \quad (9)$$

219 where α and k_s are, respectively, the effective thermal diffusivity and conductivity of bulk
 220 sand. In Eq. (9), \dot{q}_{rad}'' is the measured net radiation flux striking the dune and \dot{q}_{wind}'' is
 221 the wind-driven convective flux calculated from the Monin-Obukhov model of the cou-
 222 pled momentum and heat atmospheric boundary layers summarized in Appendix D.

223 Rather than adding Eq. (8) to the non-linear set of governing equations to be in-
 224 troduced in section 6, it is more accurate to access time and space derivatives of T by
 225 fitting its record to a sum of four solution harmonics of Eq. (8) (Carslaw & Jaeger, 1959),

$$226 \quad T \simeq T_\infty + \left[\sum_{i=1}^4 T_i \times \mathbb{H}(x, t; i) \right] + T_{1/n} \times \mathbb{H}(x, t; 1/n), \quad (10)$$

227 where

$$228 \quad \mathbb{H}(x, t; i) \equiv \exp \left(-x \sqrt{\frac{i\pi}{J\alpha}} \right) \sin \left[2i\pi \left(\frac{t - t_i}{J} \right) - x \sqrt{\frac{i\pi}{J\alpha}} \right], \quad (11)$$

229 and $J = 24$ hr is the diurnal period. The term $\mathbb{H}(x, t; 1/n)$ is a subharmonic captur-
 230 ing the increase in mean temperature on the second day due to slower wind speed. A
 231 least-squares fit to the data yielded $T_\infty \simeq 297.0^\circ\text{K}$ at large depth,
 232 amplitudes $(T_{1/n}, T_1, T_2, T_3, T_4) \simeq (19.1, 13.5, -5.5, 0.72, 0.65)^\circ\text{C}$,
 233 phase lead times $(t_{1/n}, t_1, t_2, t_3, t_4) \simeq (0.789, 0.313, 0.145, 0.441, 0.052) \times J$, $n \simeq 822$,
 234 and $\alpha \simeq 3.53 \cdot 10^{-7} \text{ m}^2/\text{s}$, which we adopted as the observed sand heat diffusivity. Equa-
 235 tions (8)–(10) suggest that depth and time should be made dimensionless as $x^* \equiv x/\sqrt{\alpha J}$
 236 and $t^* \equiv t/J$, respectively.

237 4 Measurements

238 Figure 3 shows the entire data set, which we submit as supporting information. It
 239 includes vapor mass fractions Y calculated from Eqs. (5)–(7), measured subsurface tem-
 240 peratures T used in Eq. (10), net radiation flux \dot{q}_{rad}'' recorded above the probes, the wind-
 241 driven heat flux through the surface \dot{q}_{wind}'' that Louge et al. (2013) modeled, and wind
 242 speed U at two altitudes upwind of the dune. We will use this record to validate the model
 243 framework in section 6.

244 The first unexpected feature of the mass fraction record consisted of multiple in-
 245 flections vs depth, which have no counterpart in the diffusive heat transfer captured by
 246 Eq. (10). As Fig. 4 and its animation in the supporting information illustrate, Y exhib-
 247 ited an S-shaped profile with a partial minimum that is co-located with the partial min-
 248 imum in T . This suggests that the peculiar inflections of Y were associated with the steep
 249 exponential dependence of saturation pressure on T modeled by Eq. (6) and quantified
 250 in Appendix C. The integration of mass transfer partial differential equations in section 7
 251 will confirm this explanation.

252 A more puzzling observation was sudden jumps in Y , detected from $t^* \simeq 1.4$ to
 253 1.63 on March 20, 2011. In that interval, Y switched from a dry to a humid state in rapid

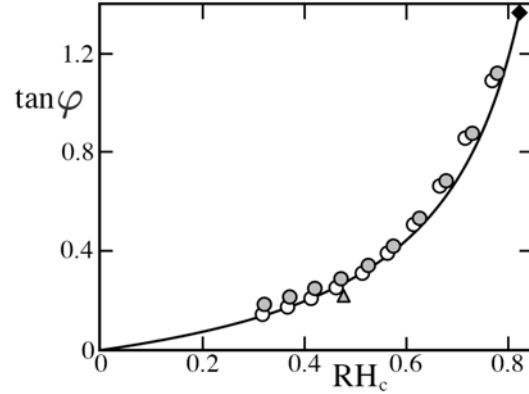


Figure 2. Loss tangent $\tan \varphi \equiv K_e''/K_e'$ vs relative humidity RH_c during consecutive 4 hr plateaus in a moisture chamber calibration at 35.4°C using the capacitance probe of Louge, Valance, el Moctar, and Dupont (2010) at the base of a 1 cm column of Qatar dune sand. The line is Eq. (4) with $\tan \varphi_0 \simeq 0.297$. The diamond marks the largest stable state observed. Ascending and descending RH_c in the chamber are shown as open and filled circles, respectively, thus revealing negligible hysteresis. The filled triangle is another calibration test at 20.9°C , corrected for temperature with Eq. (5), in which the probe of Fig. 1 was covered with sand in the lab. This test lasted long enough for both sand and solder mask to reach equilibrium with the ambient $\text{RH}_c \simeq 0.46$.

254 succession. The onset of this apparent signal bistability coincided with an upstream wind
 255 speed rising above $U \sim 7$ m/s, and it disappeared as U persistently dropped below this
 256 value. During this period, wind occasionally uncovered the top of our probes by a few
 257 millimeters. When this happened, we replenished the missing sand gently by hand to keep
 258 both probes flush with the surface.

259 Later, no such bistability arose during the corresponding period on March 21 ($2.4 \lesssim$
 260 $t^* \lesssim 2.6$), when U remained below 6 m/s, and Y_1 exhibited single values nearly identi-
 261 cal to the more humid state of March 20, implying less efficient surface drying ($Y_1 >$
 262 Y_a). Acoustic detection of sand impact and anemometry carried out on this dune in Janu-
 263 ary 2017 yielded thresholds for particle motion ~ 7 m/s. These observations suggest
 264 that signal bistability was likely associated with intermittent aeolian sand transport.

265 During such transport, mass transfer was enhanced by the presence of saltating parti-
 266 cles, which quickly adopted a value of Ω in equilibrium with the ambient Y_a . Upon their
 267 intermittent deposition, these particles also imposed their lower moisture content on sur-
 268 face grains. Consequently, the drier envelope of water vapor mass fraction Y_1 at the sen-
 269 sor closest to the surface (blue line) was nearly identical to its ambient counterpart Y_a
 270 recorded independently at the weather station (black line). (The coincidence of Y_1 and
 271 Y_a , which were measured by instruments of widely different principles, also speaks to the
 272 accuracy of the capacitance probes). Without deposition of dry saltating sands, Y_1 re-
 273 verted to the mass fraction $> Y_a$ that grains normally held at the surface. Note that
 274 we rarely observed an intermediate mass fraction between high and low states. Instead,
 275 the abrupt transition between them likely arose from rapid variations in saltation solid
 276 volume fraction, which typically accompany the passage of sharp edges of particles clus-
 277 ters meandering above the dune.

278 Remarkably, these perturbations in Y_1 recorded at the surface propagated quickly
 279 and deeply. This suggests that mass transfer was governed by two widely different time

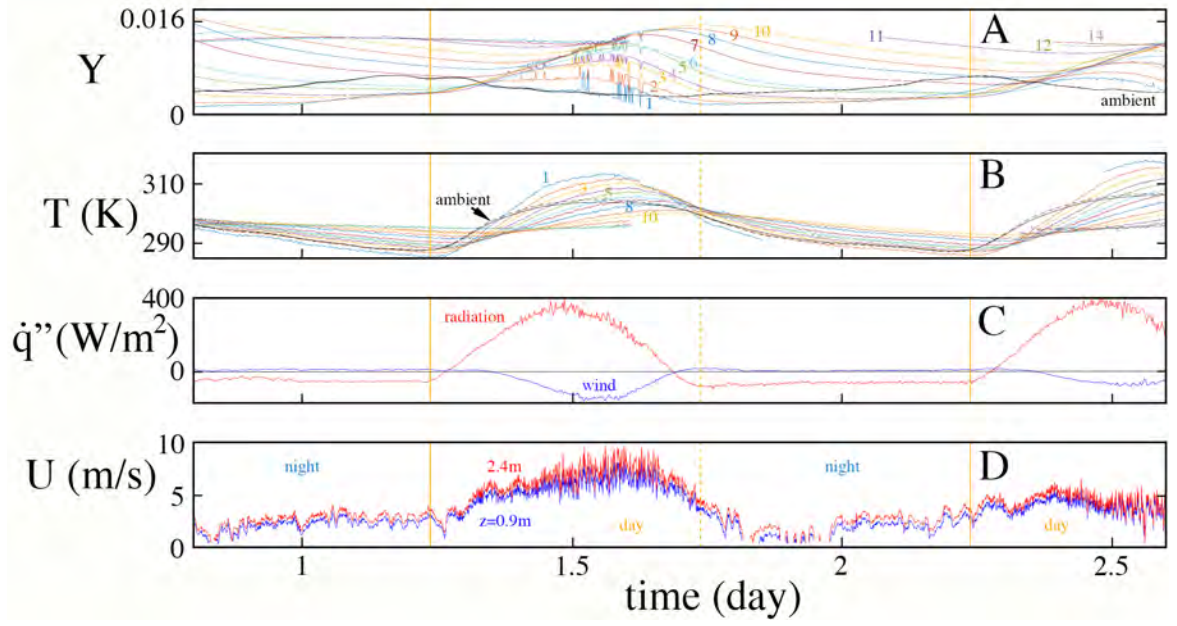


Figure 3. Measurements of March 19-21, 2011. Animations, probe depths and data are provided as supporting information. (A) Vapor mass fraction Y recorded by capacitance sensors of indices in Fig. 1, with matching line colors; black dashed and solid lines are ambient Y_a from the weather station at altitudes $z_B = 0.9$ m and $z_T = 2$ m, respectively. Values of Y appear as grey symbols in the movie **MovieDuneSubsurfaceTemperature&VaporMassFraction.mp4**. (B) Subsurface temperatures T recorded by the shorter probe of Louge et al. (2013) (increasing indices downward), and appearing as yellow symbols in **MovieDuneSubsurfaceTemperatureRadiation&Wind.mp4**. Black dashed and solid lines are ambient temperatures T_B and T_T at z_B and z_T , respectively. (C) Net thermal fluxes by radiation (red) and wind-driven convection (blue) at the dune surface, positive along depth x into the dune. \dot{q}''_{wind} is calculated as explained in the supporting information of Louge et al. (2013) with relative shear velocity $v_\tau/U \simeq 0.036$ and roughness $z_0 \simeq 16 \mu\text{m}$ recorded at the probe location in January 2017. (D) Wind speeds at the weather station at $z = 0.9$ m (blue) and 2.4 m (red) with 0.3 m/s detection threshold. The common abscissa is time t^* dimensionless with $J = 24$ hr, with origin at 00:00 Qatar time (GMT+3) on March 19, 2011. The vertical solid and dashed orange lines mark sunrise and sunset, respectively. Missing data are due to excessive K_e'' that induced spurious signals from the capacitance electronics at LF radio frequencies that contaminated both records of Y and T .

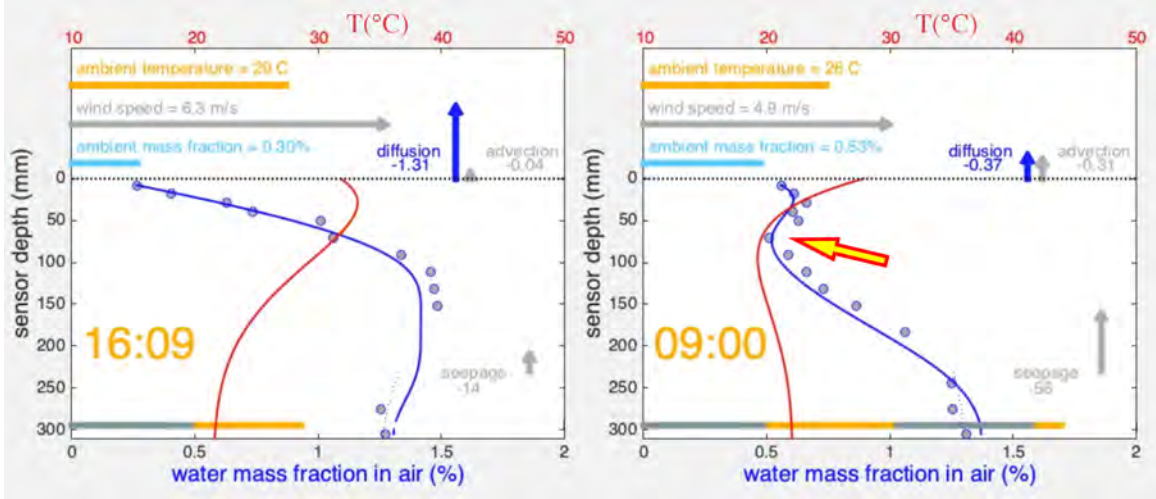


Figure 4. Snapshots of `MovieDuneSubsurfaceTemperature&VaporMassFraction.mp4` available as supporting information, showing subsurface depth profiles of temperature in $^{\circ}\text{C}$ (Eq. 10, red line) and vapor mass fraction Y_e at equilibrium with the measured Ω (grey symbols) at 16:09 Qatar time ($t^* \simeq 1.67$) on March 20 (left) and 09:00 ($t^* \simeq 2.38$) on March 21 (right). The blue line is the model implemented in section 10. The yellow arrow points to co-located partial minima in the Y - and T -profiles. Bars and arrows represents scalars and vectors with lengths proportional to ambient temperature, wind speed, ambient water vapor mass fraction, dimensionless surface fluxes of vapor diffusion $\Psi_s^*/(1 - \nu)$ and vapor advection $u_s^* Y_s p^*/T_s^*$ defined in section 8. On the thin dotted line drawn for $x > 220$ mm, the vapor mass fraction Y is at equilibrium with a constant $\Omega = 1.65 \Omega_1$. The horizontal dotted line marks the sand surface. The horizontal grey and orange timeline indicates progression along the March 19-21 record.

280 scales, namely the diurnal period J that regulates the smooth evolution of Y and T , and
 281 a much shorter one that allowed the rapid propagation of waves carrying surface distur-
 282 bances to the subsurface. Section 12 will develop a stability analysis explaining this be-
 283 havior.

284 Above the dune, wind speed rose during the day as soon as a net radiation flux stroke
 285 the desert floor (Wyngaard, 2010). An unstable atmospheric boundary layer (ABL) then
 286 developed, in which ambient temperature grew with elevation, but remained lower than
 287 its counterpart on the surface. As the radiation flux turned upward before sunset, so did
 288 the gradient of ambient temperature. During the night, surface temperature was lower
 289 than the ambient, and both progressively decreased in tandem. Low-level jets intermit-
 290 tently perturbed the nocturnal stable boundary layer (Banta et al., 2007; Klein et al.,
 291 2016).

292 The absence of significant noise in our capacitance record allowed us to differenti-
 293 ate spatio-temporal variations of Y and use Fick's law to calculate the vapor mass flux
 294 $\Psi_s'' = -\rho(1 - \nu)(D/\varpi)(\partial Y/\partial x)_s$ at the sand surface, where D is the diffusion coeffi-
 295 cient of water vapor at temperature T and ϖ is the tortuosity of porous sand (Shen &
 296 Chen, 2007). As section 8 will show, this flux was augmented by a slow "seepage" ad-
 297 vection within the pore space driven by wind blowing over topographical variations of
 298 the dune. Together, diffusion and advection fluxes provided a boundary condition for
 299 the ABL above our instruments.

5 Stratigraphy

By recording both K'_e and K''_e , the capacitance probe yielded not only Ω through K''_e/K'_e , but also the time-invariant local “bulk density” $\rho_b \simeq \rho_p \nu$ at each sensor, where ν is the solid volume fraction and ρ_p the material density of sand grains. As Louge, Valance, el Moctar, and Dupont (2010) showed, K'_e is approximated by the model of Böttcher and Bordewijk (1978),

$$K'_e = \frac{1}{4} \left\{ 2 - K_p + 3\nu(K_p - 1) + \sqrt{8K_p + [2 - K_p + 3\nu(K_p - 1)]^2} \right\}, \quad (12)$$

where K_p is an equivalent material dielectric constant that rises with Ω , and therefore with $\tan \varphi$. Rather than evaluating K_p by staging several volume fractions in the laboratory, we found it more convenient to derive it directly from field data. In this method, we model K_p as

$$K_p \simeq k_0 + k_1 \tan \varphi + k_2 \tan^2 \varphi + k_3 \tan^3 \varphi. \quad (13)$$

From Eq. (12), K'_e and $K''_e = \tan \varphi \times K'_e$ become, respectively, the functions f' and f'' of the variables ($\nu_i; \tan \varphi_j; k_0, k_1, k_2, k_3$) recorded at sensor of index i and time j . The values of k_0 through k_3 and ν_1 through ν_{15} are those yielding the smallest cost function \mathcal{C} from the entire data set of $N = 11557$ valid points acquired with all sensors,

$$\mathcal{C}(\nu_1, \nu_2, \dots, \nu_{15}; k_0, k_1, k_2, k_3) = \sum_{j=1}^N \sum_{i=1}^{15} [K'_e(i, j) - f']^2 + [K''_e(i, j) - f'']^2. \quad (14)$$

Adding terms of order higher than $\tan^3 \varphi$ in Eq. (13) (k_4, k_5 , etc) did not reduce \mathcal{C} and thus improve results.

As Fig. 5 shows, the first 14 sensors spanned a wide enough range of $\tan \varphi$ to discern variations of ν with depth. Typically, such variations are associated with layers sorted and deposited by successive avalanches on the downwind face of the mobile dune (Kocurek, 1991; Harari, 1996; Kleinhans, 2004; Bristow et al., 2007; Reesink & Bridge, 2009; Fan et al., 2012; Qian et al., 2014), then sequestered for several months until aeolian transport uncovers them upwind (Louge et al., 2013). On other visits to the same sand dune, the imprint of earlier positions of the lee face was visible for a short time after rain (Fig. 5C), suggesting preferential liquid penetration (Al-Shukaili et al., 2019). A complex layered stratigraphy was also evident upon excavation (Fig. 5A).

At the specific location of our measurements, Fig. 5 reveals relatively light sands with higher bulk density on the surface than below, consistent with the soft region that we selected for easy insertion of the probes. Its inset B also hints at an uneven stratigraphy on a wavelength $\Delta x \sim 3$ to 5 cm. Because the upwind and downwind faces of the dunes made angles of $\theta_u \simeq 7^\circ$ and $\theta_d \simeq 31^\circ$ from the horizontal, our capacitance probe inserted approximately normal to the surface along x detected strata separated by a distance $\Delta x \cos(\theta_u + \theta_d) \simeq 2$ to 4 cm. Finally, although the profile in Fig. 5B resembled the layering shown in insets A and C, the Böttcher model of Eq. (12) likely underestimated ν .

6 Modeling framework

Water evaporation from sands is complicated by capillary forces retaining liquid within its porous structure (Prat, 2002; Lehmann & Or, 2009; Or et al., 2013). Its analysis in the vadose zone therefore requires a model for the hysteretic process of wetting and draining in the unsaturated porous medium (Xu & Louge, 2015), typically obtained by invoking an empirical expression for the water retention curve (Vanderborght et al., 2017; Kamai & Assouline, 2018; Assouline & Kamai, 2019; Shao et al., 2021).

The process is simpler near the surface of hyper-arid deserts, where water exists either as a vapor, or as a film directly adsorbed on solid grains (Shahraeeni & Or, 2010).

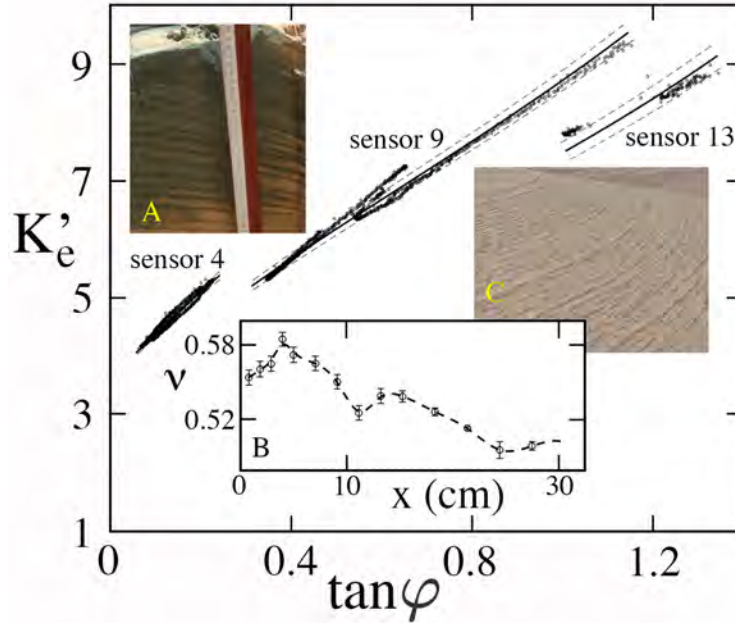


Figure 5. Real part of the effective dielectric constant K'_e vs loss tangent $\tan \varphi$ for all valid data points (small circles), shown for sensor 4, 9 and 13. The line is the Böttcher model in Eq. (12) obtained with coefficients $(k_0, k_1, k_2, k_3) \simeq (6.7, 20, -7.2, 3.9)$ from Eq. (13) and volume fractions at all 15 sensors that minimize the cost function in Eq. (14). Dashed lines above and below the main fit, as well as error bars in inset B, mark \pm one sample standard deviation in ν at the corresponding sensor. Inset A: an excavation conducted in April 2014 reveals a layered stratigraphy after pouring water laced with blue food coloring through the surface. The stratigraphy occasionally appears on the surface after rain partially dries up (inset C, picture taken on the same dune in January 2014). Inset B: profile of ν vs depth x (cm) perpendicular to the dune surface, calculated from Eqs. (12)–(14). The dashed line is a visual spline through the data.

346 Here, the drying front that Shokri et al. (2008) and Lehmann et al. (2008) documented
 347 lies deeper withing the dune, and mass transfer near the surface conforms to the last stage
 348 of the evaporation process (Shahraeeni et al., 2012).

349 Such was the case for the data set of section 4, which suggested a strong spatio-
 350 temporal coupling between subsurface variations of vapor mass fraction and tempera-
 351 ture, a situation that is difficult to reproduce in laboratory experiments on the drying
 352 process (Davarzani et al., 2014; Gao et al., 2018; Z. Li et al., 2020).

353 In this section, we derive a set of governing equations to interpret these observa-
 354 tions in the limit where interstitial water vapor is at equilibrium with water adsorbed
 355 on solid grains. We will use their framework to identify the principal mechanisms of mois-
 356 ture transport in the dune subsurface, and dismiss those that are negligible.

357 In the gas phase, the balance of total mass in an elementary slice of sand at depth
 358 x is

$$359 \quad (1 - \nu) \frac{\partial \rho}{\partial t} + (1 - \nu) \frac{\partial (\rho u)}{\partial x} = -\rho_p \nu \frac{\partial \Omega}{\partial t}, \quad (15)$$

360 where the right-hand term represents the rate of evaporation from grains of material den-
 361 sity ρ_p on which water was adsorbed, later considered in section 11 and Appendix G. The
 362 variables ρ , u , Ω and ν in this classical mass balance (Kays & Crawford, 1980; Bird et
 363 al., 2007) are implicitly coarse-grained on the scale of a few particles, as suggested by T. B. An-
 364 derson and Jackson (1967). For clarity of derivations, we ignore relatively small varia-
 365 tions of ν mentioned in section 5, so $(1 - \nu)$ can be brought out of the spatial deriva-
 366 tive. However, prior knowledge of a stratigraphy like that shown in Fig. 5 can be sub-
 367 stituted in the governing equations and its numerical solutions.

368 In Eq. (15), the density of humid air $\rho = \rho_{\text{H}_2\text{O}} + \rho_{\text{air}}$ is the sum of the partial
 369 densities of water vapor $\rho_{\text{H}_2\text{O}} \equiv \rho Y = \text{MW}_{\text{H}_2\text{O}} \chi_{\text{H}_2\text{O}} (p/\hat{R}T)$ and dry air $\rho_{\text{air}} = \text{MW}_{\text{air}} \chi_{\text{air}} (p/\hat{R}T)$,
 370 with complementary mole fractions of water and air $\chi_{\text{H}_2\text{O}} + \chi_{\text{air}} = 1$, so vapor mass
 371 fraction is $Y = \chi_{\text{H}_2\text{O}} \text{MW}_{\text{H}_2\text{O}} / [\chi_{\text{H}_2\text{O}} \text{MW}_{\text{H}_2\text{O}} + \chi_{\text{air}} \text{MW}_{\text{air}}]$. Meanwhile, dry air den-
 372 sity $\rho_{\text{air}} = \rho_{\text{st}} p^* / T^*$ can be expressed in terms of its counterpart $\rho_{\text{st}} \simeq 1.185 \text{ kg/m}^3$
 373 under standard conditions at $T_{\text{st}} = 298.15 \text{ }^\circ\text{K}$ and $p_{\text{st}} = 1.013 \times 10^5 \text{ Pa}$, where $p^* \equiv$
 374 p/p_{st} and $T^* \equiv T/T_{\text{st}}$ are dimensionless absolute pressure and temperature, respectively.
 375 Using these relations, moist air density is

$$376 \quad \rho = \rho_{\text{st}} \frac{p^* / T^*}{1 + Y(M^* - 1)}, \quad (16)$$

377 where $M^* \equiv \text{MW}_{\text{air}} / \text{MW}_{\text{H}_2\text{O}}$. Because $Y(M^* - 1) \ll 1$, ρ is almost equal to the den-
 378 sity of air at the same p and T . Therefore, although numerical solutions will adopt Eq. (16),
 379 we will lighten derivations in this article by simply writing $\rho \simeq \rho_{\text{st}} p^* / T^*$.

380 The ‘‘seepage’’ interstitial gas velocity u is given by Darcy’s law

$$381 \quad u = -\frac{K}{\mu(1 - \nu)} \frac{\partial p}{\partial x} \quad (17)$$

382 in terms of the local gradient of pressure p and air dynamic viscosity μ . In a bed of equally-
 383 sided randomly-packed spheres at the solid volume fraction ν , the permeability K may
 384 be approximated as

$$385 \quad \frac{K}{(1 - \nu)} \simeq \frac{d^2}{150} \left(\frac{1 - \nu}{\nu} \right)^2, \quad (18)$$

386 and, because liquid water is not involved, the expression of K need not be corrected for
 387 its presence (Brooks & Corey, 1964). In this work, we also ignore variations of p with
 388 time and, because we did not record atmospheric pressure during this campaign, we as-
 389 sume $p \simeq p_{\text{st}}$ without significant consequence for our results. Nonetheless, we consider
 390 pressure *gradients* in sand, which drive the seepage velocity u through Eq. (17).

391 Meanwhile, as derived by (Kays & Crawford, 1980; Bird et al., 2007), a balance of
 392 water vapor yields

$$393 \quad (1 - \nu) \frac{\partial \rho_{\text{H}_2\text{O}}}{\partial t} + (1 - \nu) \frac{\partial}{\partial x} \left[\rho_{\text{H}_2\text{O}} u - \frac{\rho D}{\varpi} \left(\frac{\partial Y}{\partial x} + a_T Y \frac{\partial \ln T}{\partial x} \right) \right] = -\rho_p \nu \frac{\partial \Omega}{\partial t}, \quad (19)$$

394 where

$$395 \quad \rho_{\text{H}_2\text{O}} = \rho Y \quad (20)$$

396 is the partial density of water vapor. In the bracket within the spatial derivative, $(\rho_{\text{H}_2\text{O}} u)$
 397 represents vapor advection, and $(\rho D/\varpi) \partial Y/\partial x$ is the Fickian diffusion flux, where ϖ is
 398 the ‘‘tortuosity’’ of the longer path taken by diffusion around grains (Shen & Chen, 2007).
 399 Because desert sands possess strong subsurface temperature gradients, we include the
 400 Soret diffusion term $(\rho D/\varpi) a_T Y \partial \ln T/\partial x$ (Chapman & Cowling, 1953; Hudson et al.,
 401 2007), and we evaluate the coefficient a_T in Appendix E. We will later see that this term
 402 is negligible. However, such diffusion may become important in extra-terrestrial envi-
 403 ronments.

404 Another gradient-driven process may be natural convection within the porous medium
 405 of permeability K over a typical distance Δx , characterized by the Rayleigh number $\text{Ra} =$
 406 $K g \Delta x (\Delta T/T) / [\alpha_m (\mu/\rho)]$ (Elder, 1967), where g is gravitational acceleration and $\alpha_m \equiv$
 407 $k_s / (\rho c_p)$ combines the effective thermal conductivity $k_s \simeq 0.49 \text{ W/m}\cdot\text{K}$ of the sand
 408 bed with the density of air and its specific heat $c_p \simeq 1000 \text{ J/kg}\cdot\text{K}$. Taking the high-
 409 est observed temperature excursion $\Delta T < 20^\circ \text{C}$ over $\Delta x < 20 \text{ cm}$, we find $\text{Ra} < 0.006$,
 410 which is much too small for natural convection to matter.

411 Expanding derivatives in Eq. (19) and combining with the overall mass conserva-
 412 tion (15), we find

$$413 \quad \rho(1 - \nu) \frac{\partial Y}{\partial t} + \rho u(1 - \nu) \frac{\partial Y}{\partial x} - (1 - \nu) \frac{\partial}{\partial x} \left[\rho \frac{D}{\varpi} \left(\frac{\partial Y}{\partial x} + a_T Y \frac{\partial \ln T}{\partial x} \right) \right] = -\rho_p \nu \frac{\partial \Omega}{\partial t} (1 - Y). \quad (21)$$

414 In this equation, the first term on the left hand side captures the rate of change of wa-
 415 ter vapor mass fraction. The second term models seepage advection at the interstitial
 416 velocity u . The third term arises from molecular diffusion of water vapor in air with co-
 417 efficient D .

418 Because temperature varies substantially through depth (Louge et al., 2013), it is
 419 important to account for variations of D with T , and to keep it within the spatial deriva-
 420 tive in Eq. (21). Neglecting the dependence of ρ on Y in Eq. (16),

$$421 \quad \rho D \simeq \rho_{\text{st}} D_{\text{st}} T^{*n_d}, \quad (22)$$

422 where $D_{\text{st}} \simeq 2.576 \cdot 10^{-5} \text{ m}^2/\text{s}$ and $n_d \simeq 0.861$, close to the 1/2 exponent predicted by
 423 the kinetic theory of hard spheres (Chapman & Cowling, 1953).

424 The volumetric rate of water evaporation $\rho_p \nu \partial \Omega/\partial t$ is driven by the difference be-
 425 tween the instantaneous vapor mass fraction Y in the interstitial space of density $\rho(1 -$
 426 $\nu)$ surrounding sand grains, and the surface mass fraction Y_e at equilibrium with the ac-
 427 tual Ω that they hold,

$$428 \quad \rho_p \nu \frac{\partial \Omega}{\partial t} = \frac{\rho(1 - \nu)}{\tau} (Y - Y_e), \quad (23)$$

429 In section 11, we will derive this expression using the Hertz-Knudsen-Schrage (HKS) the-
 430 ory (Marek & Straub, 2001), and show that the characteristic time τ is governed by ki-
 431 netics of an evaporation reaction at the grain scale. On the period $J = 24 \text{ hr}$ of diur-
 432 nal variations, τ is $\ll J$, so grains have ample time to reach equilibrium. However, as
 433 section 12 will discuss, rapid variations of Y associated with aeolian transport may be
 434 too fast for particles to adjust instantly to a new equilibrium, leading to internal waves.

7 Equilibrium regime

In general, there are two regimes arbitrated by the time scale δt of Y , T and Ω variations relative to τ . If $\delta t \gg \tau$, all particles have reached equilibrium irrespective of size, so $\Omega \simeq \Omega_e$. In this “equilibrium regime”, $\partial\Omega/\partial t \simeq \partial\Omega_e/\partial t$ may be expressed in terms of partial derivatives of T , Y and p using functions f_T , f_Y and f_p derived in Appendix C,

$$\frac{\partial\Omega_e}{\partial t} \equiv \Omega_1 \left[\frac{f_T}{T_{\text{st}}} \frac{\partial T}{\partial t} + f_Y \frac{\partial Y}{\partial t} + \frac{f_p}{p_{\text{st}}} \frac{\partial p}{\partial t} \right], \quad (24)$$

where Eq. (3) is the sand isotherm averaged over the particle size distribution. Because these functions all depend strongly on temperature, either explicitly or through p_{sat} , the term $\partial\Omega_e/\partial t$ couples spatial and temporal variations in T and Y , ultimately leading to multiple inflexions in the Y -profile (Fig. 4). With $\partial\Omega/\partial t \simeq \partial\Omega_e/\partial t$, the right-hand source term in Eq. (21) augments its unsteady counterpart to the left,

$$\begin{aligned} \rho(1-\nu) \frac{\partial Y}{\partial t} + \rho_p \nu \frac{\partial \Omega}{\partial t} (1-Y) \\ \simeq \rho(1-\nu) \left[1 + \frac{\rho_p \nu \Omega_1}{\rho(1-\nu)} f_Y (1-Y) \right] \frac{\partial Y}{\partial t} + \rho_p \nu \Omega_1 (1-Y) \frac{f_T}{T_{\text{st}}} \frac{\partial T}{\partial t}. \end{aligned} \quad (25)$$

Defining $\mathbb{R} \equiv \rho_p \nu / [\rho_{\text{st}}(1-\nu)]$ and $u^* \equiv u \sqrt{J/\alpha}$, recalling Eq. (22) and $\rho_{\text{st}}/\rho \simeq (T^*/p^*)$, dividing by $(1-\nu)\rho_{\text{st}}$ and reintroducing $t^* = t/J$, and $x^* = x/(\alpha J)^{1/2}$, Eq. (21) has the dimensionless form

$$\begin{aligned} \frac{p^*}{T^*} \left\{ \left[1 + \mathbb{R} \Omega_1 \frac{T^*}{p^*} f_Y (1-Y) \right] \frac{\partial Y}{\partial t^*} + \mathbb{R} \Omega_1 \frac{T^*}{p^*} f_T (1-Y) \frac{\partial T^*}{\partial t^*} \right\} + \\ \frac{p^*}{T^*} u^* \frac{\partial Y}{\partial x^*} - \mathbb{L} \frac{\partial}{\partial x^*} \left\{ T^{*n_d} \left(\frac{\partial Y}{\partial x^*} + a_T Y \frac{\partial \ln T^*}{\partial x^*} \right) \right\} = 0, \end{aligned} \quad (26)$$

where $\mathbb{L} \equiv D_{\text{st}}/(\varpi\alpha)$ is a hybrid Lewis number comparing interstitial vapor diffusivity with thermal diffusivity through bulk sand. With a tortuosity estimate for spheres $\varpi \sim \pi/2$ (Shen & Chen, 2007), $\mathbb{L} \simeq 46.5$. With $\rho_p \simeq 2630 \text{ kg/m}^3$ and $\nu \simeq 0.545$, $\mathbb{R} \simeq 2660$. For the entire data set, $-51 < f_T < -1.2$ and $19 < f_Y < 210$. Therefore, in the unsteady term in straight brackets of Eq. (26), the expression

$$\mathbb{R} \Omega_1 \frac{T^*}{p^*} f_Y (1-Y) \simeq \mathbb{R} \Omega_1 \frac{T^*}{p^*} f_Y \gg 1 \quad (27)$$

is very large. To illustrate the significance of this inequality, consider an isobaric and isothermal system without seepage at $Y \ll 1$. In this hypothetical situation, the dimensional version of Eq. (26) could be approximated as

$$\frac{\partial Y}{\partial t} \simeq \left[\frac{D/\varpi}{\mathbb{R} \Omega_1 (T^*/p^*) f_Y} \right] \frac{\partial^2 Y}{\partial x^2}. \quad (28)$$

If such system, unlike sand, also exhibited a linear isotherm $\Omega = \Omega_{p_0} + \Omega_{p_1} \times \text{RH}$, as is the case in pharmaceutical powders (Louge et al., 2021), which *absorb*, rather than *adsorb* water, differentiating the isotherm (Appendix C) would yield an approximately invariant $f_Y = \partial \text{RH}/\partial Y \simeq pM^*/p_{\text{sat}} \gg 1$, and Eq. (28) would govern an unsteady diffusion with apparent coefficient $D_{\text{eff}} \simeq (D/\varpi)/[\mathbb{R} \Omega_{p_1} (p_{\text{st}}/p_{\text{sat}}) T^* M^*]$, much smaller than its counterpart without water adsorption on grains (or absorption within them). In that case, the mass fraction in a powder initially at $Y = Y_i$ subject to $Y = Y_s$ at the surface of a half-space would evolve as $Y = Y_s - (Y_s - Y_i) \text{erf}(x/2\sqrt{D_{\text{eff}} t})$. In short, grain adsorption (or absorption) would result in much slower diffusive behavior.

For sands, the isotherm in Eq. (3) is more complicated, with $f_Y \propto 1/Y$, thereby precluding a simple closed-form solution. However, on long time scales $\delta t \gg \tau$, the source term $\partial\Omega_e/\partial t$ also acts as an inhibitor of diffusion, as successive layers in an initially dehydrated sand must adsorb water before letting the vapor diffuse deeper. If we ignored

477 the subtlety of $f_Y \propto 1/Y$ for our own data set, the range of f_Y would roughly imply
 478 that the apparent D_{eff} is 70 to 730 times weaker than D . Similar observations are found
 479 in moisture-absorbing pharmaceutical powders (Louge et al., 2021). Louge, Valance, Babah,
 480 et al. (2010) did not consider such hindered diffusion. However, because they derived the
 481 steady distribution of moisture through sand ripples, their model needs no repair, un-
 482 less sand is exposed to rapid variations in surface moisture.

483 While temperature variations described in section 3 conformed to the linear partial
 484 differential equation (PDE) (8), the corresponding model of vapor mass fraction in
 485 Eq. (26) is highly non-linear, as it strongly couples Y to subsurface variations in T . An-
 486 other complication is a variable advection flow within the dune subsurface, which we con-
 487 sider next.

488 8 Seepage

489 It would not be straightforward to measure the small interstitial velocity u in the
 490 field. However, the recorded mass fraction Y (Fig. 3) exhibits so little noise that its tem-
 491 poral derivative can be reliably evaluated using a smoothing spline. Then, it is possible
 492 to fit the value of u^* at each recorded time step by transforming the governing PDE (26)
 493 into an ordinary differential equation (ODE) where the unsteady term $\mathbb{U}_M + \mathbb{U}_T$ is cal-
 494 culated from data,

$$495 \quad \mathbb{U}_M \equiv \left[\frac{p^*}{T^*} + \mathbb{R}\Omega_1 f_Y (1 - Y) \right] \frac{\partial Y}{\partial t^*} \simeq \mathbb{R}\Omega_1 f_Y (1 - Y) \frac{\partial Y}{\partial t^*}, \quad (29)$$

$$496 \quad \mathbb{U}_T \equiv \mathbb{R}\Omega_1 f_T (1 - Y) \frac{\partial T^*}{\partial t^*}.$$

497 Rearranging Eq. (26) and replacing $\partial^2 T^* / \partial x^{*2}$ by $\partial T^* / \partial t^*$ using the heat equation, we
 498 find the ODE

$$499 \quad \frac{d^2 Y}{dx^{*2}} + \frac{dY}{dx^*} \left[n_d \frac{\partial \ln T^*}{\partial x^*} - \frac{p^* u^*}{\mathbb{L} T^{*n_d+1}} \right] \quad (30)$$

$$500 \quad + a_T Y \left[\frac{d \ln Y}{dx^*} \times \frac{\partial \ln T^*}{\partial x^*} + \frac{\partial \ln T^*}{\partial t^*} + (n_d - 1) \left(\frac{\partial \ln T^*}{\partial x^*} \right)^2 \right] = \frac{\mathbb{U}_M + \mathbb{U}_T}{\mathbb{L} T^{*n_d}},$$

501 which we integrate subject to the measured Y at depths x_1^* and x_{10}^* of sensors 1 and 10
 502 using the two-point boundary value toolbox `bvp4c` of MATLAB. For consistency, we limit
 503 the integration to the interval $[x_1^*, x_{10}^*]$, since moisture on sensors 11 to 15 is sometimes
 504 too large for the probe to return a stable measurement of Y (Fig. 3). Using the simplex
 505 search method of Lagarias et al. (1998), which is implemented as `fminsearch` in MAT-
 506 LAB, we repeat the integration of ODE (30) for several values of u^* until the root-mean-
 507 square (rms) difference between signal and prediction is minimized.

508 Figure 6 illustrates this procedure. It is best viewed in the animation **MovieCal-**
 509 **culatationDuneSeepageVelocity.mp4** available as supporting information. In this Fig.,
 510 the left graph shows the profile of least rms error, as well as fits of u^* to $\pm 7\%$ excur-
 511 sions in Y , which we use as uncertainty estimates in u^* . These excursions enclose spa-
 512 tial oscillations of relatively small amplitude in Y , which may be associated with the mild
 513 stratigraphy shown in Fig. 5. The corresponding uncertainties in u^* (dashed lines in Fig. 7)
 514 are small. The integration of ODE (30) fails with $u^* = 0$ (dashed lines), thereby con-
 515 firming that seepage advection is essential.

516 Shao et al. (2021) agreed with these observations. They suggested that a small ad-
 517 vection on the order of $100 \mu\text{m/s}$ is necessary to capture data, and that thermal processes
 518 are crucial. However, by ignoring the soil's isotherm, Shao et al. (2021) had to adopt heuris-
 519 tic closures for the local evaporation rate, and they could not relate the apparent dif-
 520 fusion coefficient D_{eff} to its known counterpart D for water vapor in air. In addition, the

spatial resolution and accuracy of their time-domain reflectometry (TDR) was not sufficient to discern subtle variations in equilibrium vapor mass fraction that are needed to evaluate seepage time-history. They reported $5.4 \cdot 10^{-3} < \theta_w < 8.2 \cdot 10^{-3}$, where $\theta_w \simeq (\rho_p \nu / \rho_w) \Omega$ is water volume fraction. Combining Eqs. (3) and (7), and using properties of our sands as a rough estimate, their smallest detected $\theta_{w_{\min}} \simeq 5.4 \cdot 10^{-3}$ translates to a vapor mass fraction $Y_{\min} \simeq 0.02$, which is well over an order of magnitude larger than what our own capacitance probe discerned ($Y_{\min} \simeq 0.0012$).

The right graph of Fig. 6 also shows relative magnitudes of the two contributions \mathbb{U}_M and \mathbb{U}_T to the total unsteady term. At long diurnal time scales for which grains achieve equilibrium with the surrounding Y , these terms are dominated by the rate $\partial\Omega/\partial t^*$ of the moisture exchange between solid and gas, ultimately captured by the functions f_T and f_Y derived in Appendix C. Because \mathbb{U}_M and \mathbb{U}_T often have opposite signs but similar magnitudes, temporal variations of mass fraction and temperature are both crucial, and they compete to govern vapor transfer through the dune subsurface.

A subtlety is that the seepage velocity u^* varies along x^* in response to density changes arising from temperature, pressure or the release of water vapor. Appendix F provides the corresponding ODEs (F1)–(F2), which we solve using MATLAB’s ODE45 4-th order Runge-Kutta algorithm, subject to dimensionless seepage velocity $u^* = u_s^*$ and pressure $p^* = p_s^*$ at the surface (subscript s), once Y and its derivatives have been obtained from the solution of Eq. (30).

Insets in Fig. 7 show the resulting profiles as solid lines, while dashed lines indicate calculations with $f_Y = f_T = 0$. Contrasting predictions with and without these functions underscores how the rate of water vapor release $\partial\Omega/\partial t^*$ affects u^* . Under planetary conditions where ambient pressure is small or gradients are large, ODEs (30) and (F1)–(F2) may be coupled strongly enough that the evolution of Y , p and u^* with x^* would require their simultaneous solution. However, for this dune, depth variations in u^* (solid lines) are small, and so it is legitimate to assume $u^* \simeq u_s^*$. A consequence is that seepage is not directly affected by internal gradients of temperature or mass fraction. Instead, as the next section articulates, it is likely due to wind-driven variations of surface pressure.

In short, integration of ODE (30) yields our best estimate of the dimensionless instantaneous velocity

$$v_s^* = +(1 - \nu)u_s^* \quad (31)$$

counted > 0 into sand from the atmospheric boundary layer (ABL). By fitting the recorded depth profile of Y with a smoothing spline and differentiating the result at the surface, we also evaluate the diffusive vapor flux $\dot{\Psi}_s'' = -\rho(1 - \nu)(D/\varpi)(\partial Y/\partial x)_s$ across the surface, counted > 0 into sand. Made dimensionless with $\rho_{st}\sqrt{\alpha/J}$, this flux

$$\Psi_s^* = -(1 - \nu)\mathbb{L}T_s^{*nd}(\partial Y/\partial x^*)_s, \quad (32)$$

augmented by the advection $u_s^*Y_s p^*/T_s^*$, contributes to the surface boundary condition for the ABL, which we will examine in section 13.

9 Origin of seepage

Louge, Valance, Babah, et al. (2010) recognized that wind-driven seepage advects moisture and dust through sand ripples by letting the Bernoulli effect induce a higher static pressure at their troughs than at their crests. Gao et al. (2018) staged a wavy surface to investigate its role in drying. By deploying a porous plastic ripple with harmonic amplitude h_0 and wavelength λ_0 in a wind tunnel, Musa et al. (2014) confirmed that the pore pressure gradient driving this advection scales as $\rho U^2 h_0 / \lambda_0^2$, where U is the bulk wind speed. With origin above the trough at mid-depth between trough and crest, they

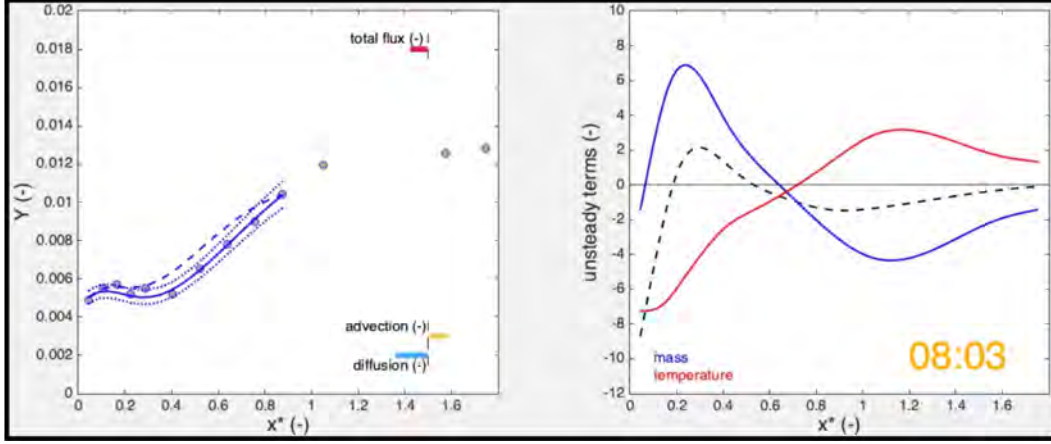


Figure 6. Snapshots of `MovieCalculationDuneSeepageVelocity.mp4` available as supporting information. Left: best fits (lines) of recorded available data (symbols) of Y vs x^* to the seepage velocity u^* using ODE (30) at 08:03 on March 20. Dotted lines mark $Y \pm 7\% Y$, from which we estimate uncertainties in u^* . The integration of ODE (30) without seepage, shown as a dashed line, fails to capture data. Blue, yellow and red vectors are proportional to dimensionless fluxes of, respectively, advection $u_s^* Y_s p^* / T_s^*$, diffusion $\Psi_s^* / (1 - \nu)$ from Eq. (32), and their sum at the dune surface. Later in the movie (not shown here), the signal splits at 13:25 on March 20 in two bistable envelopes analyzed in section 12. During the subsequent period of high winds, dryer conditions prevail with aeolian transport (pink) than without (blue). Right: measured unsteady terms \mathbb{U}_M (blue line), \mathbb{U}_T (red line) and $\mathbb{U}_M + \mathbb{U}_T$ (black dashed line) defined in Eq. (29).

569 showed that a ripple with ondulations (counted positive *downward* like x)

$$570 \quad h = h_0 \cos(\omega_{X_0} \mathcal{X}) \quad (33)$$

571 along the wind direction of unit vector $\hat{\mathbf{X}}$ produces a pore pressure field in the subsur-
572 face half-space that is a solution of the Laplace equation governing quasi-steady Darcy
573 flow,

$$574 \quad p = p_a + \rho v_\tau^2 \times \delta p^* \exp(-\omega_{X_0} x), \quad (34)$$

575 where $\omega_{X_0} = 2\pi/\lambda_0$ is the single-mode wavenumber of the harmonic ripple along \mathcal{X} ,
576 v_τ is the turbulent shear velocity, and

$$577 \quad \delta p^* = 2\pi(h_0/\lambda_0) \sqrt{\mathcal{C}^2 + \mathcal{D}^2} \cos[(\omega_{X_0} \mathcal{X}) - \phi_0] \quad (35)$$

578 is the dimensionless excursion from the ambient pressure p_a at the surface, with phase
579 lag $\phi_0 = \arctan(\mathcal{D}/\mathcal{C}) > 0$. Fourrière (2009) and Fourrière et al. (2010) calculated the
580 coefficients \mathcal{C} and \mathcal{D} in terms of the parameter $\ln(2\pi z_0/\lambda_0)$, where z_0 is the hydrodynamic
581 roughness (Claudin et al., 2016). Through Darcy's Eq. (17), the gradient of the pressure
582 field in Eq. (34) then induces the seepage velocity at $x = 0$,

$$583 \quad u_s = U^2 \left[\frac{K\rho(v_\tau/U)^2}{\mu(1-\nu)} \right] \omega_{X_0} \delta p^* \equiv U^2 \tau_K \omega_{X_0} \delta p^*, \quad (36)$$

584 which, like surface pressure, features a peak lagging behind the harmonic ripple profile
585 by a distance $\lambda_0 \phi_0 / (2\pi)$ along the wind. In Eq. (36), $\tau_K \equiv K\rho(v_\tau/U)^2 / [\mu(1-\nu)]$ has
586 units of time and incorporates the ratio v_τ/U , which typically varies on the sand sur-
587 face.

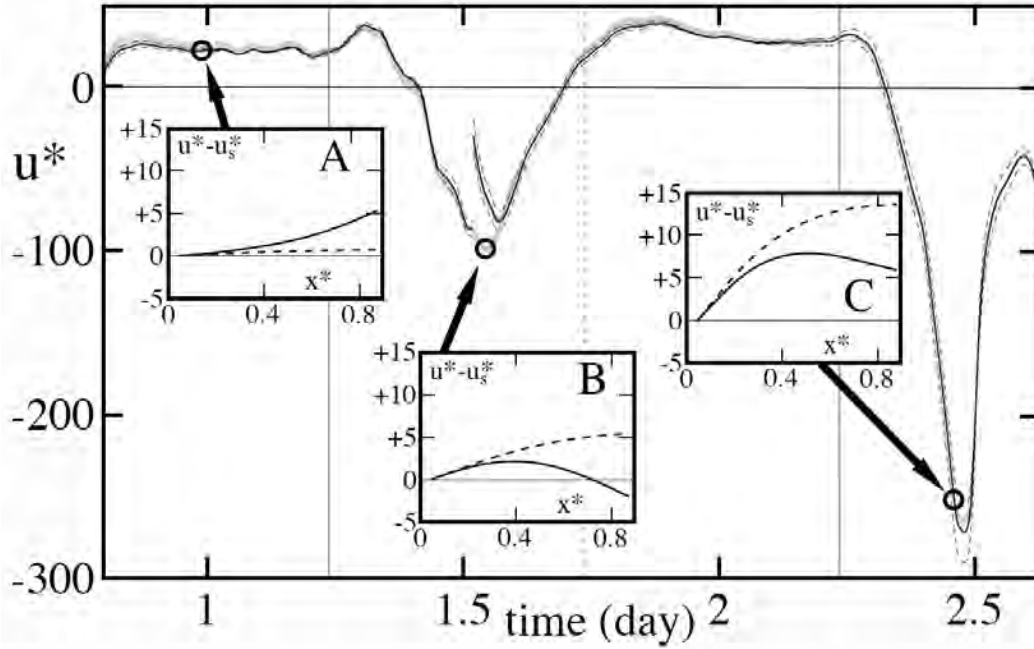


Figure 7. Time-history of dimensionless seepage velocity u^* at the dune surface vs t^* (solid line) with surrounding uncertainties (dashed lines) associated with the measured $Y \pm 7\% Y$ shown in Fig. 6. The grey regions enclose values of u^* calculated in Appendix F for depths $x^* < 0.87$ above sensor 10. Splitting of the u^* -record in the period $1.4 < t^* < 1.63$ arises as signal envelopes separate during aeolian transport. Solid lines in insets A, B and C are typical profiles of $u^* - u_s^*$ calculated through these depths at times $t^* = 0.98, 1.54$ and 2.47 ; dashed lines illustrate the role of vapor release on u^* by artificially making $f_T = f_Y = 0$ in these calculations. Insets and grey regions reveal that u^* varies little with depth in this case.

For our dune, we estimate $\lambda_0 \simeq 220$ m as approximately four times its toe to crest distance, and $h_0 \simeq 4.5$ m as its crest height (Fig. 8). Anemometry carried out near the capacitance probe location in January 2017 also found $z_0 \simeq 16 \mu\text{m}$. With $\ln(2\pi z_0/\lambda_0) \simeq -14.6$, Fourrière (2009) calculated $\mathcal{C} \simeq -1150$ and $\mathcal{D} \simeq 49$. Because \mathcal{C} and \mathcal{D} has a weak logarithmic dependence on z_0 and modal wavelengths, we ignore variations of these quantities on the dune and, for simplicity, treat \mathcal{C} and \mathcal{D} as constants.

Because the single-mode wavenumber $\omega_{X_0} = 2\pi/\lambda_0$ is very small, Eq. (36) would predict a much smaller seepage than a ripple of comparable aspect ratio, if the dune possessed a harmonic profile. However, the dune shape is not harmonic, but instead features gentle undulations in its surface elevation $z(\mathcal{X}, \mathcal{Y})$ along the wind unit direction $\hat{\mathbf{X}}$ and its cross-wind counterpart $\hat{\mathbf{Y}}$. The small ratio of dune height on wavelength $h_0/\lambda_0 \sim 0.02$ further suggests that $z(\mathcal{X}, \mathcal{Y})$ may be expanded in Fourier modes that contribute linearly to the overall pressure excursion (Musa et al., 2014). Then, as the following analysis shows, some of these modes may possess large enough wavenumbers to induce significant seepage.

Inspired by the theory of P. S. Jackson and Hunt (1975) and Hunt et al. (1988), Kroy et al. (2002) derived the transfer function relating the two-dimensional Fourier transforms of dune elevation \tilde{z} and perturbation in turbulent shear stress $\tilde{\delta\tau}$ in terms of two parameters \mathcal{A} and \mathcal{B} . The dimensionless pressure excursion δp^* is subject to a similar transfer function, in which \mathcal{A} and \mathcal{B} are respectively replaced by \mathcal{C} and \mathcal{D} ,

$$\frac{\tilde{\delta p}^*}{\tilde{z}} = \frac{\omega_X (\mathcal{C}\omega_X + i\mathcal{D}|\omega_X|)}{\sqrt{\omega_X^2 + \omega_Y^2}}, \quad (37)$$

where $\omega_X \equiv 2\pi/\lambda_X$ and $\omega_Y \equiv 2\pi/\lambda_Y$ are wavenumbers along $\hat{\mathbf{X}}$ and $\hat{\mathbf{Y}}$, respectively. With Eq. (37), the two-dimensional Fourier transform of z obtained from a dune survey therefore yields $\tilde{\delta p}^*$, which is then inverted to recover the pressure excursion everywhere on the dune surface. To evaluate \tilde{z} at each time step, we tilt the dune slightly so it rises above an artificially flattened desert floor, rotate it around the origin of $(\mathcal{X}, \mathcal{Y})$ at the barycenter of its outline to align $\hat{\mathbf{X}}$ with the instantaneous wind direction, interpolate survey points using the *C1*-continuous `scatteredInterpolant` of MATLAB, subdivide the square central domain circumscribing the rotated dune outline in 2^N cells with $N = 9$, and buttress this domain with eight identical squares holding zero elevation to avoid aliasing. The resulting physical domain of width $\Delta\mathcal{X}$ therefore holds 2^{N+2} cells along both directions, leading to 2^{N+2} discrete wavenumbers $\omega_X = (2\pi/\Delta\mathcal{X}) \times (0, \dots, 2^{N+1}, -2^{N+1} + 1, \dots, -1)$, organized in the peculiar order with which MATLAB optimizes its discrete Fourier transforms (DFT). Comparing predictions of Eq. (37) from the two-dimensional `fft2` DFT and its one-dimensional counterpart `fft` with $\omega_Y = 0$, we find that transverse wavenumbers ω_Y play a minor role. Therefore, for simplicity, we reconstruct the pressure excursion δp^* on any wind-directed transect using the first $1+2^{N+1}$ coefficients of the one-dimensional DFT $\tilde{\delta p}^*$ in Eq. (37) with $\omega_Y = 0$,

$$\delta p^* = a_0 + \sum_{i=1}^{2^{N+1}} \delta p_i^* = a_0 + \sum_{i=1}^{2^{N+1}} a_i \cos(2\pi\mathcal{X}/\lambda_i) + b_i \sin(2\pi\mathcal{X}/\lambda_i), \quad (38)$$

where $a_0 = \tilde{\delta p}_0/2$ corresponds to $\omega_X = 0$, while $a_i = \Re(\tilde{\delta p}_i^*)/2^{N+1}$ and $b_i = -\Im(\tilde{\delta p}_i^*)/2^{N+1}$ are for $\omega_X = \omega_{X_i} = (2\pi/\lambda_i) = (2\pi i/\Delta\mathcal{X})$ with $i = 1, \dots, 2^{N+1}$, and \Re and \Im denote real and imaginary parts. To evaluate the surface seepage velocity, we then superimpose modal contributions as

$$u_s = U^2 \tau_K \sum_{i=1}^n \omega_{X_i} \delta p_i^*. \quad (39)$$

To avoid spurious noise associated with survey errors at small wavelengths, we truncate the series at $n < 2^{N+1}$, such that remaining modes account for 97% of the total power $\sum a_i^2 + b_i^2$ of the DFT.

636 Because we did not conduct a detailed survey of the dune in March 2011, we de-
 637 rive z from theodolite measurements carried out on the same dune in January 2017, and
 638 thus our calculations are only suggestive. However, they explain the seepage variations
 639 shown in Fig. 7. As inset (D) of Fig. 8 illustrates, variations of dune elevation along the
 640 wind direction, once converted to excursions in surface pressure, have their greatest Fourier
 641 power content at wavelengths on the order of the dune size ~ 100 m. Unlike sand rip-
 642 ples (Louge, Valance, Babah, et al., 2010), such wavelengths are too large to contribute
 643 appreciably to seepage. However, much power remains at smaller wavelengths ~ 10 to
 644 30 m, particularly when wind flows toward the mean 159° historical bearing of this mo-
 645 bile dune. Because the gradient in Darcy’s Eq. (17) effectively amplifies surface pressure
 646 variations, these modes produce a seepage advection with significant longitudinal oscil-
 647 lations. As colored zones in Fig. 8E suggest, parts of the dune inhale (red, $u_s > 0$), while
 648 others simultaneously exhale (blue, $u_s < 0$). These patterns change as wind changes
 649 direction, and as aeolian transport alters the dune’s surface morphology.

650 The resulting predictions of u_s/τ_K in Fig. 8 are consistent with magnitudes of u_s
 651 calculated in section 8. At the capacitance probe location (grey circle), inset A has a min-
 652 imum of $u_s/\tau_K \simeq -3300$ m/s² on the first day, while Fig. 7 has $u^* \simeq u_s^* \simeq -100$.
 653 This corresponds to $\tau_K \simeq 6 \cdot 10^{-8}$ s, which agrees well with $\tau_K \simeq 5 \cdot 10^{-8}$ s derived from
 654 parameters adopted in this article: $d \simeq 351 \mu\text{m}$, $\nu \simeq 0.545$, $K \simeq 2.6 \cdot 10^{-10}$ m² (Eq. 18),
 655 $\rho \simeq 1.19$ kg/m³, $\mu \simeq 1.8 \cdot 10^{-5}$ kg/m.s and $v_\tau/U \simeq 0.036$.

656 However, a surprising observation from Fig. 7 is the larger seepage advection ve-
 657 locity magnitude on March 21 ($t^* \sim 2.5$) than March 20 ($t^* \sim 1.5$) despite a smaller
 658 wind speed on the second day ($U \sim 5$ m/s) than the first ($U \sim 7.5$ m/s). A possible
 659 reason for this paradox may be a change in surface morphology from one day to the next,
 660 which affects \tilde{z} and therefore shifts seepage patterns. Another could be associated with
 661 sand loading during aeolian transport on March 21. Here, the energy required to lift sand
 662 grains on the first day may have lowered static pressure on the surface, thereby reduc-
 663 ing the gradient between ambient and porous sand beneath it.

664 Finally, this calculation revealed that seepage advection varies greatly with loca-
 665 tion. Therefore, it is difficult to predict it for an arbitrary point using Eq. (39), unless
 666 topography is known precisely for the entire dune at every instant, along with wind strength
 667 and direction. Fortunately, we showed in section 8 that seepage can be inferred locally
 668 from measured spatio-temporal variations of vapor mass fraction.

669 10 Diurnal predictions

670 In this section, we use MATLAB’s `pdepe` to integrate PDE (26) with the seepage
 671 velocity inferred in section 8 and predict the observed spatio-temporal evolution of va-
 672 por mass fraction Y on relatively long diurnal time scales. Deferring a discussion of rapid
 673 variations until section 12, we view the record of Y during the onset of aeolian transport
 674 as two coinciding envelopes of a bistable signal. Integration is achieved in two overlap-
 675 ping periods. The first one begins at 19:12 Qatar time ($t^* \simeq 0.80$) on March 19 and
 676 ends at 15:02 ($t^* \simeq 1.63$) on March 20 when aeolian transport stops. Here, the PDE
 677 is subject to a surface boundary condition Y_1 equal to the low continuous signal enve-
 678 lope at sensor 1 closest to the surface (Fig. 3). The second period starts at the onset of
 679 aeolian transport on March 20 (12:29 or $t^* \simeq 1.52$) and it persists until data acqui-
 680 sition is over on March 21 at 15:02 ($t^* \simeq 2.63$). Its surface boundary condition is the high
 681 envelope at sensor 1.

682 Unlike the procedure outlined in section 8 to determine seepage velocity (Fig. 6),
 683 we integrate the PDE over the entire probe depth, even if the probe does not return data
 684 at the deepest sensors. When it does, we note that the resulting values of Y align on the
 685 thin dotted line marking the adsorbed mass fraction $\Omega \simeq 1.65 \Omega_1$. This suggests that

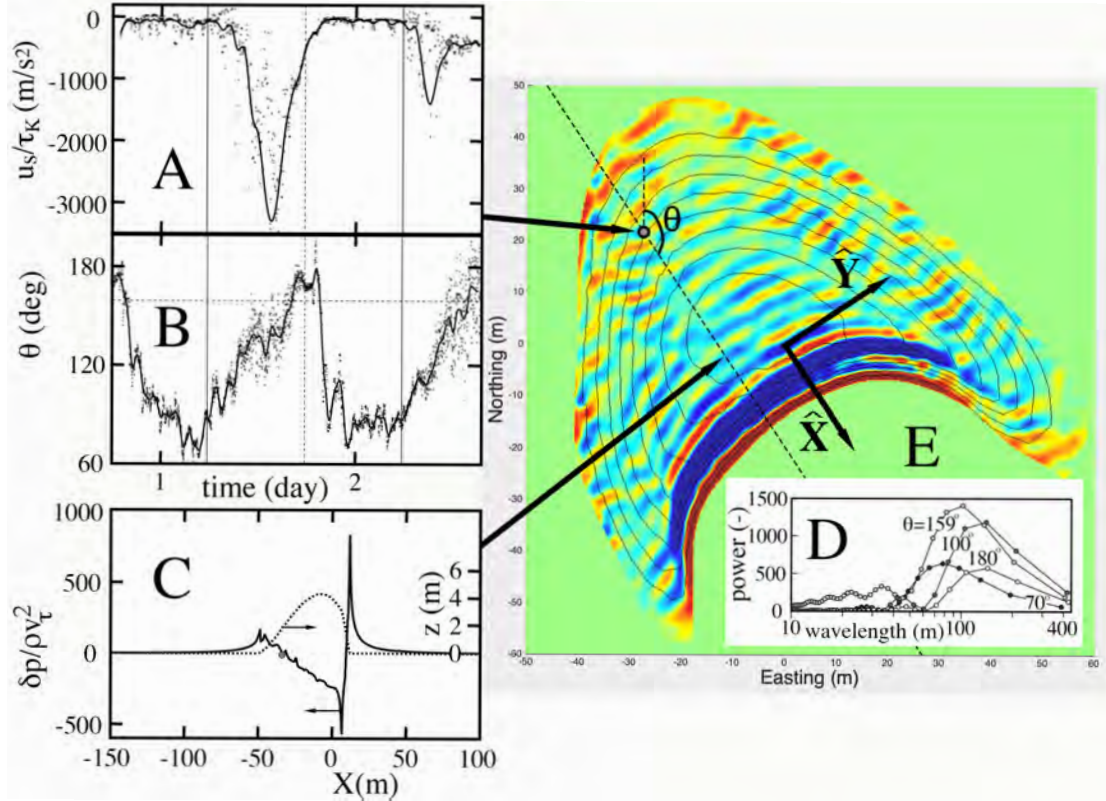


Figure 8. Seepage predictions of Eq. (39) calculated for the dune shape in January 2017, the wind record U in Fig. 3, and the instantaneous wind direction $\hat{\mathbf{X}}$. (A) Relative surface seepage velocity u_s/τ_K (m/s² > 0 into sand) at the position shown by the grey dot in inset (E) vs diurnal time t/J . (B) Instantaneous wind bearing θ (deg) vs t/J , and mean historical bearing from Louge et al. (2013) (horizontal line). In insets (A) and (B), the line is a visual fit, and vertical solid and dashed lines mark sunrise and sunset, respectively. (C) Solid line: predicted relative pressure excursion δp^* vs distance \mathcal{X} (m) along the transect marked by the dashed line in inset (E); dashed line: dune elevation z (m) along this transect. (D) Dimensionless spectral power $a_i^2 + b_i^2$ of pressure excursions in Eq. (38) vs wavelength $\lambda_i = \Delta\mathcal{X}/i$ with $i = 1, \dots, 2^{N+1}$ for the wind bearings shown. (E) Snapshot of u_s/τ_K on the dune surface at 11:14 on March 21, marked by grey dots in A and B. The whole movie **MovieDuneSurfaceSeepagePrediction.mp4** is available as supporting information. Black isolines are placed every 0.5 m. For best contrast, colors are obtained by converting $[1 + \tanh(u_s/(\tau_K\gamma_0))]/2$ to the **jet** color map of MATLAB with $\gamma_0 = 10^3$ m/s².

686 a suitable bottom boundary condition is an invariant Ω at depth, $\partial\Omega/\partial x^*|_{\text{depth}} = 0$.
 687 In this case, using equations derived in Appendix C, such boundary condition (BC) may
 688 be written

$$689 \quad \left. \frac{\partial Y}{\partial x^*} \right|_{\text{depth}} = Y [1 + Y(M^* - 1)] \left. \frac{\partial T^*}{\partial x^*} \right|_{\text{depth}} \left[\frac{1}{T^*} \ln \left(\frac{1}{\text{RH}} \right) + \frac{T_{A_a} T_{\text{st}}}{(T - T_{A_0})^2} \right]. \quad (40)$$

690 We impose it as the bottom of our integration domain, set for simplicity at the deepest
 691 sensor. To show predicted variations with depth and time, and to compare measurements
 692 and predictions, we produced a movie available in the supporting information, with typ-
 693 ical frames in Fig. 4. This analysis also underscores the coupling of spatio-temporal vari-
 694 ations of T and Y . Making $f_T \equiv 0$ to eliminate it from PDE (26) would suppress the
 695 multiple observed inflections in the depth profile of Y , and altogether fail to capture data.

696 Finally, deeply buried water from antecedent rains, reported in Table 1 of Louge
 697 et al. (2013), matters to spatio-temporal variations of adsorbed moisture on sand grains
 698 nearer the surface. Its effects are captured by BC (40) at the bottom of our near-surface
 699 domain without liquid water. This BC can also be used to match our model of the near-
 700 subsurface to solutions for the deeper, moister domain below, for example those of Kamai
 701 and Assouline (2018); Assouline and Kamai (2019); Shao et al. (2021), or our own in-
 702 tegration of Richards' equation (Richards, 1931; Louge et al., 2013).

703 However, because unsaturated porous media are governed by a history-dependent
 704 and hysteretic relation between capillary pressure and liquid volume fraction (Xu & Louge,
 705 2015), definitive models of deeper liquid-infused regions are more challenging than our
 706 own. Conversely, their measurement techniques of water content are well established (Kizito
 707 et al., 2008; Kidron & Kronenfeld, 2020).

708 In short, until now, spatio-temporal variations of adsorbed water had not been mea-
 709 sured in the liquid-free near-surface region of hyper-arid dunes with enough accuracy or
 710 spatial resolution. Doing so allowed us to show that this region could be analyzed with-
 711 out arbitrary closures. The principal remaining challenge is to model the deeper unsat-
 712 urated region holding free liquid, where capillary effects continue to defy rigorous pre-
 713 dictions.

714 11 Evaporation at the grain scale

715 The capacitance probe detects phenomena that other instruments with thicker mea-
 716 surement volume, such as microlysimeters (Boast & Robertson, 1982) or frequency-domain
 717 reflectometry sensors (Kizito et al., 2008), cannot discern. In particular, during periods
 718 of aeolian sand transport, the capacitance probe returned values of Y belonging to two
 719 distinct envelopes switching rapidly from one to the other.

720 Figure 9 shows that the difference ΔY between these envelopes decreases exponen-
 721 tially with depth, that the lowest envelope coincides with the ambient vapor mass frac-
 722 tion Y_a , and that the probe hardly ever discerned any value of Y in between the envelopes.
 723 These observations suggest that strands of saltating particles meandering over the dune
 724 dried the surface intermittently, thereby sending rapid waves of Y downward on time scales
 725 too small for water vapor to come to equilibrium with the thin film of water adsorbed
 726 on sand grains.

727 To support this explanation, we briefly summarize the underlying physics of evap-
 728 oration at the grain scale, and we show that the characteristic time τ for the film's re-
 729 turn to an equilibrium is governed by slow first-order reaction kinetics, rather than by
 730 diffusion to the surface of individual grains. Then, we conduct a linear stability analy-
 731 sis of Eq. (21) in the limit of short time scales. The calculations are consistent with the
 732 observed exponential decrease of the wave amplitude with depth. The corresponding length
 733 scale then lets us estimate τ , thus providing insight into the drying process for these sands.

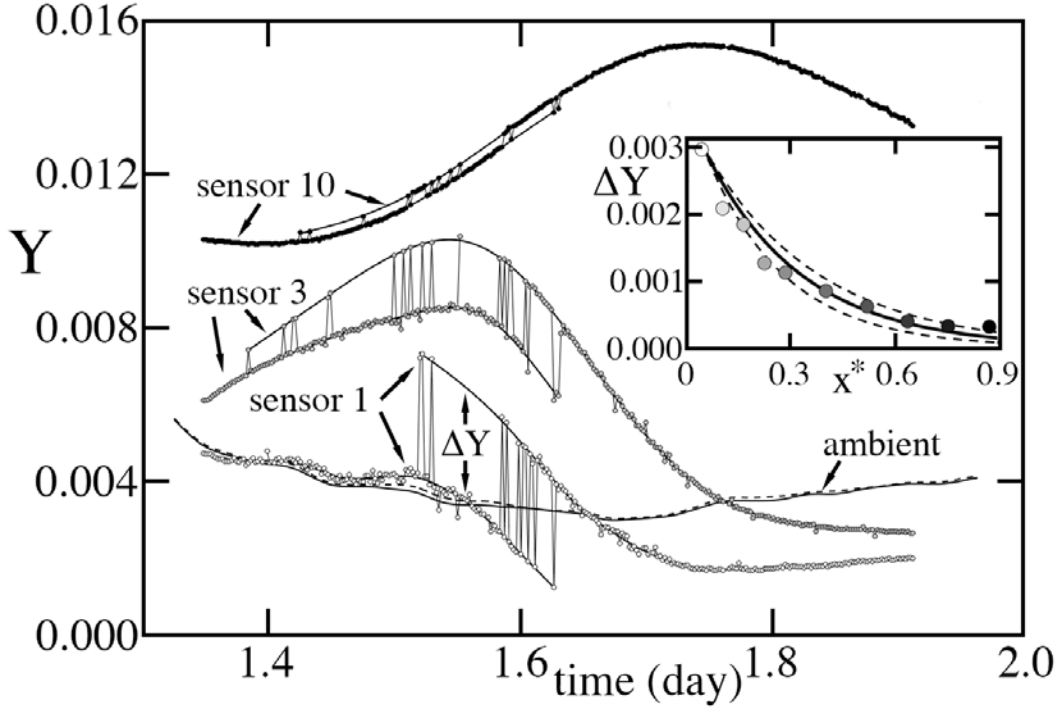


Figure 9. Detail of Fig. 3 showing two envelopes of the vapor mass fraction Y during a period of aeolian transport. Circles are data of sensors shown vs dimensionless time t^* . Thin lines indicate when the signal jumps from one envelope to the other. For each sensor, the lower Y correspond to aeolian sand drying the surface. The superimposed lines are smoothing spline fits used to evaluate $\partial Y/\partial t^*$ in the analysis. The solid and dashed lines marked “ambient” are Y_a measured at the top and bottom hygrometers of the weather station, respectively. Inset: the resulting mean difference $\Delta Y = (t_1^* - t_0^*)^{-1} \int_{t_0^*}^{t_1^*} (Y_u - Y_l) dt^*$ between the upper Y_u and lower Y_l envelopes of Y vs dimensionless depth x^* (circles) with $t_0^* \simeq 1.52$ and $t_1^* \simeq 1.63$. The line is the model of Eq. (51) with $\ell^* = 0.28 \pm 0.05$.

734 During our two consecutive days of field data collection, the top ten sensors of our
 735 capacitance probe detected no free liquid water within the first 15 cm below the surface.
 736 In this case, the exchange of moisture conformed to the “hygroscopic” regime, in which
 737 capillary forces are insignificant, and water molecules either form a thin layer on the sur-
 738 face of grains, or exist as a vapor in air.

739 The amount of moisture bound to grains in the size class of diameter d is measured
 740 by the mass fraction Ω_d of water that the class holds. In the vapor phase within the in-
 741 terstitial space between packed grains, the mass fraction of water is Y . Given enough
 742 time, Ω_d and Y reach an equilibrium, denoted by the subscript e , in which the rate of
 743 evaporation from grains is balanced by condensation at a given temperature. Appendix
 744 B provides the form of the corresponding “isotherm” of size class d . Once integrated over
 745 the particle-size distribution, Eq. B1 yields the isotherm for the average mass fraction
 746 Ω_e that Louge et al. (2013) recorded in terms of the relative humidity RH_e in a humid-
 747 ity chamber.

748 In general, Ω is a macroscopic measure of the thin coating of water arranged as molec-
 749 ular layers on grain surfaces. As Eqs. (1)-(2) indicate (Shahraeeni & Or, 2010), his coat-
 750 ing has mean thickness

$$751 \quad \ell_w \simeq \left(\frac{d_{2,3}}{6}\right) \left(\frac{\rho_p}{\rho_w}\right) \frac{\Omega_1}{T^{*1/3} \ln^{1/3} [p_{\text{sat}} / (pM^*Y_e)]}, \quad (41)$$

752 where $\rho_p \simeq 2630 \text{ kg/m}^3$ and $\rho_w \simeq 997 \text{ kg/m}^3$ are, respectively, sand and water ma-
 753 terial densities, $d_{2,3} \simeq 300 \mu\text{m}$ is the Sauter mean diameter that arises from the inte-
 754 gration over the particle size distribution, and $\Omega_1 \simeq 0.0013$ (Louge et al., 2013). In this
 755 field campaign, the probe recorded $0.0011 < Y_e < 0.017$, or $120 \text{ nm} < \ell_w < 330 \text{ nm}$,
 756 corresponding to 400 to 1100 layers of water molecules of individual 0.3 nm thickness (Yeşilbaş
 757 & Boily, 2016).

758 With so many layers, it is reasonable to neglect interactions with the solid as wa-
 759 ter molecules escape from grains or adsorb on them. In this case, grain evaporation can
 760 be regarded as a non-equilibrium process releasing water molecules at the interface be-
 761 tween interstitial air and the thin water coating, mitigated by a reverse reaction of va-
 762 por condensation (Koffman et al., 1984). Even under controlled laboratory conditions,
 763 the coupling of vapor and liquid phases, or possibly local variations of temperature near
 764 the gas-liquid interface (Jafari et al., 2018), make it challenging to model this process (Persad
 765 & Ward, 2016). Because we must also contend with grains of varying size, shape, sur-
 766 face geometry, impurities and composition, immersed in a random interstitial space, we
 767 resort to a rudimentary model that is inspired from the Hertz-Knudsen-Schrage (HKS)
 768 theory (Marek & Straub, 2001). In this view, the net vapor mass flux at the saturated
 769 gas-liquid interface,

$$770 \quad \dot{W}_{\text{HKS}}'' = \frac{2\kappa_e}{2 - \kappa_c} \sqrt{\frac{\text{MW}_{\text{H}_2\text{O}}}{2\pi\hat{R}}} \left[\left(\frac{\kappa_c}{\kappa_e}\right) \frac{p_{\text{sat}}}{T_\ell^{1/2}} - \frac{p_{\text{H}_2\text{O}}}{T_v^{1/2}} \right], \quad (42)$$

771 is built upon the prediction of the kinetic theory of gases for the water mass flux
 772 $p_{\text{H}_2\text{O}} \sqrt{\text{MW}_{\text{H}_2\text{O}} / (2\pi\hat{R}T)}$ crossing a control surface under a Maxwellian velocity distri-
 773 bution function (Vincenti & Kruger, 1965). In this expression, $p_{\text{H}_2\text{O}} \simeq pYM^*$ is the
 774 partial pressure of water vapor in the interstitial space, $\hat{R} \simeq 8.314 \text{ J/mole.K}$ is the fun-
 775 damental gas constant, and the “accommodation coefficients” of evaporation κ_e and con-
 776 densation κ_c represent the probability that a water molecule colliding with the interface
 777 undergoes its respective first-order phase transition (Y. Q. Li et al., 2001).

778 For the tight porous medium of the dune with grains of relatively high heat capaci-
 779 ty, it is reasonable to assume that the temperature T_ℓ at the gas-liquid interface and its
 780 interstitial vapor counterpart T_v are equal to the local value T of the “heat bath” that

our instrument measured. Then, because the vapor is saturated at the interface, $\text{RH} \equiv 1$, an expression similar to Eq. (7) sets the mass fraction there, $Y_{\text{sat}} \simeq p_{\text{sat}}/(pM^*)$.

Meanwhile, at equilibrium, evaporation and condensation balance ($\dot{W}_{\text{HKS}}'' = 0$), and molecular diffusion makes the interstitial vapor fraction Y uniform and equal to the value Y_e recorded by the isotherm of Eq. (B1) for each size class. Therefore, the expression $(\kappa_c/\kappa_e)Y_{\text{sat}}$ is identified with Y_e , and Eq. (42) becomes

$$\dot{W}_{\text{HKS}}'' \simeq \frac{2\kappa_e}{2 - \kappa_c} \sqrt{\frac{MW_{\text{H}_2\text{O}}}{2\pi\hat{R}T}} pM^* (Y_e - Y) \equiv k_m (Y_e - Y), \quad (43)$$

which serves as definition of the rate constant k_m of a balanced first-order reaction of evaporation returning the system to equilibrium.

Because the interstitial space may also possess local gradients of Y , vapor diffusion on the pore scale could also play a role in setting the flux at the film’s interface. For example, Philip (1964) and Shahraeni and Or (2010) assumed that the transport of vapor to grain asperities is dominated by diffusion. (Section 12 will show that such assumption is not consistent with the depth scale of subsurface waves that we observed).

In general, as in the combustion of a solid particle (Kanury, 1975), there are two limiting regimes. In the “kinetic limit”, k_m is small relative to $\rho D/d$, so diffusion of coefficient D erases gradients of Y in a pore with interstitial air of local density ρ . Conversely, in the “diffusion limit”, the evaporation rate of Eq. (43) is much more intense than the local diffusive flux.

As Appendix G shows, the dominant process setting the net vapor flux \dot{W}_s'' at the grain surface is the slowest of the two. Once it is identified, one can infer the rate of change of the mass fraction Ω_d for each size class. Assuming for simplicity that grains of material density ρ_p are spherical,

$$\rho_p \nu \frac{\partial \Omega_d}{\partial t} = -\frac{6\nu \dot{W}_s''}{d} \equiv \frac{\rho(1 - \nu)}{\tau_d} (Y - Y_e), \quad (44)$$

which defines the characteristic reaction time τ_d for the size class of diameter d . Upon integration over the particle size distribution in Appendix B, Eq. (44) yields the ODE that governs the rate of change of the overall moisture mass fraction Ω adsorbed on bulk sand of solid volume fraction ν ,

$$\frac{\partial \Omega}{\partial t} = \frac{\rho(1 - \nu)}{\rho_p \nu} \left(\frac{Y - Y_e}{\tau} \right). \quad (45)$$

In the next section, we conduct a stability analysis to determine the origin of the subsurface waves of Y revealed by our instrument, and to calculate the characteristic depth of their decay. In turn, this depth sets bounds for possible values of τ and, as Appendix G shows, conclusively places evaporation at the grain scale in the kinetic limit.

12 Evanescent waves

In section 7, we considered the limit when variables change slowly enough that the water film of mass fraction Ω remains in equilibrium with the interstitial Y . When instead Y varies on a time scale shorter than τ , Ω does not change appreciably, so the right side of Eq. (21) becomes small. This situation arises during aeolian transport (Dupont et al., 2013), when clustered strands of dry particles meander over the dune, alternately forcing the surface Y to adopt the ambient value Y_a , or letting it quickly readjust to its higher original level without them. As Fig. 9 shows, recorded mass fractions then switch between these two extreme states, and the resulting difference ΔY decreases exponen-

823 tially with depth. Toward explaining this, we write Eq. (21) in a dimensionless form de-
 824 noted by asterisks,

$$825 \frac{p^*}{T^*} \frac{\partial Y}{\partial t^*} + \frac{p^*}{T^*} u^* \frac{\partial Y}{\partial x^*} - \mathbb{L} \frac{\partial}{\partial x^*} \left[T^{*n_d} \left(\frac{\partial Y}{\partial x^*} + a_T Y \frac{\partial \ln T^*}{\partial x^*} \right) \right] = -\frac{p^*}{T^*} \frac{(Y - Y_e)}{\tau^*} (1 - Y), \quad (46)$$

826 where $\tau^* \equiv \tau/J$. Here, the diffusion term involves a Soret effect with coefficient a_T cou-
 827 pling variations of T and Y , which Appendix E dismisses as unimportant.

828 In this equation, Y_e is known in terms of the instantaneous Ω held by grains from
 829 Eqs. (3) and (7). On short time scales, it is therefore invariant as equilibrium cannot be
 830 restored fast enough. In this analysis, we consider waves of Y traveling about its mean
 831 value \bar{Y} at the dimensionless frequency $f^* \equiv fJ$,

$$832 Y = \bar{Y} + \delta Y \exp[i(2\pi f^* t^* - k^* x^*)], \quad (47)$$

833 where $i^2 = -1$. Substituting this expression in Eq (46), expanding to leading order in
 834 $\delta Y/\bar{Y} \ll 1$, simplifying $(1 - Y) \simeq 1$, subtracting the time-averaged equation, applying
 835 derivatives of Eq. (47), and dividing by the exponential term and δY , Eq. (46) yields the
 836 characteristic equation

$$837 A_c k^{*2} - i B_c k^* + C_c = 0, \quad (48)$$

838 where

$$839 A_c \equiv \mathbb{L} T^{*n_d} \quad (49)$$

$$840 B_c \equiv \frac{p^*}{T^*} u^* - \mathbb{L} (n_d + a_T) T^{*n_d} \frac{\partial \ln T^*}{\partial x^*}$$

$$841 C_c \equiv -a_T \mathbb{L} T^{*n_d} \left[(n_d - 1) \left(\frac{\partial \ln T^*}{\partial x^*} \right)^2 + \frac{\partial \ln T^*}{\partial t^*} \right] + \frac{p^*}{T^*} [i 2\pi f^* + 1/\tau^*],$$

842 and T^* and u^* are sampled in the midst of the aeolian transport period at $t^* \simeq 1.57$.
 843 There are two solutions $k^{*\pm} = k_r^{*\pm} - i k_i^{*\pm}$ to quadratic Eq. (48), with real and imag-
 844 inary parts $k_r^{*\pm}$ and $k_i^{*\pm}$,

$$845 k^{*\pm} = i \frac{B_c}{2A_c} \pm \frac{1}{2A_c} \sqrt{-B_c^2 - 4A_c C_c}. \quad (50)$$

846 The two resulting traveling waves in Y have the form $\delta Y \exp(k_i^{*\pm} x^*) \times \exp[i(2\pi f^* t^* -$
 847 $k_r^{*\pm} x^*)]$. Of these, only the k^{*+} wave has $k_i^{*+} < 0$, and therefore vanishes as $x^* \rightarrow \infty$.
 848 In the regime of rapid oscillations and slow return to equilibrium (Fig. 9), we match its
 849 decreasing amplitude along x^*

$$850 \Delta Y = \delta Y \exp(-|k_i^{*+}| x^*) \quad (51)$$

851 to the exponential decay with characteristic length $\ell^* \equiv -1/k_i^{*+} = 0.28 \pm 0.05$, or $\ell =$
 852 4.9 ± 0.9 cm. This relatively short ℓ justifies why it is crucial to measure water mass frac-
 853 tion with a probe of narrow vertical spatial resolution.

854 Meanwhile, Eqs. (49)-(50) yield k_i^{*+} in terms of the known parameters \mathbb{L} , n_d , and
 855 a_T , the measured variables T^* , u^* and p^* , as well as τ^* and f^* . Therefore, they can be
 856 recast as the relation between τ^* and f^* that yields the measured ℓ^* . For our conditions,
 857 this relation is conveniently fitted as $\tau^* \simeq \tau_1^* + \delta\tau^*/[(1/f^* - (1/f_1^*))]$, where $(1/f_1^*) \simeq$
 858 0.0084 (12 min), $\delta\tau^* \simeq 4.2 \cdot 10^{-5}$ and $\tau_1^* \simeq 0.01$ (14 min). Although we did not sample
 859 Y fast enough to establish its high frequency content, an inspection of oscillations in the
 860 bistable Y -record (thin lines in Fig. 9) suggests that $0.013 \lesssim 1/f^* \lesssim 0.033$ (19 to 48 min),
 861 thus yielding $\tau^* = 0.015 \pm 0.004$ (22 ± 5 min).

862 Such time is much larger than the diffusion time $\tau_{\text{DIFF}} \sim 240 \mu\text{s}$ estimated in Ap-
 863 pendix G. Therefore, if the diffusion limit prevailed, sand grains would have ample time

864 to return everywhere to an equilibrium with the surrounding vapor mass fraction. In that
 865 case, as section 7 showed, the right side of Eq. (46) would become $-\mathbb{R}\Omega_1 f_Y \partial Y / \partial t^*$, where
 866 temperature changes negligibly, $f_Y \propto 1/Y$, and $\mathbb{R} \equiv \rho_p \nu / [\rho_{st}(1 - \nu)]$. Then, the pro-
 867 cedure leading to characteristic Eq. (48) would leave A_c and B_c unchanged, while replac-
 868 ing C_c in Eq. (49) with

$$869 \quad C'_c = \frac{p^*}{T^*} i 2\pi f^* + \mathbb{R}\Omega_1 \bar{f}_Y \left(i 2\pi f^* - \frac{\partial \ln \bar{Y}}{\partial t^*} \right), \quad (52)$$

870 an expression that no longer involves τ . Using recorded T^* , u^* , \bar{f}_Y , and $\partial \ln \bar{Y} / \partial t^*$ at
 871 $t^* \simeq 1.6$, we find that ℓ^* would never exceed 0.045, which is much smaller than the ob-
 872 served ℓ^* . Therefore, we conclude that evaporation is a kinetic-limited process in our case.

873 A common alternative approach to the kinetics of evaporation assumes that wa-
 874 ter in the adsorbed film is at thermodynamic equilibrium with the surrounding RH, while
 875 time-history is reintroduced through mass conservation and diffusion (Eq. 21). Such equi-
 876 librium approach to the evaporation rate, which is suitable for the drying of porous me-
 877 dia such as wood or biomass, see for example Nasrallah and Perré (1988); Zhang and Datta
 878 (2004); Borujerdi et al. (2019), would fail for these hyper-arid sands.

879 Lastly, our determination of $\tau^* \simeq \tau_{\text{HKS}}^* = 0.015 \pm 0.004$ yields the accommoda-
 880 tion coefficient of evaporation. Substituting the mean Sauter diameter $d_{2,3}$ for d in Eq. (G1),
 881 and taking κ_c to be on the same order, we find $\kappa_e = (2.3 \pm 0.5) 10^{-10}$. Such value is
 882 very small by the standards of pure, smooth surfaces. However, microscopic impurities,
 883 which are certain to contaminate desert sands, and interface coverage (Rubel & Gentry,
 884 1984) are known to thwart interfacial mass transfer and reduce κ_e by several orders of
 885 magnitude (Marek & Straub, 2001).

886 Coincidentally, this low probability is also consistent with an activation energy $\hat{E} =$
 887 $-\hat{R}T \ln \kappa_e = 54.6 \pm 0.6$ kJ/mole, another common interpretation of the evaporation
 888 process (Rubel & Gentry, 1984; Y. Q. Li et al., 2001; Smith et al., 2006; Cappa et al.,
 889 2007; Tsukahara et al., 2009). This value is typical of the energy needed to release solid-
 890 bound water in solid fuels (Borujerdi et al., 2019) or powders (Prado & Vyazovkin, 2011)
 891 and, as expected, it is above, – but on the order of –, the latent heat $\simeq 43.9$ kJ/mole
 892 to vaporize unbound water.

893 In short, the characteristic decay depth of the evanescent waves suggests that evap-
 894 oration from these sand grains is a kinetic-limited process. Although the latter may be
 895 interpreted as having a very low accommodation coefficient, it is more intuitive to re-
 896 gard it as an activated reaction.

897 **13 Atmospheric boundary layer**

898 The instantaneous evaporation flux exchanged with the atmospheric boundary layer
 899 (ABL) from the vadose zone is a crucial boundary condition for understanding the hy-
 900 drology (Assouline & Kamai, 2019; Shao et al., 2021) and microbiology (Kidron & Starin-
 901 sky, 2019) of hyper-arid regions. Because it is important to distinguish evaporation from
 902 transpiration when vegetation is involved (R. G. Anderson et al., 2017), flux techniques
 903 deployed in the ABL, such as eddy-covariance, are supplemented by carbon dioxide mea-
 904 surements (Scanlon & Kustas, 2010), sometimes involving stable isotopes (Griffis, 2013).

905 Measurements of the evaporation flux from within the sand surface are equally chal-
 906 lenging. For example, in a fog desert, Feigenwinter et al. (2020) used an automated mi-
 907 crolysimeter (ML) that recorded the mass of non-rainfall water (NRW) deposited in a
 908 sampling cup mounted flush with the surface. However, Kidron and Kronenfeld (2020)
 909 noted how the ML technique can overestimate the NRW amount, especially at night.

910 Meanwhile, transport in the ABL faces instabilities arising from natural convec-
 911 tion during the day (Wyngaard, 2010), and it is complicated at night by stratified, weak
 912 turbulence (Mahrt, 2014; Optis et al., 2014) and by low-level jets intermittently perturb-
 913 ing the stable nocturnal boundary layer (Banta et al., 2007; Klein et al., 2016). For flat
 914 expanses of land, the resulting transports of momentum and heat are typically modeled
 915 using the Monin-Obukhov similarity (Monin, 1970). However, in the case of isolated sand
 916 dunes surrounded by a hard, more impermeable desert floor, it is unclear how such sim-
 917 ilarity can be extended to mass transfer of water vapor, or whether a boundary layer of
 918 vapor mass fraction developing from the dune leading edge may dominate the exchange.
 919 Therefore it is opportune to validate mass transfer boundary conditions at the base of
 920 the ABL at a realistic field scale with direct flux measurements from within the dune.

921 In this context, the capacitance probe described in section 2 provides an alterna-
 922 tive to traditional evaporation instruments by capturing spatio-temporal variations of
 923 the water vapor mass fraction Y just below the sand surface. As section 8 showed, an
 924 integration of the governing equations then returns a best estimate of the dimensionless
 925 instantaneous wind-driven seepage velocity u^* . At the surface, denoted by the subscript
 926 s , this yields the superficial gas velocity

$$927 \quad v_s^* = +(1 - \nu)u_s^* \quad (53)$$

928 counted > 0 into sand from the atmospheric boundary layer (ABL).

929 In addition, by virtue of their accuracy and low noise, the recorded depth profiles
 930 of Y can be smoothed with a spline and differentiated to evaluate the vapor flux $\Psi_s'' =$
 931 $-\rho(1 - \nu)(D/\varpi)(\partial Y/\partial x)_s$ across the surface, again counted > 0 into sand. Made di-
 932 mensionless with $\rho_{st}\sqrt{\alpha/J}$, the diffusive flux in Eq. (32) augmented by its advection coun-
 933 terpart $u_s^*Y_s p^*/T_s^*$, constitutes a unique measurement of the mass transfer boundary con-
 934 dition at the base of ABL. As Appendix H shows from the integral equations of the bound-
 935 ary layer, the proper way is to count it > 0 into the ABL aloft as

$$936 \quad \Sigma^* \equiv -\Psi_s^* - \frac{p^*}{T_s^*}u_s^*(Y_s - Y_a). \quad (54)$$

937 In this determination, the principal uncertainty is associated with the tortuosity $\varpi \sim$
 938 $\pi/2$ (Shen & Chen, 2007), which we estimated for the nearly spherical and monodisperse
 939 grains of this dune.

940 As the panels of Figure 10 show, the diffusion flux into the ABL and its sign are,
 941 as expected, nearly proportional to the “driving potential” ($Y_s - Y_a$) in the second day,
 942 i.e. to the difference between the surface mass fraction Y_s and its ambient counterpart
 943 Y_a . However, two surprising observations stand out. First, the driving potential nearly
 944 vanishes during aeolian transport in the first day (Fig. 10A), while the flux maintains
 945 roughly the same magnitude (Fig. 10B). As discussed in section 12, we attribute this phe-
 946 nomenon to enhanced mass transfer by saltating particles, which effectively produce a
 947 Dirichlet boundary condition imposing $Y_s \simeq Y_a$ at the surface.

948 The second paradox is more puzzling. When the ABL is stable at night, the dry
 949 surface keeps losing moisture to the wetter ambient, in an apparent inversion of the pro-
 950 portionality between flux and driving potential. In addition, the net surface flux changes
 951 sign in the last quarter of the night, while the driving potential does not.

952 Profile measurements at our short weather station are not sufficient to resolve this
 953 paradox. However, data support the following comments. As Fig. 3C showed, the ABL
 954 is stable at night, when a colder dune at ~ 290 K gives up heat at long-wavelength in-
 955 frared $\sim 10 \mu\text{m}$, and unstable during the day, when warm air rises from sand stricken
 956 by a solar irradiation that exceeds wind-driven losses. Therefore, turbulent momentum
 957 in the ABL is coupled with natural convection during the day (Wyngaard, 2010). To cap-
 958 ture this effect, Monin and Obukhov proposed a similarity between the transports of mo-

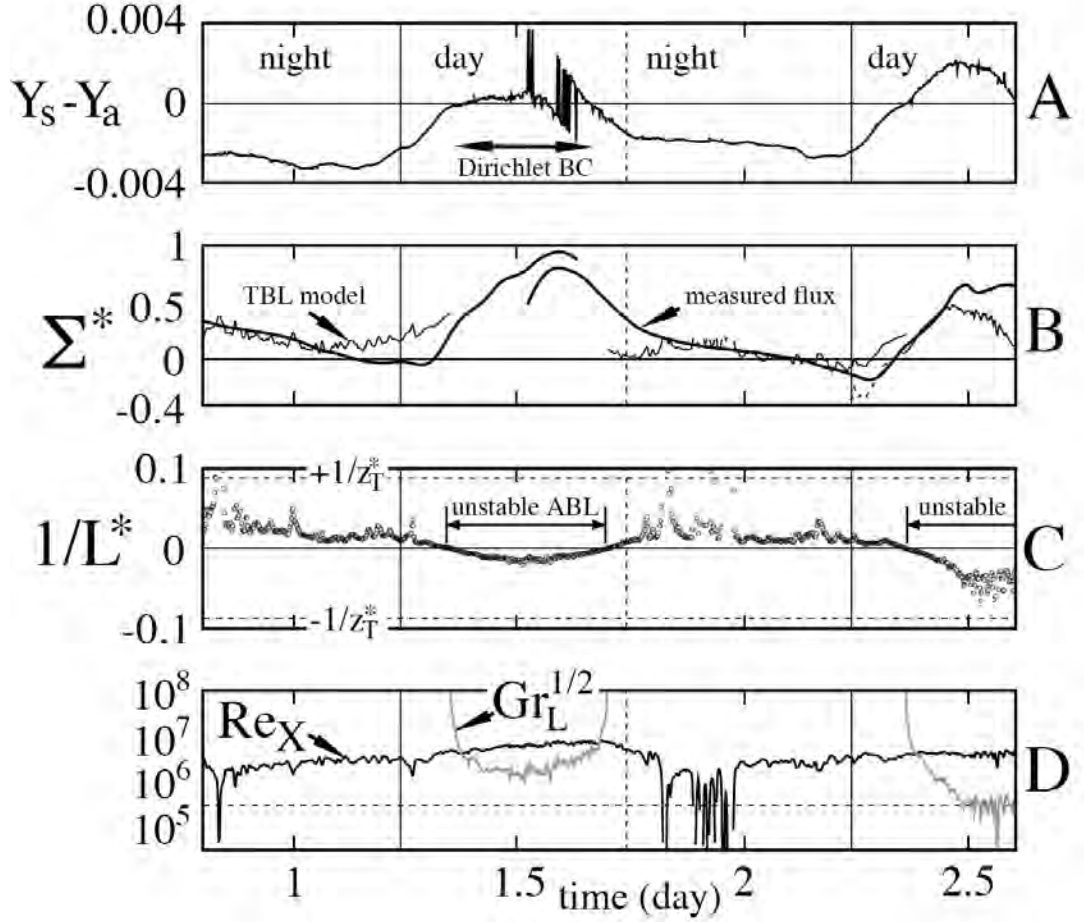


Figure 10. Time-histories in the atmospheric boundary layer (ABL). (A) Driving potential ($Y_s - Y_a$), nearly vanishing during aeolian transport from $t^* \simeq 1.4$ to 1.6 , thus imposing a Dirichlet boundary condition on the ABL. (B) Thick line: measured dimensionless net flux of Eq. (54). Thin line: Turbulent boundary layer (TBL) model of Eq. (57) with $a_m \simeq 0.0010$ and $a_m \simeq 0.0015$ under stable ($L > 0$) and unstable ($L < 0$) conditions, respectively, $\Sigma_\infty^* \simeq 0.43$ in the first night, $\Sigma_\infty^* \simeq 0.22$ in the second night, and $\Sigma_\infty^* \simeq 0.075$ in the second day. Dotted line: TBL model of the second day extrapolated to the period of stability after sunrise. (C) Inverse Monin-Obukhov length, dimensionless with $\sqrt{\alpha J}$; dotted lines at \pm the inverse dimensionless altitude z_T of the top RH sensor. (D) Re_X and $Gr_L^{1/2}$. The horizontal dashed line marks $Re_{X,crit}$ (Kays & Crawford, 1980).

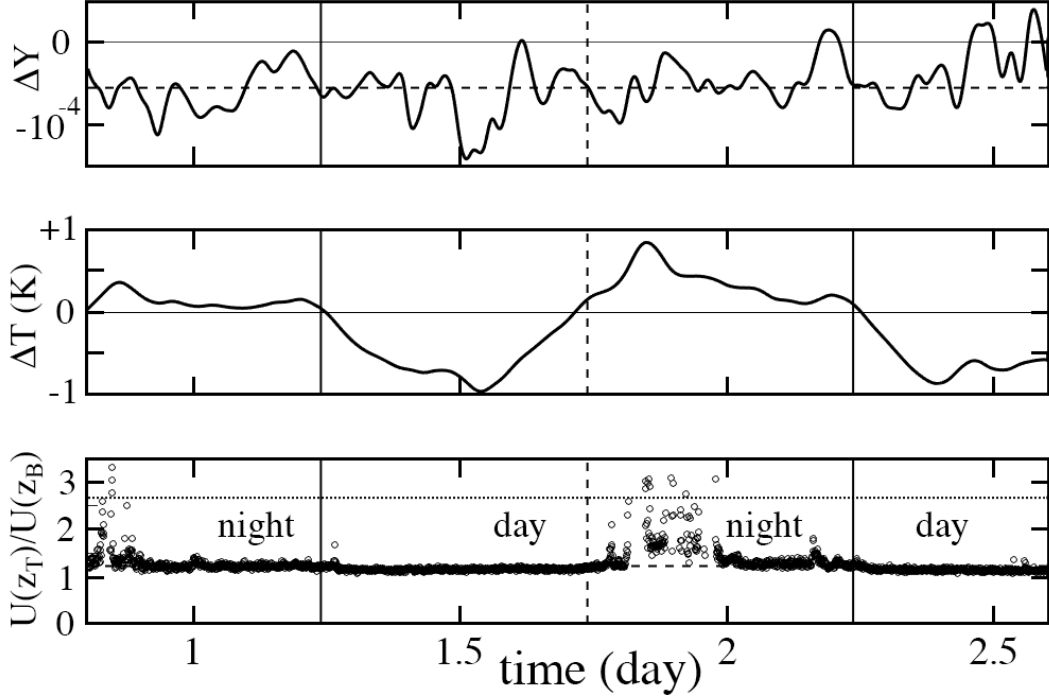


Figure 11. (A) Small difference $\Delta Y_a = Y_a(z_T) - Y_a(z_B)$ in the ambient water vapor mass fraction time-history between the top and bottom sensor elevations at $z_T \simeq 2$ m and $z_B \simeq 0.9$ m measured by the weather station above hard ground with much higher aerodynamic roughness $z_0 \simeq 0.011$ m (Louge et al., 2013) than found over the sand surface. Vertical lines mark sunrise and sunset. The horizontal dashed line is the mean ΔY_a . (B) Corresponding change in ambient temperature $\Delta T = T(z_T) - T(z_B) \equiv T_T - T_B$ ($^{\circ}\text{K}$). (C) Ratio $U(z_T)/U(z_B)$. The horizontal dashed and dotted lines show $\ln(z_T/z_0)/\ln(z_B/z_0)$ and z_T/z_B , respectively consistent with a turbulent log-law and a viscous sublayer.

959 momentum, heat and mass in the turbulent ABL (Monin, 1970), which we summarize in Ap-
 960 pendix D. The similarity is captured by corrections to the Prandtl-von Kàrmàn log-law
 961 of the wall using heuristic functions $\phi_m(z/L)$, $\phi_h(z/L)$ and $\phi_Y(z/L)$ for momentum, heat
 962 and moisture. In these functions, the altitude z is measured against the Monin-Obukhov
 963 length

$$964 \quad L = \frac{(\rho c_p T) v_\tau^3}{\kappa g \dot{q}''_{\text{wind}}}, \quad (55)$$

965 which is positive when the cold dune is warmed by a stable ABL at night ($\dot{q}''_{\text{wind}} > 0$),
 966 and negative when an unstable ABL cools off sand during the day. In Eq. (55), g is the
 967 gravitational acceleration, $\kappa \simeq 0.41$ is von Kàrmàn's constant, T is absolute temper-
 968 ature, and \dot{q}''_{wind} is the convective thermal flux at the surface. (Note that, because we
 969 count $\dot{q}''_{\text{wind}} > 0$ *into* sand, the expression of L in Eq. (55) has opposite sign than most
 970 conventions for the ABL). For example, field tests in Kansas in 1968 conformed to

$$971 \quad \phi_m = \begin{cases} 1 + a_{m_N} z/L & , L > 0 \\ 1/(1 - a_{m_D} z/L)^{1/4} & , L < 0 \end{cases} \quad (56)$$

972 with coefficients $a_{m_N} \simeq 4.8$ and $a_{m_D} \simeq 19.3$ (Wyngaard, 2010). At low altitudes such
 973 that $z \ll |L|$, all three functions tend to 1, and the log-law remains unchanged. Such
 974 is the case for our relatively short weather station (Fig. 10C).

975 The Monin-Obukhov analogy was meant for a fully-developed ABL established over
 976 vast, uniform, flat expanses, like the horizontal desert floor surrounding our sparsely-populated
 977 barchan dunes. However, it is questionable whether its mass transfer predictions apply
 978 to the dune itself during the day, or whether it is altogether valid under stratified, weak
 979 turbulence at night (Mahrt, 2014; Optis et al., 2014).

980 As Fig. 11A shows, ambient moisture changes negligibly with altitude at the weather
 981 station, $\Delta Y_a \simeq -0.01 Y_a$, in contrast with the noticeable difference in ambient temper-
 982 ature at the same location (Fig. 11B). Therefore, the moisture flux through the hard,
 983 relatively more impermeable desert floor should be very small. However, our measure-
 984 ments reveal that it is significant above the porous sand surface (Fig. 10B), which typ-
 985 ically traps more moisture during long periods without rain (Louge et al., 2013). Con-
 986 sequently, the windward toe of the dune likely constitutes the leading edge of a turbu-
 987 lent mass transfer boundary layer (TBL) driven by forced horizontal convection, devel-
 988 oping below an ABL subject to vertical natural convection when unstable, and stratifi-
 989 fied otherwise.

990 We consider such boundary layer in Appendix H. To establish its Reynolds number
 991 $\text{Re}_X \equiv \rho U \mathcal{X} / \mu$ at the probe, where $\mu \simeq 1.8 \cdot 10^{-5}$ kg/m.s is the air dynamic vis-
 992 cosity, we calculate the distance \mathcal{X} from the toe to the buried probe along the instan-
 993 taneous wind direction. As the dashed line in Fig. 10D shows, Re_X almost always ex-
 994 ceeds the critical value $\text{Re}_{X_{\text{crit}}} \simeq 3 \times 10^5$ for transition to a TBL, except from sunset
 995 to midnight, when the lower ABL intermittently behaves as a viscous sublayer or as log-
 996 law turbulence (Fig. 11C).

997 To make the TBL analysis tractable, we invoke the integral equations of the bound-
 998 ary layer (Kays & Crawford, 1980), and adopt the analogy between turbulent heat and
 999 mass transfer to estimate a Stanton number capturing wind-driven mass transfer. We
 1000 account for exchanges at the upper boundary of the TBL by including a vapor flux $\dot{\Sigma}''_\infty$
 1001 counted > 0 into the ABL aloft. Equation (H6) then predicts the net dimensionless flux,
 1002 which we equate to what we measured in Eq. (54),

$$1003 \quad \Sigma^* \equiv -\Psi_s^* - \frac{p^*}{T_s^*} v_s^* (Y_s - Y_a) = a_m \frac{\rho^* U^* (Y_s - Y_a)}{\text{Re}_X^{1/5} \text{Sc}^{0.4}} + \Sigma_\infty^*, \quad (57)$$

1004 where $\rho^* \equiv \rho/\rho_{\text{st}} \simeq p^*/T_T^*$ is the relative air density in the TBL, and $\text{Sc} \equiv (\mu/\rho)/D \simeq$
 1005 0.60 is the Schmidt number. As Fig. 10 shows, this prediction requires a value of a_m about

1006 an order of magnitude smaller than a typical laboratory correlation $a_m \simeq 0.0307$ for
 1007 the TBL over a flat plate (Kays & Crawford, 1980), suggesting a much thicker TBL than
 1008 expected. However, this disagreement may not be surprising, since Reynolds et al. (1958)
 1009 fixed a_m for heat transfer (not mass transfer) at Reynolds numbers within $9.2 \cdot 10^4 < \text{Re}_X <$
 1010 $1.27 \cdot 10^6$, which are below values in Fig. 10D, except during quiet periods at night. An-
 1011 other possible reason for the discrepancy may be a possible gradual evolution of Y_s along
 1012 the dune, which we did not measure. Lastly, to gauge whether the apparent TBL thicken-
 1013 ing may be associated with the presence of strong natural convection during the day,
 1014 Fig. 10D also compares Re_X with the square root of a Grashof number $\text{Gr}_L^{1/2} \equiv \rho[gL(T_s -$
 1015 $T_T)/T_T]^{1/2}L/\mu$, which amounts to a Reynolds number based on L and speed driven by
 1016 buoyant air rising from the hot surface at T_s and the colder measured ambient temper-
 1017 ature T_T . However, because $\text{Gr}_L^{1/2} < \text{Re}_X$ during much of the day, natural convection
 1018 is unlikely to dominate mass transfer in the TBL.

1019 At night, fitting our data to Eq. (57) also suggests a strong upward vapor flux Σ_∞^*
 1020 at the top edge of the TBL, perhaps due to a moisture inversion above the dune, whereby
 1021 dry air aloft lurks above a more humid layer closer to the surface (Mahrt, 2014). How-
 1022 ever, because the turbulent behavior of the stable night-time ABL is complex (Optis et
 1023 al., 2014; Mortarini et al., 2016), we do not know whether this interpretation has merit.
 1024 In future, detailed profiles of Y_a , T and U vs elevation should be simultaneously estab-
 1025 lished above a capacitance instrument recording surface moisture flux to inform the de-
 1026 tailed behavior of the mass transfer ABL, especially at night.

1027 14 Conclusions

1028 In this work, we deployed a unique capacitance instrument of fine vertical resolu-
 1029 tion to measure spatio-temporal variations of water mass fraction adsorbed on sand grains
 1030 in the hygroscopic regime without free liquid, as well as stratigraphy of the solid volume
 1031 fraction, within the first 30 cm from the surface of a hyper-arid dune. We simultaneously
 1032 recorded temperature profiles there, as well as ambient conditions, net solar radiation,
 1033 and wind speed and direction. We also characterized relevant sand properties, includ-
 1034 ing the van der Waals isotherm that relates water mass fraction in the bulk solid to rel-
 1035 ative humidity around grains at equilibrium.

1036 Unlike heat, which propagates mainly through the sand contact network by con-
 1037 duction, water vapor diffuses and advects through the tortuous interstitial pore space
 1038 between grains. As a result, its governing equations are more complicated and lead to
 1039 richer physics. Accordingly, we derived a partial differential equation (PDE) describing
 1040 the unsteady advection-diffusion of water vapor in that space without free liquid, cou-
 1041 pled with an ordinary differential equation (ODE) capturing evaporation kinetics of wa-
 1042 ter adsorbed on solid grains.

1043 We used this framework to interpret data. First, we considered long diurnal time
 1044 scales, during which grains have ample opportunity to achieve thermodynamic equilib-
 1045 rium with the surrounding relative humidity. Here, the source term in the solid phase
 1046 ODE effectively augments the unsteady term of the water vapor PDE. The result is an
 1047 apparent vapor diffusion that is nearly three orders of magnitude slower than without
 1048 any solid. In simpler terms, each dry sand layer hinders vapor diffusion by adsorbing mois-
 1049 ture before letting it proceed to the next layer.

1050 Another attribute of the long-term equilibrium behavior is a strong coupling be-
 1051 tween depth profiles of water vapor mass fraction and temperature. As the latter evolves
 1052 on a diurnal basis, the non-linear coupling produces multiple inflections in moisture mass
 1053 fraction that have no counterpart in linear diffusive systems. It originates in the depen-
 1054 dence of the amount of adsorbed water on interstitial relative humidity, which varies ex-
 1055 ponentially with temperature through the saturation pressure. We considered two other

1056 transport processes driven by strong temperature gradients, namely the Soret effect and
1057 natural convection. However in our case, both proved negligible.

1058 The porous matrix created by well-rounded packed sand also allows a slow “seep-
1059 age” advection to compete with diffusion, or to augment it. To evaluate its velocity at
1060 each measurement time step, we transformed the coupled governing equations into a sin-
1061 gle ODE along depth, which we solved as a two-point boundary value problem subject
1062 to the measured vapor mass fraction just below the surface and at the deepest probe sen-
1063 sor that consistently yielded a stable signal. We then selected the seepage velocity that
1064 presented the smallest least-squares error between ODE prediction and data.

1065 Separately, we showed that seepage is caused by gentle variations in dune topog-
1066 raphy that induce streamwise surface static pressure oscillations decaying exponentially
1067 with depth, thereby creating Darcy pressure gradients that effectively amplify small to-
1068 pographical deformations. As such, seepage changes from vapor inhalation to exhalation
1069 along the surface, and it depends on wind direction.

1070 Then, we applied the governing equations to the other limit where water mass frac-
1071 tion varies on short time scales. This let us elucidate a peculiar moisture wave phenomenon,
1072 whereby disturbances in vapor mass fraction on the dune surface propagate rapidly down-
1073 ward into its sands. A linear stability analysis of the governing equations identified the
1074 origin of these evanescent waves. Whereas subsurface moisture transport on the deci-
1075 metric scale operated in an effective diffusion limit, we showed that the microscopic size
1076 of the interstitial space between grains was too small for the evaporation process itself
1077 to be diffusion-limited. Accordingly, we derived an estimate for the characteristic time
1078 of first-order drying kinetics from the exponential decay of the moisture wave amplitude
1079 with depth. Here, data suggested a drying process at the grain scale that is limited by
1080 the kinetics of a reaction with activation energy larger than, but on the order of, the la-
1081 tent heat of vaporization.

1082 Finally, the depth profiles of water mass fraction Y allowed us to determine the time-
1083 history of the moisture flux into the atmospheric boundary layer (ABL). To our knowl-
1084 edge, this constitutes the first direct measurement of this quantity on a hyper-arid sur-
1085 face. We registered three unexpected observations. First, when the flux was, as antic-
1086 ipated, nearly proportional to the difference ($Y_s - Y_a$) between vapor mass fraction at
1087 the surface and in the ambient, it was about an order of magnitude smaller than pre-
1088 dicted for a turbulent mass transfer boundary layer developing from the dune toe, or by
1089 a Monin-Obukhov correlation of the ABL. Second, during aeolian sand transport, the
1090 flux was effectively decoupled from a vanishing ($Y_s - Y_a$). Third and most intriguing,
1091 although the flux slowly decreased in unison with ($Y_s - Y_a$) during the stable ABL at
1092 at night, it was augmented by a nearly invariant upward moisture flux aloft. To elucidate
1093 these observations in future, detailed profiles of vapor mass fraction Y , wind speed U
1094 and temperature T in the ABL should be recorded just above probes measuring Y and
1095 T in the subsurface.

1096 The capacitance instrument and modeling framework that we presented in this ar-
1097 ticle have wider relevance than hyper-arid dunes. In industry, they can be deployed, for
1098 example, to predict vapor contamination through pharmaceutical powders (Louge et al.,
1099 2021). Because the probe can reliably detect very low moisture, it could also be used as
1100 “ground-truth” for satellite remote sensing over sand seas (Zribi et al., 2014; Myeni et
1101 al., 2019; Bürgi & Lohman, 2021), or to look for scant water in future space applications (Honniball
1102 et al., 2020; Davidsson & Hosseini, 2021).

1103 Studies of the Earth life-sustaining Critical Zone have underscored the importance
1104 of water exchange at interfaces among the zone’s compartments (Sprenger et al., 2019).
1105 In temperate regions, the top soil often behaves as an unsaturated porous medium, where
1106 liquid water content is reliably measured (Kizito et al., 2008; Kidron & Kronenfeld, 2020),

albeit on a relatively coarse spatial resolution. There, the principal challenge is to specify the water retention curve, a history-dependent relation between water volume fraction and capillary pressure subject to “return-point” memory hysteresis, which is predictable for known pore networks (Xu & Louge, 2015), but is typically modeled instead with the Van Genuchten (1980) empirical correlation, see for example Assouline and Kamai (2019), or with local closures involving meniscus curvature (Gray & Miller, 2005) that elicit controversy (Baveye, 2013).

For hyper-arid soils without free liquid, measurements of small amounts of water adsorbed on solids lacked until now the spatial resolution and accuracy that could reveal the essential physics of water transport. With such instrument at hand, we have shown that a model free of arbitrary closures can capture observations and record the exchange of moisture at the soil-atmosphere interface. Recent improvements in the stability of the instrument’s processing electronics suggest that its range can be extended to greater water content (Louge et al., 2021), thereby enabling measurements into the more humid vadose zone with a single instrument.

Appendix A Multiple capacitance probe

Louge et al. (1997) developed capacitance instruments to measure density and dielectric signature of snow. Recently, Louge et al. (2021) improved their data reduction to reach unprecedented accuracy in pharmaceutical applications. Our design is based on a similar principle (Fig. 1). The probe records the impedance of the medium between any one of 15 sensors and a “target” held at a constant reference voltage. To achieve this, conductors carrying a sensor voltage are surrounded by a “guard” driven at precisely the same potential by an independent circuit. By guiding electric field lines that penetrate sand at the probe face, the guard focuses the extent of the probe’s measurement volume originating from the sensor, thereby avoiding external interference known as “stray” capacitance. Because the guard is also connected to the outer conductor of a high-quality coaxial cable connecting probe and processing electronics, it also shields the wire and all electrical components carrying the sensor voltage. Therefore, because there can be no charge accumulation in the cable, the latter’s capacitance does not perturb the measurement, unlike conventional bridge circuits. Consequently, this technique allows precise detection of extremely small capacitances.

For the invasive design in Fig. 1, symmetry produces circular electric field lines that are shed from sensor to target in planes perpendicular to the long axis of the probe. Their center lies on the target conductor at a distance x_c from the centerline and with radius R satisfying $x_c^2 - R^2 = a^2$, where $a \simeq 12.6$ mm is the half guard width (Louge et al., 1996). These field lines delimit a measurement volume of $W \simeq 5$ mm vertical spatial resolution set by the sensor height W , small enough to resolve steep gradients of Ω perpendicular to the free surface. In the probe of Fig. 1, each sensor has respective outer and inner distances $b \simeq 11.8$ mm and $c \simeq 4.8$ mm from the lance’s centerline. It is separated from the grounded target by a thin guarded strip that absorbs the singular voltage jump from AC guard to DC target. As Louge et al. (1996) calculated, this makes the measurement volume penetrate sand no farther than $(a^2 - c^2)/2c \simeq 14$ mm from the probe. It also confers each sensor a capacitance $C_0 = \epsilon_0 \ell_c = \epsilon_0 (W/\pi) \ln\{(b+a)(c-a)/[(b-a)(c+a)]\} \simeq 38 \cdot 10^{-15}$ F when the probe is exposed to air or, equivalently, $\ell_c \simeq 4.3$ mm.

Such tight dimensions are achieved by deploying all conductive surfaces in a thin printed-circuit board (PCB) consisting of four layers. The top one is where sensor, guard and target are exposed to sand. To limit wear, it is covered with a thin TAIYO PSR-4000BN solder mask. The next layer is a copper film held at guard voltage, designed to shield the back of all sensors. The third layer contains wires of resistance $\lesssim 1 \Omega$ bringing sensor voltages to a location where each can be individually soldered to one of 15 wires as-

1158 sembled into a guarded coaxial cable ~ 1.5 m linking probe and processing electronics.
 1159 Finally, the bottom PCB layer is another guarded copper film shielding these sensor wires.
 1160 Our PCB was printed by ADVANCED CIRCUITS.

1161 Coincidentally, the thin solder mask, which equilibrates quickly to the local interstitial
 1162 vapor mass fraction Y , also lets the probe discern rapid changes in that quantity,
 1163 even if sand lags in achieving an adsorbed mass fraction Ω_e at equilibrium with Y . Al-
 1164 though Ω is the primary variable determining the recorded complex effective dielectric
 1165 constant, adsorbed moisture on the film, which is closest to sensor and ground, can af-
 1166 fect the electric field, thereby acting as an impedance in series with the sand’s, regard-
 1167 less whether Ω has reached Ω_e . We noticed this behavior when the phase lead of the bare
 1168 probe in moist air disappeared after it was briefly dried in an oven. While it is unclear
 1169 whether the probe detects rapid variations in Y quantitatively, we exploited such capa-
 1170 bility to reveal the signal bistability shown in Fig. 3, which we analyzed in section 12.

1171 The electronics, manufactured by CAPACITEC, supplies sensors with a current of
 1172 constant amplitude by controlling the AC voltage across a reference impedance fed with
 1173 a stable “clock” oscillator of frequency $f \simeq 15.6254$ kHz, thereby producing sensor and
 1174 guard voltage amplitudes proportional to the impedance between sensor and ground (Louge
 1175 et al., 1997). When the probe is exposed to air alone, its impedance $Z_0 = (2\pi f \iota C_0)^{-1}$
 1176 is only function of the capacitance C_0 between sensor and target. In humid sand, the
 1177 impedance becomes $Z = [2\pi f C_0 (K_e'' + \iota K_e')]^{-1}$. By forming the ratio of guard voltage
 1178 amplitude in air V_0 and in sand V , the probe then records the modulus
 1179 $V_0/V = (K_e'^2 + K_e''^2)^{1/2}$. Louge et al. (2021) offer algorithms to determine guard am-
 1180 plitude and phase with high accuracy. Using them, the phase yields $\tan \varphi \equiv K_e''/K_e'$
 1181 and, ultimately, as shown in section 4, the acquired clock and guard signals provide sand
 1182 bulk density and Ω simultaneously at each sensor (Louge, Valance, Babah, et al., 2010).

1183 The PCB is backed by a rigid composite lance made of DELRINTM plastic and a
 1184 glass filler, with effective heat conductivity $\simeq 0.35$ W/m. $^\circ$ K. This precaution minimizes
 1185 thermal interference with surrounding sands of similar conductivity $k_s \simeq 0.49$ W/m.K.
 1186 (A metal probe, which we tried unsuccessfully, dried sand deeply by conducting heat from
 1187 the surface at high noon). The hard-plastic housing lance is tapered to an asymmetric
 1188 thin edge with 10° angle to impart minimum sand compression in front of the sensors
 1189 during probe insertion.

1190 The top-rear of the lance supports a carefully-guarded enclosure to shield 15 sensor
 1191 wires connecting the PCB to a AMPHENOL multi-position circular connector plug.
 1192 The latter serves as quick connection with a guarded coaxial cable carrying all 15 sensor
 1193 wires to a guarded multiplexer. Upon receiving a five-bit binary address, the mul-
 1194 tiplexer operates relay switches to connect one of the sensors to the processing electron-
 1195 ics, while guarding all other. Relays and digital electronics in the multiplexer are power-
 1196 ered by a small battery. To avoid stray capacitances within the multiplexer, the DC volt-
 1197 age of this battery is made to “float” with respect to the ground reference of the probe,
 1198 i.e. these two voltages are strictly independent.

1199 A compact Field Programmable Gate Array (FPGA) deployed in a NATIONAL IN-
 1200 STRUMENT cRIO controls the multiplexer by sending it a binary address through a NI-
 1201 9401 module, consistent with a pre-programmed schedule. The cRIO acquires 150 clock
 1202 and guard voltages simultaneously using two separate synchronous NI-9201 data acqui-
 1203 sition cards at a rate of 350 kS/s. It also acquires data from the Kipp & Zonen radiome-
 1204 ter and the temperature probe of Louge et al. (2013). Finally, the cRIO orchestrates data
 1205 storage on a USB-A memory flash drive. After retrieval from the latter, a MATLAB al-
 1206 gorithm described by Louge et al. (2021) calculates K_e' and K_e'' . The system is powered
 1207 by a distant 12 V lead-acid battery recharged by a 1 kW solar panel, or by lithium-polymer
 1208 battery packs buried nearby for minimal footprint.

1209 Appendix B Size distribution

1210 In the film adsorption regime, spherical sand particles of diameter d and material
 1211 density ρ_p at equilibrium with the surrounding RH $_e$ have masses $(\pi/6)d^3\rho_p$ of solid and
 1212 $\pi d^2\ell_w\rho_w$ of liquid, thereby holding a solid-bound water mass fraction

$$1213 \Omega_{d,e} = \frac{\Omega_{1_d}}{[T^* \ln(1/\text{RH}_e)]^{1/3}} \simeq \frac{\Omega_{1_d}}{\{T^* \ln[p_{\text{sat}}/(pM^*Y_e)]\}^{1/3}}, \quad (\text{B1})$$

1214 where

$$1215 \Omega_{1_d} = \frac{6\ell_0 \rho_w}{d \rho_p} \quad (\text{B2})$$

1216 is inversely proportional to grain diameter (Shahraeeni & Or, 2010). In these expressions,
 1217 the subscripts e and d indicate, respectively, equilibrium and the particle size class of di-
 1218 ameter d . To average Ω_{1_d} over the entire population, we use the normalized particle size
 1219 distribution f_M , such that the elementary mass fraction of grains with diameter in the
 1220 range $[d, d + dd]$ is $f_M dd$. The result

$$1221 \Omega_1 = \int_{d=0}^{\infty} \Omega_{1_d} f_M dd = 6\ell_0 \frac{\rho_w}{\rho_p} \int_{d=0}^{\infty} f_M \frac{dd}{d} = \frac{6\ell_0 \rho_w}{d_{2,3} \rho_p}, \quad (\text{B3})$$

1222 which appears in the isotherm of Eq. (3), involves the ‘‘Sauter’’ diameter $d_{2,3}$. It is ob-
 1223 tained by relating $f_M = d^3 f_N / \int_0^\infty f_N d^3 dd$ to the normalized population size distribu-
 1224 tion f_N . The notation $d_{2,3}$ adopts the convention of Babinsky and Sojka (2002),

$$1225 d_{p,q} \equiv \left[\frac{\int_0^\infty d^p f_N dd}{\int_0^\infty d^q f_N dd} \right]^{1/(p-q)}. \quad (\text{B4})$$

1226 Louge et al. (2013) provided moments of the measured distribution f_M , summarized in
 1227 their supporting information.

1228 Appendix C Isotherm derivatives

1229 We define

$$1230 \frac{\partial \Omega_e}{\partial t} \equiv \Omega_1 \left[\frac{f_T}{T_{\text{st}}} \frac{\partial T}{\partial t} + f_Y \frac{\partial Y}{\partial t} + \frac{f_p}{p_{\text{st}}} \frac{\partial p}{\partial t} \right] \quad (\text{C1})$$

$$1231 = \left[\left(\frac{\partial \Omega_e}{\partial T} \right)_{\text{RH}} + \left(\frac{\partial \Omega_e}{\partial \text{RH}} \right)_T \times \left(\frac{\partial \text{RH}}{\partial T} \right)_{Y,p} \right] \frac{\partial T}{\partial t}$$

$$1232 + \left[\left(\frac{\partial \Omega_e}{\partial \text{RH}} \right)_T \times \left(\frac{\partial \text{RH}}{\partial Y} \right)_{p,T} \right] \frac{\partial Y}{\partial t}$$

$$1233 + \left[\left(\frac{\partial \Omega_e}{\partial \text{RH}} \right)_T \times \left(\frac{\partial \text{RH}}{\partial p} \right)_{T,Y} \right] \frac{\partial p}{\partial t},$$

1234 where subscripts indicate which variables are held constant in calculating the derivative.
 1235 Differentiating Eq. (3) and Eqs. (6)-(7), we find

$$1236 \left(\frac{\partial \text{RH}}{\partial Y} \right)_{p,T} = \left(\frac{p}{p_{\text{sat}}} \right) \frac{M^*}{[1 + Y(M^* - 1)]^2}, \quad (\text{C2})$$

$$1237 \left(\frac{\partial \text{RH}}{\partial T} \right)_{Y,p} = -\text{RH} \frac{T_{A_a}}{(T - T_{A_0})^2},$$

$$1238 \left(\frac{\partial \text{RH}}{\partial p} \right)_{T,Y} = \frac{M^*}{p_{\text{sat}}} \times \frac{Y}{1 + Y(M^* - 1)},$$

1239 and

$$1240 \quad \frac{1}{\Omega_1} \left(\frac{\partial \Omega_e}{\partial T} \right)_{\text{RH}} = - \frac{1}{3T_{\text{st}} \ln^{1/3}(1/\text{RH})} \left(\frac{T_{\text{st}}}{T} \right)^{4/3}, \quad (\text{C3})$$

$$1241 \quad \frac{1}{\Omega_1} \left(\frac{\partial \Omega_e}{\partial \text{RH}} \right)_T = \frac{1}{3\text{RH} \ln^{4/3}(1/\text{RH})} \left(\frac{T_{\text{st}}}{T} \right)^{1/3},$$

1242 which can be substituted into Eq. (C1) to find expressions for the dimensionless func-
1243 tions f_T , f_Y and f_p in terms of Y , T and p . In particular,

$$1244 \quad f_Y \equiv \frac{1}{\Omega_1} \left(\frac{\partial \Omega_e}{\partial Y} \right)_{T,p} = \quad (\text{C4})$$

$$1245 \quad \frac{1/3}{Y [1 + Y(M^* - 1)] T^{*1/3} \ln^{4/3}(1/\text{RH})} \simeq \frac{1/3}{YT^{*1/3} \ln^{4/3}[p_{\text{sat}}/(pM^*Y)]}.$$

1246 Because grains of diameter d have isotherms captured by Eq. (B1), they are individu-
1247 ally subject to Eqs. (C3)-(C4), in which $\Omega_{1,d}$ is substituted for its average Ω_1 over the
1248 particle size distribution.

1249 Appendix D Monin-Obukhov similarity

1250 In the spirit of Prandtl's mixing length hypothesis, Monin and Obukhov postulated
1251 that the turbulent transport of momentum is coupled to the fluxes of heat \dot{q}_{wind}'' and va-
1252 por mass $\dot{\Psi}''$ in the ABL through the similarity (Monin, 1970)

$$1253 \quad \rho v_\tau^2 = \frac{\kappa z \rho v_\tau}{\phi_m} \frac{\partial U}{\partial z}, \quad (\text{D1})$$

$$1254 \quad \dot{q}_{\text{wind}}'' = \frac{\kappa z \rho c_p v_\tau}{\phi_h \text{Pr}_t} \frac{\partial T}{\partial z},$$

$$1255 \quad \dot{\Psi}'' = \frac{\kappa z \rho v_\tau}{\phi_Y \text{Sc}_t} \frac{\partial Y_a}{\partial z},$$

1256 where κz is the mixing length, c_p is specific heat at constant pressure, and Pr_t and Sc_t
1257 are, respectively, turbulent Prandtl and Schmidt numbers that Monin (1970) called "ra-
1258 tios of exchange coefficients" between heat and momentum or mass and momentum. Note
1259 that, for consistency with the internal flux, $\dot{\Psi}''$ and \dot{q}_{wind}'' in the ABL are positive down-
1260 ward. The quantities ϕ_m , ϕ_h and ϕ_Y are heuristic functions of the relative altitude z/L
1261 mentioned in section 13. For heat transfer, Louge et al. (2013) adopted

$$1262 \quad \phi_h = \begin{cases} 1 + a_{h_N} z/L & , L > 0 \\ 1/(1 - a_{h_D} z/L)^{1/2} & , L < 0 \end{cases} \quad (\text{D2})$$

1263 with coefficients $a_{h_N} \simeq 7.8$ and $a_{h_D} \simeq 12$.

1264 Making ρ , T , v_τ , \dot{q}_{wind}'' and z dimensionless with ρ_{st} , T_{st} , $(\alpha/J)^{1/2}$, $\rho_{\text{st}} c_p T_{\text{st}} (\alpha/J)^{1/2}$
1265 and $(\alpha J)^{1/2}$, respectively, the unsteady heat balance in the ABL is

$$1266 \quad \left(\frac{\text{Pr}_t e^\xi}{\kappa v_\tau^*} \right) \frac{\partial(\rho^* T^*)}{\partial t^*} = \frac{\partial}{\partial \xi} \left(\frac{\rho^*}{\phi_h} \frac{\partial T^*}{\partial \xi} \right), \quad (\text{D3})$$

1267 where we define $\xi \equiv \ln z$. Because $\rho^* T^* = p^*$ is invariant at constant atmospheric pres-
1268 sure $p^* \equiv p/p_{\text{st}}$, Eq. (D3) has no unsteady term, and the flux is independent of z . In-
1269 tegrating it between the surface at $z = z_0$ (index s) and the altitude z_T where ambi-
1270 ent temperature T_T is measured, we find

$$1271 \quad T^*(z^*) = T_s^* \exp \left[\frac{\Phi_{2h}(z^*/L^*)}{\Phi_{2h}(z_T^*/L^*)} \ln \left(\frac{T_T^*}{T_s^*} \right) \right], \quad (\text{D4})$$

1272 where we take T_s to be the temperature measured at the buried sensor closest to the sur-
 1273 face, and the integral function is

$$1274 \quad \Phi_{2h}(z) \equiv \int_{\xi=z_0}^z \phi_h d \ln \xi. \quad (D5)$$

1275 From Eq. (D1), the dimensionless heat flux is then

$$1276 \quad q^* = \frac{\kappa v_\tau p^*}{\text{Pr}_t \Phi_{2h}(z_T^*/L^*)} \ln \left(\frac{T_T^*}{T_s^*} \right). \quad (D6)$$

1277 Meanwhile, the Monin-Obukhov length in Eq. (55), dimensionless with $(\alpha J)^{1/2}$, satis-
 1278 fies the equation

$$1279 \quad L^* = \left(\frac{\alpha}{J^3 g^2} \right)^{1/2} \frac{v_\tau^{*2} \text{Pr}_t \Phi_{2h}(z_T^*/L^*)}{\kappa^2 \ln(T_T^*/T_s^*)}, \quad (D7)$$

1280 which we solve for L^* using time-histories of the measured wind speed U , temperatures
 1281 T_T and T_s reported in section 4, $v_\tau/U \simeq 0.036$ measured at the probe location in Jan-
 1282 uary 2017, and adopting $\text{Pr}_t \simeq 1$.

1283 Appendix E Soret coefficient

1284 Chapman and Cowling (1953) used the kinetic theory to derive the Soret diffusion
 1285 mass flux $-\rho(D/\varpi)k_T \nabla \ln T$ of a gas driven by a temperature gradient. They found

$$1286 \quad k_T = 5(C_s - 1) \frac{S_1[n_1/(n_1 + n_2)] - S_2[n_2/(n_1 + n_2)]}{Q_1(n_1/n_2) + Q_2(n_2/n_1) + Q_{12}}, \quad (E1)$$

1287 where $n_1 m_1$ is the partial density of gas 1 with molecular mass m_1 diffusing into gas 2.
 1288 Substituting 1 for 2 and vice-versa completes the set of equations. With water vapor (gas
 1289 1) dilute in air (gas 2), $n_1 m_1 = \rho Y$ and $n_2 m_2 = (1 - Y)\rho \simeq \rho$. Using the shorthand
 1290 $M_1 \equiv m_1/(m_1 + m_2)$, Chapman and Cowling (1953) calculated

$$1291 \quad \begin{aligned} S_2 &= M_2^2 E_2 - 3M_1(M_1 - M_2) - 4M_2 M_1 A_s & (E2) \\ Q_2 &= M_2 E_2 [6M_1^2 + (5 - 4B_s) M_2^2 + 8M_2 M_1 A_s] \\ Q_{12} &= 3(M_1 - M_2)^2 (5 - 4B_s) + 4M_1 M_2 A_s (11 - 4B_s) + 2M_1 M_2 E_1 E_2 \\ E_2 &= \frac{2\sqrt{2}}{5M_2 M_1^{1/2}} \left(\frac{\sigma_2}{\sigma_{12}} \right)^2 \\ \sigma_{12} &= (\sigma_1 + \sigma_2)/2, \end{aligned}$$

1296 with $A_s = 2/5$, $B_s = 3/5$ and $C_s = 6/5$. Because $n_1/n_2 \simeq M^* Y \ll 1$, where M^* is
 1297 the ratio of the molar masses of air and water, Eq. (E1) simplifies to $k_T \simeq -S_2 M^* Y / Q_2 \equiv$
 1298 $a_T Y$. With $M_1 = 1/(1 + M^*)$, $M_2/M_1 = M^*$, $\sigma_1 \simeq 2.65 \text{ \AA}$, $\sigma_2 \simeq 3.60 \text{ \AA}$, we find
 1299 $a_T \simeq -0.319$.

1300 With this magnitude, our calculations indicate that log derivatives of temperature
 1301 $\partial \ln T^*/\partial x^*$ and $\partial \ln T^*/\partial t^*$ are too small for terms involving a_T to play a significant role
 1302 in Eq. (49). Therefore in our case, the Soret effect can be ignored. In extra-terrestrial
 1303 applications with stronger temperature variations, this may no longer be the case.

1304 Appendix F Seepage profiles

1305 On time scales long enough to establish equilibrium, the mass conservation Eq. (15)
 1306 and the rate Eq. (24) can be manipulated to extract an ODE for the evolution of u^* along

1307 the relative depth x^* ,

$$\begin{aligned}
 1308 \quad \frac{\partial u^*}{\partial x^*} &= \left[-\frac{\partial \ln p^*}{\partial t^*} + \frac{\partial \ln T^*}{\partial t^*} + \frac{(M^* - 1)}{1 + Y(M^* - 1)} \frac{\partial Y}{\partial t^*} \right] \\
 1309 \quad &- u^* \left[\frac{\partial \ln p^*}{\partial x^*} - \frac{\partial \ln T^*}{\partial x^*} - \frac{(M^* - 1)}{1 + Y(M^* - 1)} \frac{\partial Y}{\partial x^*} \right] \\
 1310 \quad &- \mathbb{R}\Omega_1 \frac{T^*}{p^*} \left[f_T \frac{\partial T^*}{\partial t^*} + f_Y \frac{\partial Y}{\partial t^*} \right],
 \end{aligned} \tag{F1}$$

1311 which is coupled with Darcy's law (17) through the dimensionless term

$$1312 \quad \frac{\partial \ln p^*}{\partial x^*} = - \left(\frac{\mu\alpha}{Kp_{\text{st}}} \right) \frac{u^*}{p^*}. \tag{F2}$$

1313 These equations are solved with ODE (30), or with PDE (26). They are used to calcu-
 1314 late profiles of u^* in the insets of Fig. 7.

1315 Appendix G Kinetic limit

1316 In this Appendix, we estimate the time τ_d needed to bring the mass fraction Ω_d
 1317 held by a spherical grain of diameter d to its value Ω_{e_d} at equilibrium with the imposed
 1318 Y around it. This equilibration process is driven by the volumetric rate of evaporation
 1319 at the particle scale, which is governed by the surface mass flux \dot{W}_s'' expanding into the
 1320 interstitial space of density $\rho(1-\nu)$ surrounding grains. In Eq. (44), Y_e is the mass frac-
 1321 tion at equilibrium with the instantaneous Ω_d on the solid of size class d given by Eq. (B1).

1322 As in the combustion of a solid particle (Kanury, 1975), there are two limiting regimes.
 1323 In the ‘‘kinetic limit’’, k_m is small relative to $\rho D/d$, so diffusion erases gradients of Y ,
 1324 and the flux is given by Eq. (43), $\dot{W}_s'' = \dot{W}_{\text{HKS}}''$. Combining with Eq. (44), the charac-
 1325 teristic time of size class d is

$$1326 \quad \tau_d = \tau_{\text{HKS}} = \frac{\rho(1-\nu)d}{6\nu k_m} = \left(\frac{1-\nu}{\nu} \right) d \sqrt{\frac{\pi \text{MW}_{\text{H}_2\text{O}}}{18\hat{R}T}} \left(\frac{1-\kappa_c/2}{\kappa_e} \right), \tag{G1}$$

1327 which, upon averaging over the particle size distribution, would return the same expres-
 1328 sion with the Sauter diameter $d_{2,3}$ instead of d .

1329 If instead diffusion is not as fast, it is essential to involve it in the local water mass
 1330 balance, as the local vapor mass fraction \check{Y} may vary within each pore. For simplicity,
 1331 we imagine, crudely, that particles are isolated, as commonly assumed to derive closed-
 1332 form solutions for solid or droplet combustion (Kanury, 1975). Under quasi-steady condi-
 1333 tions $\partial \check{Y} / \partial t \simeq 0$, the mass flow rate through any spherical shell at radius r from the
 1334 particle center is invariant and equal to its value $\pi d^2 \dot{W}_s''$ at the surface. Then, the isother-
 1335 mal balance of water vapor mass in a slice $[r, r + dr]$ is

$$1336 \quad \pi d^2 \dot{W}_s'' \frac{\partial \check{Y}}{\partial r} - \rho D \frac{\partial}{\partial r} \left(r^2 \frac{\partial \check{Y}}{\partial r} \right) = 0. \tag{G2}$$

1337 At $r = d/2$, the net evaporation rate of a unit area of water film must balance the sum
 1338 of the advection and diffusion fluxes in the gas phase,

$$1339 \quad \dot{W}_s'' = \dot{W}_s'' Y_s - \rho D \left(\frac{\partial \check{Y}}{\partial r} \right)_s. \tag{G3}$$

1340 Integrating Eq. (G2) twice subject to $\check{Y} \rightarrow Y$ at $r \rightarrow \infty$ and boundary condition (G3),
 1341 we find

$$1342 \quad (1 - \check{Y}) = (1 - Y) \exp[-d^2 \dot{W}_s'' / (4\rho D r)], \tag{G4}$$

1343 where \dot{W}_s'' is given by Eq. (43). Applying this profile expression to the surface at $r =$
 1344 $d/2$ and eliminating Y_s using Eq. (43) yields an equation to solve for \dot{W}_s'' in the general
 1345 case,

$$1346 \quad 1 - Y_e + \frac{\dot{W}_s''}{k_m} = (1 - Y) \exp\left(-\frac{d\dot{W}_s''}{2\rho D}\right). \quad (\text{G5})$$

1347 As expected, we recover $\dot{W}_s'' = \dot{W}_{\text{HKS}}''$ in the kinetic limit by making $D \rightarrow \infty$. In the
 1348 “diffusion limit”, slow diffusion is the rate limiting step. Here, by making $k_m \rightarrow \infty$, \dot{W}_s''
 1349 becomes

$$1350 \quad \dot{W}_{\text{DIFF}}'' = \frac{2\rho D}{d} \ln\left(\frac{1 - Y}{1 - Y_e}\right) \simeq \frac{2\rho D}{d}(Y_e - Y), \quad (\text{G6})$$

1351 with characteristic time

$$1352 \quad \tau_{\text{DIFF}} = (1 - \nu)d^2/(12\nu D). \quad (\text{G7})$$

1353 Because an interstitial space with $\nu > 0.5$ has a pore size on the order of $d[(1-\nu)/\nu]^{1/3} <$
 1354 d , the time to diffuse vapor through this space should be even less than predicted by Eq. (G7).
 1355 Combining the profile Eq. (G4) with Eq. (G6), we also find $Y_s = Y_e$ in the diffusion limit.

1356 Expanding the exponential to first order in Eq. (G5) and recognizing that $Y \ll$
 1357 1 , the flux in the general case is approximately given by

$$1358 \quad \frac{1}{\dot{W}_s''} \simeq \frac{1}{\dot{W}_{\text{DIFF}}''} + \frac{1}{\dot{W}_{\text{HKS}}''}, \quad (\text{G8})$$

1359 confirming that the two limiting processes operate in parallel. Damköhler’s “second ra-
 1360 tio” $\text{Da}_{\text{II}} \equiv \tau_{\text{DIFF}}/\tau_{\text{HKS}} = k_m d/(2\rho D)$ reveals which mechanism predominates by be-
 1361 ing the slowest. A large Da_{II} implies the diffusion limit. With a unity accommodation
 1362 coefficient of evaporation ($\kappa_e \sim 1$), this would likely be the case, since $\text{Da}_{\text{II}} \sim 860$ for
 1363 our mean Sauter diameter under standard conditions. For example, to complement the
 1364 capillary condensation model of Philip (1964), Shahraeeni and Or (2010) postulated a
 1365 diffusion-limited process for film adsorption at the microscopic scale of wedge-shaped grain
 1366 asperities. However, as section 12 shows, the characteristic time involved $\tau_{\text{DIFF}} \sim 240 \mu\text{s}$
 1367 would be much too small to explain the exponential decay of ΔY with depth. There-
 1368 fore, the behavior of subsurface waves imply instead that the kinetic limit prevails at the
 1369 grain scale.

1370 Appendix H Developing mass transfer boundary layer

1371 We invoke integral equations of the boundary layer to model wind-driven convec-
 1372 tive mass transfer, coupled to the advection/diffusion measured through the sand sur-
 1373 face, with possible mass flux exchanged with the ABL aloft. Unlike Appendix D, where
 1374 we entertained unsteady terms, here we ignore them due to the more rapid development
 1375 of the turbulent mass transfer boundary layer (TBL). Overall mass conservation in a TBL
 1376 slice perpendicular to the surface is

$$1377 \quad \frac{d}{d\mathcal{X}} \int_{z=0}^{z_\ell} \rho U dz - \rho_\ell v_\ell + \rho_s v_s = 0, \quad (\text{H1})$$

1378 where \mathcal{X} is distance along the wind from the leading toe of the dune, v is superficial gas
 1379 velocity (> 0 toward sand), and indices s and ℓ represent the surface and the top of the
 1380 slice, respectively. The corresponding mass balance of water vapor is

$$1381 \quad \frac{d}{d\mathcal{X}} \int_{z=0}^{z_\ell} \rho U Y dz - \rho_\ell Y_\ell v_\ell + \rho_s Y_s v_s - \dot{\Psi}_\ell'' + \dot{\Psi}_s'' = 0, \quad (\text{H2})$$

1382 where vapor fluxes $\dot{\Psi}''$ are > 0 into sand. Eliminating $\rho_\ell v_\ell$ from Eq. (H2) using Eq. (H1),
 1383 dividing by $\rho_\ell U_\ell$ and letting $\ell \rightarrow \infty$, we find

$$1384 \quad \frac{d\delta_m}{d\mathcal{X}} + \frac{\rho_s v_s}{\rho_\infty U_\infty} - \frac{\dot{\Psi}_\infty''}{\rho_\infty U_\infty (Y_s - Y_\infty)} + \frac{\dot{\Psi}_s''}{\rho_\infty U_\infty (Y_s - Y_\infty)} = 0, \quad (\text{H3})$$

where ρ_∞ and U_∞ are recorded at an altitude higher than the mass transfer thickness of the boundary layer

$$\delta_m \equiv \int_{z=0}^{\infty} \frac{\rho U}{\rho_\infty U_\infty} \left(\frac{Y - Y_\infty}{Y_s - Y_\infty} \right) dz. \quad (\text{H4})$$

Because water vapor has a diffusion coefficient D on the same order as the thermal diffusivity of air or, equivalently, that its Lewis number is near unity, an analogy with heat transfer in the TBL suggests that $d\delta_m/d\mathcal{X}$ is a kind of Stanton number

$$\text{St}_X = \frac{d\delta_m}{d\mathcal{X}} \simeq \frac{a_m}{\text{Re}_X^{1/5} \text{Sc}^{0.4}}, \quad (\text{H5})$$

where $\text{Sc} \equiv (\mu/\rho)/D \simeq 0.60$ is the Schmidt number of water vapor diffusing in air. Then, from its standpoint, the ABL receives a net surface flux

$$\dot{\Sigma}'' \equiv -\dot{\Psi}_s'' - \rho_s v_s (Y_s - Y_a) = a_m \frac{\rho_\infty U (Y_s - Y_a)}{\text{Re}_X^{1/5} \text{Sc}^{0.4}} + \dot{\Sigma}_\infty'', \quad (\text{H6})$$

where $\dot{\Sigma}_\infty'' \equiv -\dot{\Psi}_\infty''$ is the upward moisture flux on top of the TBL, with both $\dot{\Sigma}''$ and $\dot{\Sigma}_\infty''$ now counted > 0 upwards, and we identify Y_∞ and U_∞ as the mass fraction Y_a and wind speed U recorded by the top instruments of the weather station. Using this equation and our net flux measurements provided in dimensionless form in Eqs. (53)-(32), we estimate the coefficient a_m and the exchange flux $\dot{\Sigma}_\infty''$ toward the ABL aloft (section 13).

Acknowledgments

We are grateful to Patrick Perré, Florian Pierre, and Joël Casalinho for help measuring sand isotherms; to Jean-Luc Métayer for measuring particle size distribution, to Anthony Hay, Ali Sultan, Renée Richer, Christopher Ogden, Dah Ould Ahmedou, Pascal Dupont, Anushree Acharya, Sara Abdul-Majid, Osama Al Achek, Carlos Mejia, Nathalie Vriend, and Matthew Arran for assistance in the field; to Chun-Chieh (Jimmy) Chang for creating special batteries; to Robert Foster and Hai Trinh for advice on capacitance instrumentation; to Stephen Keast for help with probe design; to Marc Massot, Greg Bewley, Abraham Stroock, Jean-Yves Parlange, Tammo Steenhuis, Shmuel Assouline, Dani Or, Michael Gentzler and Sylvain Dupont for illuminating discussions; to Isabelle Louge and J. Gregory Butler for vetting the plain language summary; and to Amy East, Thomas Pächtz, Giora Kidron and anonymous reviewers for their insight on revising the manuscript. This paper was made possible by the support of NPRP grants 09-546-2-206 and 6-059-2-023 from the Qatar National Research Fund, and by a Qatar Foundation Research Excellence Award.

The entire data set, movie animations, original figures and nomenclature are available as supporting information at doi:10.7298/kqgg-5888. The “ReadMeDataFilesContents” file lists their contents and specifies all parameters adopted in this work. The movies animating Figs. 4, 6 and 8 are listed in the “ReadMeSupportingMovie” file.

References

- Abdul-Majid, S., Chatziefthimiou, A. D., Richer, R., Dargham, S., Hay, A. G., Louge, M. Y., ... Courant, J. (2016). The fate of *Scincus mitranus* in the face of climate change: A Qatar case study. In *Qatar university life science symposium 2016: Biodiversity, sustainability and climate change, with perspectives from Qatar* (Vol. 2016, p. 44). doi: 10.5339/qproc.2016
- Abdul-Majid, S., Graw, M. F., Chatziefthimiou, A. D., Nguyen, H., Richer, R., Louge, M., ... Hay, A. G. (2016). Microbial characterization of Qatari barchan sand dunes. *PloS one*, 11, e0161836. doi: 10.1371/journal.pone.0161836

- 1429 Al-Shukaili, A., Al-Busaidi, H., Al-Maktoumi, A., Abdalla, O., Shelukhina, O., &
1430 Kacimov, A. R. (2019). Oblique porous composite as evaporating “cap”: Do
1431 desert dunes preserve moisture by capillary barriers and tilt of their slopes?
1432 *Water Resources Research*, *55*, 2504-2520. doi: 10.1029/2018WR024526
- 1433 Anderson, R. G., Zhang, X., & Skaggs, T. H. (2017). Measurement and partition-
1434 ing of evapotranspiration for application to vadose zone studies. *Vadose Zone*
1435 *Journal*, *16*, 1-9. doi: 10.2136/vzj2017.08.0155
- 1436 Anderson, T. B., & Jackson, R. (1967). Fluid mechanical description of fluidized
1437 beds. Equations of motion. *Industrial & Engineering Chemistry Fundamentals*,
1438 *6*, 527-539. doi: 10.1021/i160024a007
- 1439 Arran, M. I. (2018). *Avalanching on dunes and its effects: Size statistics, stratifi-*
1440 *cation, and seismic surveys* (Doctoral dissertation, University of Cambridge).
1441 <https://doi.org/10.17863/CAM.26140>. doi: 10.17863/CAM.26140
- 1442 Assouline, S., & Kamaï, T. (2019). Liquid and vapor water in vadose zone profiles
1443 above deep aquifers in hyper-arid environments. *Water Resources Research*,
1444 *55*, 3619–3631. doi: 10.1029/2018WR024435
- 1445 Babinsky, E., & Sojka, P. E. (2002). Modeling drop size distributions. *Progress*
1446 *in Energy and Combustion Science*, *28*, 303–329. doi: 10.1016/S0360-1285(02)
1447 00004-7
- 1448 Banta, R. M., Mahrt, L., Vickers, D., Sun, J., Balsley, B., Pichugina, Y., &
1449 Williams, E. (2007). The very stable boundary layer on nights with weak low-
1450 level jets. *J. Atmospheric Sciences*, *64*, 3068–3090. doi: 10.1175/JAS4002.1
- 1451 Baveye, P. C. (2013). Comment on “Averaging theory for description of envi-
1452 ronmental problems: What have we learned?” by William G. Gray, Cass T.
1453 Miller, and Bernhard A. Schrefler. *Advances in Water Resources*, *52*, 328-330.
1454 doi: 10.1016/j.advwatres.2012.08.012
- 1455 Bird, R. B., Stewart, W. E., & Lightfoot, E. N. (2007). *Transport phenomena, 2nd*
1456 *ed.* NY: John Wiley & Sons.
- 1457 Boast, C. W., & Robertson, T. M. (1982). A “micro-lysimeter” method for
1458 determining evaporation from bare soil: Description and laboratory eval-
1459 uation. *Soil Science Society of America Journal*, *46*, 689-696. doi:
1460 10.2136/sssaj1982.03615995004600040005x
- 1461 Borujerdi, P. R., Shotorban, B., Mahalingam, S., & Weise, D. R. (2019). Mod-
1462 eling of water evaporation from a shrinking moist biomass slab subject
1463 to heating: Arrhenius approach versus equilibrium approach. *Interna-*
1464 *tional Journal of Heat and Mass Transfer*, *145*, 118672. doi: 10.1016/
1465 j.ijheatmasstransfer.2019.118672
- 1466 Böttcher, C. J. F., & Bordewijk, P. (1978). *Theory of electric polarization, vol. II:*
1467 *Dielectrics in time-dependent fields.* NY: Elsevier.
- 1468 Bristow, C. S., Duller, G. A. T., & Lancaster, N. (2007). Age and dynamics of linear
1469 dunes in the namib desert. *Geology*, *35*, 555-558. doi: 10.1130/G23369A.1
- 1470 Brooks, R. H., & Corey, A. T. (1964). Hydraulic properties of porous media. In
1471 *Hydrology papers no. 3* (p. 1-27). Colorado State University, Fort Collins,
1472 CO. [https://www.wipp.energy.gov/library/CRA/2009_CRA/references/
1473 Others/Brooks_Corey_1964_Hydraulic_Properties_ERMS241117.pdf](https://www.wipp.energy.gov/library/CRA/2009_CRA/references/Others/Brooks_Corey_1964_Hydraulic_Properties_ERMS241117.pdf).
- 1474 Brutsaert, W. (1982). *Evaporation into the atmosphere: theory, history and applica-*
1475 *tions.* New York: Springer Science & Business Media. doi: 10.1007/978-94-017
1476 -1497-6
- 1477 Brutsaert, W. (1986). Catchment-scale evaporation and the atmospheric
1478 boundary layer. *Water Resources Research*, *22*, 39S-45S. doi: 10.1029/
1479 WR022i09Sp0039S
- 1480 Bürgi, P. M., & Lohman, R. (2021). High-resolution soil moisture evolution
1481 in hyper-arid regions: A comparison of InSAR, SAR, microwave, optical,
1482 and data assimilation systems in the southern Arabian Peninsula. *Jour-*
1483 *nal of Geophysical Research: Earth Surface*, *126*, e2021JF006158. doi:

- 1484 10.1029/2021JF006158
 1485 Cáceres, L., Gómez-Silva, B., Garró, X., Rodríguez, V., Monardes, V., & McKay,
 1486 C. P. (2007). Relative humidity patterns and fog water precipitation in the
 1487 Atacama desert and biological implications. *J. Geophys. Res.*, *112*, G04S14.
 1488 doi: 10.1029/2006JG000344
 1489 Cahill, A. T., & Parlange, M. B. (1998). On water vapor transport in field soils.
 1490 *Water Resources Research*, *34*, 731-739. doi: 10.1029/97WR03756
 1491 Cappa, C. D., Smith, J. D., Drisdell, W. S., Saykally, R. J., & Cohen, R. C. (2007).
 1492 Interpreting the h/d isotope fractionation of liquid water during evapo-
 1493 ration without condensation. *J. Phys. Chem. C*, *111*, 7011-7020. doi:
 1494 10.1021/jp065095r
 1495 Carslaw, H. S., & Jaeger, J. C. (1959). *Conduction of heat in solids, 2nd ed.* Oxford:
 1496 Clarendon Press.
 1497 Cereceda, P., Larrain, H., Osse, P., Faras, M., & Egana, I. (2008). The climate of
 1498 the coast and fog zone in the Tarapacá region, Atacama desert, Chile. *Atmo-*
 1499 *spheric Res.*, *87*, 301-311. doi: 10.1016/j.atmosres.2007.11.011
 1500 Chapman, S., & Cowling, T. (1953). *The mathematical theory of non-uniform gases.*
 1501 Cambridge, UK: Cambridge University Press.
 1502 Claudin, P., Louge, M. Y., & Andreotti, B. (2016). Basal pressure variations induced
 1503 by a turbulent flow over a wavy surface. *Front. Phys.*, *9*, 682564. doi: 10.3389/
 1504 fphy.2021.682564
 1505 Davarzani, H., Smits, K., Tolene, R. M., & Illangasekare, T. (2014). Study of the
 1506 effect of wind speed on evaporation from soil through integrated modeling of
 1507 the atmospheric boundary layer and shallow subsurface. *Water Resources*
 1508 *Research*, *50*, 661-680. doi: 10.1002/2013WR013952
 1509 Davidsson, B. J. R., & Hosseini, S. (2021). Implications of surface roughness in mod-
 1510 els of water desorption on the moon. *MNRAS*, *506*, 3421-3429. doi: 10.1093/
 1511 mnras/stab1360
 1512 de Félice, P. (1968). Etude des échanges de chaleur entre l'air et le sol sur deux sols
 1513 de nature différente. *Geophys. Bioklimatol. Ser. A*, *16*, 70-80. doi: 10.1007/
 1514 BF02248867
 1515 Dincer, T., Al-Mugrin, A., & Zimmermann, U. (1974). Study of the infiltration and
 1516 recharge through the sand dunes in arid zones with special reference to the
 1517 stable isotopes and thermonuclear tritium. *Journal of Hydrology*, *23*, 79-109.
 1518 doi: 10.1016/0022-1694(74)90025-0
 1519 Dupont, S., Bergametti, G., Marticorena, B., & Simoëns, S. (2013). Modeling salta-
 1520 tion intermittency. *J. Geophys. Res. Atmospheres*, *118*, 7109-7128. doi: 10
 1521 .1002/jgrd.50528
 1522 Elder, J. W. (1967). Steady free convection in a porous medium heated from below.
 1523 *Journal of Fluid Mechanics*, *27*, 29-48. doi: 10.1017/S0022112067000023
 1524 Fan, Y., Boukerkour, Y., Blanc, T., Umbanhowar, P. B., Ottino, J. M., & Lueptow,
 1525 R. M. (2012). Stratification, segregation, and mixing of granular materials in
 1526 quasi-two-dimensional bounded heaps. *Physical Review E*, *86*, 051305. doi:
 1527 10.1103/PhysRevE.86.051305
 1528 Fang, H. Y., Cai, Q. G., Chen, H., & Li, Q. Y. (2007). Mechanism of formation of
 1529 physical soil crust in desert soils treated with straw checkerboards. *Soil Tillage*
 1530 *Res.*, *93*, 222-230. doi: 10.1016/j.still.2006.04.006
 1531 Feigenwinter, C., Franceschi, J., Larsen, J. A., Spirig, R., & Vogt, R. (2020). On
 1532 the performance of microlysimeters to measure non-rainfall water input in a
 1533 hyper-arid environment with focus on fog contribution. *J. Arid Environ.*, *182*,
 1534 104260. doi: 10.1016/j.jaridenv.2020.104260
 1535 Fourrière, A. (2009). *River morphodynamics : Width selection, ripples and dunes*
 1536 (Doctoral dissertation, Université Paris-Diderot). [https://pastel.archives](https://pastel.archives-ouvertes.fr/pastel-00005562)
 1537 [-ouvertes.fr/pastel-00005562](https://pastel.archives-ouvertes.fr/pastel-00005562).
 1538 Fourrière, A., Claudin, P., & Andreotti, B. (2010). Bedforms in a turbulent stream:

- 1539 Formation of ripples by primary linear instability and of dunes by nonlin-
 1540 ear pattern coarsening. *Journal of Fluid Mechanics*, *649*, 287-328. doi:
 1541 10.1017/S0022112009993466
- 1542 Gambaryan-Roisman, T. (2014). Liquids on porous layers: Wetting, imbibition
 1543 and transport processes. *Current Opinion in Colloid and Interface Science*, *19*,
 1544 320–335. doi: 10.1016/j.cocis.2014.09.001
- 1545 Gao, B., Davarzani, H., Helmig, R., & Smits, K. M. (2018). Experimental and
 1546 numerical study of evaporation from wavy surfaces by coupling free flow
 1547 and porous media flow. *Water Resources Research*, *54*, 9096-9117. doi:
 1548 10.1029/2018WR023423
- 1549 Gottlieb, P., Wilkie, G., Sutherland, D., Ho-Tun, E., Suthers, S., Perera, K., ...
 1550 Rayner, J. (2000). Using quantitative electron microscopy for process mineral-
 1551 ogy applications. *JOM*, *52*, 24-25. doi: 10.1007/s11837-000-0126-9
- 1552 Gray, W. G., & Miller, C. T. (2005). Thermodynamically constrained averaging the-
 1553 ory approach for modeling flow and transport phenomena in porous medium
 1554 systems: 1. Motivation and overview. *Advances in Water Resources*, *28*,
 1555 161-180. doi: 10.1016/j.advwatres.2004.09.005
- 1556 Griffis, T. J. (2013). Tracing the flow of carbon dioxide and water vapor between
 1557 the biosphere and atmosphere: A review of optical isotope techniques and
 1558 their application. *Agricultural and Forest Meteorology*, *174*, 85-109. doi:
 1559 10.1016/j.agrformet.2013.02.0095
- 1560 Harari, Z. (1996). Ground-penetrating radar (GPR) for imaging stratigraphic fea-
 1561 tures and groundwater in sand dunes. *Journal of applied Geophysics*, *36*, 43-
 1562 52. doi: 10.1016/S0926-9851(96)00031-6
- 1563 Heulin, T., Luca, G. D., Barakat, M., de Groot, A., Blanchard, L., Ortet, P., &
 1564 Achouak, W. (2012). Bacterial adaptation to hot and dry deserts. In H. S-
 1565 L. et al. (Ed.), (p. 6985). Wien: Springer-Verlag.
- 1566 Honniball, C. I., Lucey, P. G., Li, S., Shenoy, S., Orlando, T. M., Hibbitts, C. A.,
 1567 ... Farrell, W. M. (2020). Molecular water detected on the sunlit moon by
 1568 SOFIA. *Nature Astronomy*, 1–7. doi: 10.1038/s41550-020-01222-x
- 1569 Hudson, T., Aharonson, O., Schorghofer, N., Farmer, C. B., Hecht, M. H., &
 1570 Bridges, N. T. (2007). Water vapor diffusion in mars subsurface environments.
 1571 *J. Geophys. Res.*, *112*, E05016. doi: 10.1029/2006JE002815
- 1572 Hunt, J. C. R., Leibovich, S., & Richards, K. (1988). Turbulent shear flows over low
 1573 hills. *Quarterly Journal of the Royal Meteorological Society*, *114*, 1435-1470.
 1574 doi: 10.1002/qj.49711448405
- 1575 Iwamatsu, M., & Horii, K. (1996). Capillary condensation and adhesion of two wet-
 1576 ter surfaces. *Journal of Colloid and Interface Science*, *182*, 400–406. doi: 10
 1577 .1006/jcis.1996.0480
- 1578 Jackson, J. D. (1999). *Classical electrodynamics* (3rd ed.). New York: Wiley.
- 1579 Jackson, P. S., & Hunt, J. C. R. (1975). Turbulent wind flow over a low hill. *Quar-
 1580 terly Journal of the Royal Meteorological Society*, *101*, 929-955. doi: 10.1002/qj
 1581 .49710143015
- 1582 Jafari, P., Masoudi, A., Irajizad, P., Nazari, M., Kashyap, V., Eslami, B., &
 1583 Ghasemi, H. (2018). Evaporation mass flux: a predictive model and exper-
 1584 iments. *Langmuir*, *34*, 11676-11684. doi: 10.1021/acs.langmuir.8b02289
- 1585 Johnson, R., & Dettre, R. (1964). Contact angle hysteresis. III. Study of an ide-
 1586 alized heterogeneous surface. *J. Phys. Chem.*, *68*, 1744–1750. doi: 10.1021/
 1587 j100789a012
- 1588 Jury, W. A., & Letey Jr, J. (1979). Water vapor movement in soil: Reconciliation of
 1589 theory and experiment. *Soil Science Society of America Journal*, *43*, 823-827.
 1590 doi: 10.2136/sssaj1979.03615995004300050001x
- 1591 Kamai, T., & Assouline, S. (2018). Evaporation from deep aquifers in arid regions:
 1592 Analytical model for combined liquid and vapor water fluxes. *Water Resources
 1593 Research*, *54*, 4805–4822. doi: 10.1029/2018WR023030

- 1594 Kanury, A. M. (1975). *Introduction to combustion phenomena*. Amsterdam, The
 1595 Netherlands: Gordon & Breach Publishers.
- 1596 Kays, W. M., & Crawford, M. E. (1980). *Convection heat and mass transfer, 2nd ed.*
 1597 NY: McGraw-Hill.
- 1598 Kidron, G. J., & Kronenfeld, R. (2020). Microlysimeters overestimate the amount of
 1599 non-rainfall water – an experimental approach. *Catena*, *194*, 104691. doi: 10
 1600 .1016/j.catena.2020.104691
- 1601 Kidron, G. J., & Starinsky, A. (2019). Measurements and ecological implications
 1602 of non-rainfall water in desert ecosystems – A review. *Ecohydrology*, *12*, e2121.
 1603 doi: 10.1002/eco.2121
- 1604 Kizito, F., Campbell, C., Campbell, G., Cobos, D., Teare, B., Carter, B., & Hop-
 1605 mans, J. (2008). Frequency, electrical conductivity and temperature analysis
 1606 of a low-cost capacitance soil moisture sensor. *Journal of Hydrology*, *352*(3),
 1607 367-378. doi: <https://doi.org/10.1016/j.jhydrol.2008.01.021>
- 1608 Klein, P. M., Hu, X.-M., Shapiro, A., & Xue, M. (2016). Linkages between
 1609 boundary-layer structure and the development of nocturnal low-level jets
 1610 in Central Oklahoma. *Boundary-Layer Meteorol.*, *158*, 383–408. doi:
 1611 10.1007/s10546-015-0097-6
- 1612 Kleinhans, M. G. (2004). Sorting in grain flows at the lee side of dunes. *Earth-*
 1613 *Science Reviews*, *65*, 75-102. doi: 10.1016/S0012-8252(03)00081-3
- 1614 Kobayashi, T., Matsuda, A., Kamichika, M., & Sato, T. (1986). Studies of the dry
 1615 surface layer in a sand dune field. (1) Modeling of the dry surface layer of sand
 1616 under isothermal steady conditions. *J. Agric. Meteorol.*, *42*, 113–118. doi:
 1617 10.2480/agrmet.42.113
- 1618 Kobayashi, T., Matsuda, A., Kamichika, M., & Yamamura, Y. (1991). Why the
 1619 thickness of the dry surface layer in sand dune fields exhibits a diurnal varia-
 1620 tion? *J. Agric. Meteorol.*, *47*, 3–9. doi: 10.2480/agrmet.47.3
- 1621 Kocurek, G. (1991). Interpretation of ancient eolian sand dunes. *Annual review*
 1622 *of Earth and planetary sciences*, *19*, 43-75. doi: 10.1146/annurev.ea.19.050191
 1623 .000355
- 1624 Koffman, L. D., Plesset, M. S., & Lees, L. (1984). Theory of evaporation and con-
 1625 densation. *Physics of Fluids*, *27*, 876-880. doi: 10.1063/1.864716
- 1626 Kroy, K., Sauermann, G., & Herrmann, H. J. (2002). Minimal model for sand dunes.
 1627 *Physical Review Letters*, *88*, 054301. doi: 10.1103/PhysRevLett.88.054301
- 1628 Lagarias, J. C., Reeds, J., Wright, M. H., & Wright, P. E. (1998). Convergence
 1629 properties of the Nelder–Mead simplex method in low dimensions. *SIAM Jour-*
 1630 *nal on optimization*, *9*, 112–147. doi: 10.1137/S1052623496303470
- 1631 Lancaster, J., Lancaster, N., & Seely, M. K. (1984). Climate of the central Namib
 1632 desert. *MADOQUA.*, *14*, 5–61. doi: 10520/AJA10115498_484
- 1633 Lehmann, P., Assouline, S., & Or, D. (2008). Characteristic lengths affecting evap-
 1634 orative drying of porous media. *Physical Review E*, *77*, 056309 1-16. doi: 10
 1635 .1103/PhysRevE.77.056309
- 1636 Lehmann, P., & Or, D. (2009). Evaporation and capillary coupling across vertical
 1637 textural contrasts in porous media. *Physical Review E*, *80*, 046318 1-13. doi:
 1638 10.1103/PhysRevE.80.046318
- 1639 Li, Y. Q., Davidovits, P., Kolb, C. E., & Worsnop, D. R. (2001). Mass and thermal
 1640 accommodation coefficients of H₂O (g) on liquid water as a function of
 1641 temperature. *The Journal of Physical Chemistry A*, *105*, 10627-10634. doi:
 1642 10.1021/jp012758q
- 1643 Li, Z., Vanderborght, J., & Smits, K. M. (2020). The effect of the top soil layer on
 1644 moisture and evaporation dynamics. *Vadose Zone J.*, *19*, e20049 1-15. doi: 10
 1645 .1002/vzj2.20049
- 1646 Louge, M. Y., Foster, R. L., Jensen, N., & Patterson, R. (1998). A portable capac-
 1647 itance snow sounding instrument. *Cold Regions Science and Technology*, *28*,
 1648 73–81. doi: 10.1016/S0165-232X(98)00015-9

- 1649 Louge, M. Y., Mandur, J., Blincoe, W., Tantuccio, A., & Meyer, R. F. (2021).
 1650 Non-invasive, continuous, quantitative detection of powder level and mass
 1651 holdup in a metal feed tube. *Powder Technology*, *382*, 1467-477. doi:
 1652 10.1016/j.powtec.2020.12.068
- 1653 Louge, M. Y., Steiner, R., Keast, S. C., Decker, R., Dent, J., & Schneebeli, M.
 1654 (1997). Application of capacitance instrumentation to the measurement of
 1655 density and velocity of flowing snow. *Cold Regions Science and Technology*,
 1656 *25*, 47–63. doi: 10.1016/S0165-232X(96)00016-X
- 1657 Louge, M. Y., Tuccio, M., Lander, E., & Connors, P. (1996). Capacitance mea-
 1658 surements of the volume fraction and velocity of dielectric solids near a
 1659 grounded wall. *Review of Scientific Instruments*, *67*, 1869–1877. doi:
 1660 10.1063/1.1146991
- 1661 Louge, M. Y., Valance, A., Babah, H. M., Moreau-Trouvé, J.-C., el Moctar, A. O.,
 1662 Dupont, P., & Ahmedou, D. O. (2010). Seepage-induced penetration of water
 1663 vapor and dust beneath ripples and dunes. *J. Geophys. Res.*, *115*, F02002. doi:
 1664 10.1029/2009JF001385
- 1665 Louge, M. Y., Valance, A., el Moctar, A. O., & Dupont, P. (2010). Packing vari-
 1666 ations on a ripple of nearly monodisperse dry sand. *J. Geophys. Res.*, *115*,
 1667 F02001. doi: 10.1029/2009JF001384
- 1668 Louge, M. Y., Valance, A., el Moctar, A. O., Xu, J., Hay, A. G., & Richer, R.
 1669 (2013). Temperature and humidity within a mobile barchan sand dune, im-
 1670 plications for microbial survival. *J. Geophys. Res. Earth Surf.*, *118*. doi:
 1671 10.1002/2013JF002839
- 1672 Mahrt, L. (2014). Stably stratified atmospheric boundary layers. *Annual Review of*
 1673 *Fluid Mechanics*, *46*, 23–45. doi: 10.1146/annurev-fluid-010313-141354
- 1674 Marek, R., & Straub, J. (2001). Analysis of the evaporation coefficient and the con-
 1675 densation coefficient of water. *International Journal of Heat and Mass Trans-*
 1676 *fer*, *44*, 39-53. doi: 10.1016/S0017-9310(00)00086-7
- 1677 Michel, S., Avouac, J., Ayoub, F., Ewing, R., Vriend, N., & Heggy, E. (2018). Com-
 1678 paring dune migration measured from remote sensing with sand flux prediction
 1679 based on weather data and model, a test case in Qatar. *Earth and Planetary*
 1680 *Science Letters*, *497*, 12-21. doi: 10.1016/j.epsl.2018.05.037
- 1681 Mitarai, N., & Nori, F. (2006). Wet granular materials. *Adv. in Physics*, *55*, 1–45.
 1682 doi: 10.1080/00018730600626065
- 1683 Monin, A. S. (1970). The atmospheric boundary layer. *Annual Review of Fluid Me-*
 1684 *chanics*, *2*, 225-250. doi: 10.1146/annurev.fl.02.010170.001301
- 1685 Mortarini, L., Stefanello, M., Degrazia, G., Roberti, D., Castelli, S. T., & Anfossi,
 1686 D. (2016). Characterization of wind meandering in low-wind-speed conditions.
 1687 *Boundary-Layer Meteorol.*, *161*, 165–182. doi: 10.1007/s10546-016-0165-6
- 1688 Musa, R. A., Takarrouht, S., Louge, M. Y., Xu, J., & Berberich, M. E. (2014). Pore
 1689 pressure in a wind-swept rippled bed below the suspension threshold. *J. Geo-*
 1690 *phys. Res. Earth Surf.*, *119*, 112–147. doi: 10.1002/2014JF003293
- 1691 Myeni, L., Moeletsi, M. E., & Clulow, A. D. (2019). Present status of soil moisture
 1692 estimation over the African continent. *Journal of Hydrology: Regional Studies*,
 1693 *21*, 14-24. doi: 10.1016/j.ejrh.2018.11.004
- 1694 Nasrallah, S. B., & Perré, P. (1988). Detailed study of a model of heat and mass
 1695 transfer during convective drying of porous media. *International Journal of*
 1696 *Heat and Mass Transfer*, *31*, 957-967. doi: 10.1016/0017-9310(88)90084-1
- 1697 Optis, M., Monahan, A., & Bosveld, F. C. (2014). Moving beyond Monin-Obukhov
 1698 similarity theory in modelling wind-speed profiles in the lower atmospheric
 1699 boundary layer under stable stratification. *Boundary-Layer Meteorol.*, *153*,
 1700 497–514. doi: 10.1007/s10546-014-9953-z
- 1701 Or, D., Lehmann, P., Shakraeni, E., & Shokri, N. (2013). Advances in soil evapora-
 1702 tion physics - a review. *Vadose Zone Journal*, *12*, 1-16. doi: 10.2136/vzj2012
 1703 -0163

- 1704 Parlange, J. Y. (1980). Water transport in soils. *Annual review of fluid mechanics*,
1705 12, 77-102. doi: 10.1146/annurev.fl.12.010180.000453
- 1706 Persad, A. H., & Ward, C. A. (2016). Expressions for the evaporation and condensa-
1707 tion coefficients in the Hertz-Knudsen relation. *Chemical Reviews*, 116, 7727-
1708 7767. doi: 10.1021/acs.chemrev.5b00511
- 1709 Philip, J. R. (1964). Kinetics of capillary condensation in wedge-shaped pores. *J.*
1710 *Chem. Phys.*, 41, 911-916. doi: 10.1063/1.1726032
- 1711 Philip, J. R., & De Vries, D. A. (1957). Moisture movement in porous materials
1712 under temperature gradients. *Eos, Transactions American Geophysical Union*,
1713 38, 222-232. doi: 10.1029/TR038i002p00222
- 1714 Prado, J. R., & Vyazovkin, S. (2011). Activation energies of water vaporization
1715 from the bulk and from laponite, montmorillonite, and chitosan powders.
1716 *Thermochimica Acta*, 524, 197-201. doi: 10.1016/j.tca.2011.06.005
- 1717 Prat, M. (2002). Recent advances in pore-scale models for drying of porous me-
1718 dia. *Chemical Engineering Journal*, 86, 153-164. doi: 10.1103/PhysRevE.80
1719 .046318
- 1720 Qian, R., Li, J., Liu, L., & Zhao, Z. (2014). Internal structure of sand dunes in
1721 the Badain Jaran desert revealed by GPR and its implications to inter-dune
1722 lake hydrology. In *Proceedings of the 15th international conference on ground*
1723 *penetrating radar* (p. 166-169). doi: 10.1109/ICGPR.2014.6970407
- 1724 Ravi, S., Zobeck, T. M., Over, T. M., Okin, G. S., & D'Odorico, P. (2006). On the
1725 effect of moisture bonding forces in air-dry soils on threshold friction velocity
1726 of wind erosion. *Sedimentology*, 53, 597-609. doi: 10.1002/2013JF002839
- 1727 Reesink, A. J., & Bridge, J. S. (2009). Influence of bedform superimposition and
1728 flow unsteadiness on the formation of cross strata in dunes and unit bars
1729 - Part 2, further experiments. *Sedimentary Geology*, 222, 274-300. doi:
1730 10.1016/j.sedgeo.2009.09.014
- 1731 Reynolds, W. C., Kays, W. M., & Kline, S. J. (1958). Heat transfer in the turbu-
1732 lent incompressible boundary layer. IV - Effect of location of transition and
1733 prediction of heat transfer in a known transition region. In NASA MEMO
1734 12-2-58W. Washington, D.C. [https://ntrs.nasa.gov/api/citations/
1735 20050158659/downloads/20050158659.pdf](https://ntrs.nasa.gov/api/citations/20050158659/downloads/20050158659.pdf).
- 1736 Richards, L. A. (1931). Capillary conduction of liquids through porous mediums.
1737 *Physics*, 1, 318-333. doi: 10.1063/1.1745010
- 1738 Ritsema, C. J., & Dekker, L. W. (1994). Soil moisture and dry bulk density patterns
1739 in bare dune sands. *Journal of Hydrology*, 154, 107-131. doi: 10.1016/0022
1740 -1694(94)90214-3
- 1741 Robinson, M., & Barrows, C. (2013). Namibian and North American sand-diving
1742 lizards. *J. Arid Environ.*, 93, 116-125. doi: 10.1016/j.jaridenv.2012.08.003
- 1743 Rotnicka, J. (2013). Aeolian vertical mass flux profiles above dry and moist sandy
1744 beach surfaces. *Geomorphology*, 187, 27-37. doi: 10.1016/j.geomorph.2012.12
1745 .032
- 1746 Rubel, G. O., & Gentry, J. W. (1984). Measurement of the kinetics of solu-
1747 tion droplets in the presence of adsorbed monolayers: Determination of
1748 water accommodation coefficients. *J. Phys. Chem.*, 88, 3142-3148. doi:
1749 10.1021/j150658a046
- 1750 Scanlon, T. M., & Kustas, W. P. (2010). Partitioning carbon dioxide and water va-
1751 por fluxes using correlation analysis. *Agricultural and Forest Meteorology*, 150,
1752 89-99. doi: 10.1016/j.agrformet.2009.09.005
- 1753 Shahraeeni, E., Lehmann, P., & Or, D. (2012). Coupling of evaporative fluxes from
1754 drying porous surfaces with air boundary layer: Characteristics of evapora-
1755 tion from discrete pores. *Water Resources Research*, 48, W09525 1-15. doi:
1756 10.1029/2012WR011857
- 1757 Shahraeeni, E., & Or, D. (2010). Pore-scale analysis of evaporation and condensa-
1758 tion dynamics in porous media. *Langmuir*, 26, 13924-13936. doi: 10.1021/

- 1759 la101596y
 1760 Shang, S., Horne, R. N., & Jr, H. J. R. (1995). Water vapor adsorption on geother-
 1761 mal reservoir rocks. *Geothermics*, *24*, 523-540. doi: 10.1016/0375-6505(95)
 1762 00008-E
 1763 Shao, Y., Fraedrich, K., & Ishizuka, M. (2021). Modelling soil moisture in hyper-arid
 1764 conditions. *Boundary-Layer Meteorology*, *179*, 169-186. doi: 10.1007/s10546
 1765 -020-00596-9
 1766 Shen, L., & Chen, Z. (2007). Critical review of the impact of tortuosity on diffusion.
 1767 *Chemical Engineering Science*, *62*, 3748-3755. doi: 10.1016/j.ces.2007.03.041
 1768 Shokri, N., Lehmann, P., Vontobel, P., & Or, D. (2008). Drying front and wa-
 1769 ter content dynamics during evaporation from sand delineated by neu-
 1770 tron radiography. *Water Resources Research*, *44*, W06418 1-11. doi:
 1771 10.1029/2007WR006385
 1772 Smith, J. D., Cappa, C. D., Drisdell, W. S., Cohen, R. C., & Saykally, R. J. (2006).
 1773 Raman thermometry measurements of free evaporation from liquid water
 1774 droplets. *Journal of the American Chemical Society*, *128*, 12892-12898. doi:
 1775 10.1021/ja063579v
 1776 Sprenger, M., Stumpp, C., Weiler, M., Aeschbach, W., Allen, S. T., Benettin, P., ...
 1777 Werner, C. (2019). The demographics of water: A review of water ages in the
 1778 critical zone. *Reviews of Geophysics*, *57*, 800834. doi: 10.1029/2018RG000633
 1779 Tsukahara, T., Mizutani, W., Mawatari, K., & Kitamori, T. (2009). NMR studies of
 1780 structure and dynamics of liquid molecules confined in extended nanospaces. *J.*
 1781 *Phys. Chem. B*, *113*, 10808-10816. doi: 10.1021/jp903275t
 1782 Vanderborght, J., Fetzer, T., Mosthaf, K., Smits, K. M., & Helmig, R. (2017). Heat
 1783 and water transport in soils and across the soil-atmosphere interface: 1. theory
 1784 and different model concepts. *Water Resources Research*, *53*, 1057-1079. doi:
 1785 10.1002/2016WR019982
 1786 Van Genuchten, M. T. (1980). A closed-form equation for predicting the hydraulic
 1787 conductivity of unsaturated soils. *Soil Science Soc. of America J.*, *44* (5), 892-
 1788 898.
 1789 Vincenti, W. G., & Kruger, C. H. (1965). *Introduction to physical gas dynamics*.
 1790 NY: John Wiley & Sons.
 1791 Wang, J., & Mitsuta, Y. (1992). Evaporation from the desert: Some preliminary
 1792 results of HEIFE. *Boundary-Layer Meteorology*, *59*, 413-418. doi: 10.1007/
 1793 BF02215461
 1794 Wang, T., Han, P., Wu, S., Bu, X., Guan, Y., & Yang, S. (2011). *Deserts and aeol-*
 1795 *ian desertification in China*. Beijing: Science Press.
 1796 Wilcox, C. S., Ferguson, J. W., Fernandez, G. C., & Nowak, R. S. (2004).
 1797 Fine root growth dynamics of four Mojave desert shrubs as related to soil
 1798 moisture and microsite. *J. Arid Environ.*, *56*, 129-148. doi: 10.1016/
 1799 S0140-1963(02)00324-5
 1800 Wyngaard, J. C. (2010). *Turbulence in the atmosphere*. NY: Cambridge University
 1801 Press.
 1802 Xu, J., & Louge, M. Y. (2015). Statistical mechanics of unsaturated porous media.
 1803 *Physical Review E*, *92*, 062405 1-17. doi: 10.1103/PhysRevE.92.062405
 1804 Yeşilbaş, M., & Boily, J.-F. (2016). Particle size controls on water adsorption and
 1805 condensation regimes at mineral surfaces. *Scientific Reports*, *6*, 1-10. doi: 10
 1806 .1038/srep32136
 1807 Zhang, J., & Datta, A. K. (2004). Some considerations in modeling of moisture
 1808 transport in heating of hygroscopic materials. *Drying Technology*, *22*, 1983-
 1809 2008. doi: 10.1081/LDRT-200032740
 1810 Zribi, M., Kotti, F., Amri, R., Wagner, W., Shabou, M., Lili-Chabaane, Z., &
 1811 Baghdadi, N. (2014). Soil moisture mapping in a semiarid region, based
 1812 on ASAR/Wide Swath satellite data. *Water Resources Research*, *50*, 823-835.
 1813 doi: 10.1002/2012WR013405